ANALYSIS OF THE REACTOR CAVITY COOLING SYSTEM FOR VERY HIGH TEMPERATURE GAS-COOLED REACTORS USING COMPUTATIONAL FLUID DYNAMICS TOOLS

A Thesis

by

ANGELO FRISANI

Submitted to the Office of Graduate Studies of
Texas A&M University
in partial fulfillment of the requirements for the degree of

MASTER OF SCIENCE

May 2010

Major Subject: Nuclear Engineering

ANALYSIS OF THE REACTOR CAVITY COOLING SYSTEM FOR VERY HIGH TEMPERATURE GAS-COOLED REACTORS USING COMPUTATIONAL FLUID DYNAMICS TOOLS

A Thesis

by

ANGELO FRISANI

Submitted to the Office of Graduate Studies of
Texas A&M University
in partial fulfillment of the requirements for the degree of

MASTER OF SCIENCE

Approved by:

Chair of Committee,	Yassin A. Hassan
Committee Members,	Hamn-Ching Chen
	Pavel V. Tsvetkov
	Victor M. Ugaz
Head of Department,	Raymond J. Juzaitis

May 2010

Major Subject: Nuclear Engineering

ABSTRACT

Analysis of the Reactor Cavity Cooling System

for Very High Temperature Gas-Cooled Reactors

Using Computational Fluid Dynamics Tools. (May 2010)

Angelo Frisani, B.S., University of Pisa

Chair of Advisory Committee: Dr. Yassin A. Hassan

The design of passive heat removal systems is one of the main concerns for the modular Very High Temperature Gas-Cooled Reactors (VHTR) vessel cavity. The Reactor Cavity Cooling System (RCCS) is an important heat removal system in case of accidents. The design and validation of the RCCS is necessary to demonstrate that VHTRs can survive to the postulated accidents. The commercial Computational Fluid Dynamics (CFD) STAR-CCM+/ V3.06.006 code was used for three-dimensional system modeling and analysis of the RCCS.

Two models were developed to analyze heat exchange in the RCCS. Both models incorporate a 180º section resembling the VHTR RCCS bench table test facility performed at Texas A&M University. All the key features of the experimental facility were taken into account during the numerical simulations.

Two cooling fluids (i.e., water and air) were considered to test the capability of maintaining the RCCS concrete walls temperature below design limits.

Mesh convergence was achieved with an intensive parametric study of the two different cooling configurations and selected boundary conditions.

To test the effect of turbulence modeling on the RCCS heat exchange, predictions using several different turbulence models and near-wall treatments were evaluated and compared. The models considered included the first-moment closure one equation Spalart-Allmaras model, the first-moment closure two-equation k-ε and k-ω models and the second-moment closure Reynolds Stress Transport (RST) model. For the near wall treatments, the *low* y^+ and the *all* y^+ wall treatments were considered. The two-layer model was also used to investigate the effect of near-wall treatment.

The comparison of the experimental data with the simulations showed a satisfactory agreement for the temperature distribution inside the RCCS cavity medium and at the standpipes walls. The tested turbulence models demonstrated that the Realizable k-ε model with two-layer *all* y^+ wall treatment performs better than the other k-ε models for such a complicated geometry and flow conditions. Results are in satisfactory agreement with the RST simulations and experimental data available.

A scaling analysis was developed to address the distortion introduced by the experimental facility and CFD model in simulating the physics inside the RCCS system with respect to the real plant configuration. The scaling analysis demonstrated that both the experimental facility and CFD model give a satisfactory reproduction of the main flow characteristics inside the RCCS cavity region, with convection and radiation heat exchange phenomena being properly scaled from the real plant to the model analyzed.

NOMENCLATURE

AKN	Abe-Kondoh-Nagano
ANL	Argonne National Laboratory;
A_α	annulus cross flow area;
A_c	reactor cavity equivalent area of heat transfer by convection;
A_o	total standpipes cross flow area;
A_{rad}	reactor cavity equivalent area of heat transfer by radiation;
BOP	Balance of Plant;
CFD	Computational Fluid Dynamics;
c_p	specific heat;
D	hydraulic diameter;
D_1	downcomer diameter (i.e., D_{Ip});
D_2	inner diameter of the annulus;
D_3	outer diameter of the annulus;
D_4	external diameter of the outer tube (i.e., D_{ext});
DCC	Depressurized Conduction Cooldown scenario;
D_{ext}	external diameter of the outer tube;
DES	Detached Eddy Simulation;
D_{Ip}	diameter of the inner tube;
DLOFC	Depressurized Loss-of-Flow-Circulation accident;
DOE	U.S. Department of Energy;

F	friction factor;
g	gravity;
GT-MHR	Gas Turbine-Modular Helium Reactor;
GIF	Generation IV International Forum;
H	cavity height;
HTR-10	Chinese High Temperature Gas-Cooled Reactor;
HTTR	High-Temperature Engineering Test Reactor;
h_{cav}	heat transfer coefficient for heat transfer in the reactor cavity by convection;
h_e	heat transfer coefficient at the annulus external wall;
h_I	heat transfer coefficient at the inner tube wall;
h_{IO}	heat transfer coefficient at the annulus inner wall;
HTGR	High Temperature Gas Reactor;
HTR-10	Chinese High Temperature Gas-Cooled Reactor;
HTTR	High-Temperature Engineering Test Reactor;
IAEA	International Atomic Energy Agency;
IHX	Intermediate Heat Exchanger;
INET	Institute of Nuclear Energy Technology;
JAEA	Japan Atomic Energy Agency (formerly JAERI);
k	thermal conductivity;
LES	Large Eddy Simulation;
L_h	length of the standpipes heated section;

LWR	Light Water Reactor;
NGNP	Next Generation Nuclear Plant;
NRC	Nuclear Regulatory Commission;
PBMR	Pebble Bed Modular Reactor;
PBR	Pebble Bed Reactor
PCC	Pressurized Conduction Cooldown scenario;
PCU	Power Conversion Unit;
P_e	perimeter of the annulus external surface;
P_I	perimeter of the annulus inner surface;
p_{in}	pressure at the inlet of standpipes;
PIRT	Phenomena Identification and Ranking Table;
PLOFC	Pressurized Loss-Of-Flow-Circulation accident;
p_{out}	pressure at the outlet of standpipes;
Δp	p_{in} - p_{out};
ΔP	$\Delta p / \rho_o U_r^2$;
Q	heat transferred from the reactor vessel to the RCCS cavity;
RCCS	Reactor Cavity Cooling System;
R&D	Research and Development;
RPV	Reactor Pressure Vessel;
RST	Reynolds Stress Transport;
SNU	Seoul National University;
T	temperature;

T_α	temperature of water in the annulus;
T_c	temperature of the standpipes external surface;
T_e	temperature of water in the annulus;
T_h	average reactor vessel external surface temperature;
T_I	temperature of water in the inner tube;
T_o	reference temperature at the standpipes inlet;
T_r	reference temperature at the standpipes outlet;
TRISO	Tri-isotopic, ceramic-coated-particle fuel;
T_{se}	temperature of the annulus external wall;
T_{sI}	temperature of the inner tube;
U	velocity;
U_0	reference water velocity at the standpipes inlet;
u^*	reference velocity in the air-cavity region;
V	velocity component in the horizontal direction;
VHTR	Very High Temperature Gas-Cooled Reactors;
W	velocity component in the vertical direction;
Y	horizontal direction;
Z	axial direction;

Greek symbols

β	=	volumetric coefficient of thermal expansion;

ε = emissivity;

μ = dynamic viscosity;

θ = non-dimensional temperature;

Π = similarity group;

ρ = density;

ρ_o = reference water density;

σ = Stefan-Boltzmann constant;

Subscripts

c = cold;

d = down;

e = external;

h = hot;

I = inner;

h = hot;

m = model;

p = plant;

R = experimental to plant ratio;

r = reference value;

s = structure;

u = up;

Similarity groups

$$Gr = \left(\frac{g\rho^2 \beta \left(T_h - T_c\right) H^3}{\mu^2} \right), \quad \text{Grashof number;}$$

$$\frac{Gr}{\mathrm{Re}^2} = \frac{g\beta \left(T_h - T_c\right) H}{u^{*2}}, \quad \text{Grashof/Re}^2 \text{ number;}$$

$$N_c = \frac{A_c h_{cav}}{A_\alpha U_0 \rho_0 c_p}, \quad \text{Cavity convective number;}$$

$$N_r = \frac{A_{rad} \varepsilon \sigma T_0^4}{A_\alpha U_0 \rho_0 c_p \left(T_r - T_0\right)}, \quad \text{Cavity radiation number;}$$

$$N_t = \left(\frac{T_r}{T_0} - 1 \right), \quad \text{Temperature ratio number;}$$

$$\mathrm{P}e = \mathrm{Re} \cdot \mathrm{Pr} = \frac{\rho c_p u^* H}{k}, \quad \text{Peclet number;}$$

$$\mathrm{Pr} = \frac{\mu c_p}{k}, \quad \text{Prandlt number;}$$

$$\mathrm{Re} = \left(\frac{\rho u^* H}{\mu} \right), \quad \text{Reynolds number;}$$

$$Ra = \frac{c_p g \rho^2 \beta \left(T_h - T_c\right) H^3}{\mu k} \quad \text{Rayleigh number;}$$

$$Ri = \frac{g\beta \left(T_r - T_0\right) L_r}{U_0^2}, \quad \text{Richardson number;}$$

$St_I = \frac{4h_I L_r}{\rho c_p U_0 D_{Ip}}$, Stanton number (inner tube);

$St_e = \frac{P_e h_e L_r}{\rho c_p U_0 A_\alpha}$, Stanton number (annulus external wall);

$St_\alpha = \frac{P_I h_{IO} L_r}{\rho c_p U_0 A_\alpha}$, Stanton number (annulus inner wall);

TABLE OF CONTENTS

Page

Page

LIST OF FIGURES

Page

Page

Page

Page

Page

Page

LIST OF TABLES

Page

Page

1. INTRODUCTION

The Very High Temperature Gas-Cooled Reactor (VHTR) concept was promulgated in the Generation IV technology roadmap (Generation IV International Forum, 2002) as one of the Next Generation Nuclear Power Plant (NGNP) design. The most likely VHTR candidates are the prismatic and pebble-bed designs. Various design and analysis tools are needed to calculate the behavior of the NGNP within its normal, off normal and accident conditions. Thus software tools and adequate experiments for their validation or "benchmarking" must be provided.

The gas-cooled thermal reactors built in the past are characterized by operations at conditions with substantial design and safety margins. The margins were designed to be large because of the analysis tools used. Those tools were not capable of calculating important local limiting parameters with sufficient accuracy to reduce the safety margins to more desirable levels such that the economics of the plant operational, off normal, and accident conditions could be optimized. This approach has resulted in sustained operational efficiencies that are below the Generation IV system goals.

Presently the State-of-the-art software and advanced detailed methods are not ready to perform design and analysis to the standard required by the VHTR. Considerable validation, and development of the necessary software tools, is required.

Although a specific NGNP design has not been selected, the most likely design will be either a prismatic or pebble-bed gas-cooled thermal reactor with known general characteristics. Therefore, the various steady-state and transient characteristics are

---

This thesis follows the style of Nuclear Engineering and Design.

known in general. A different suite of methods software is required to calculate the reactor physics behavior for prismatic as opposed to the pebble-bed gas-cooled reactor. However, the software used to calculate the thermal-hydraulics behavior is the same for both reactor types.

On-line nuclear power plants can only operate within limits defined by the capability of the licensee to demonstrate that all important *figures-of-merit* for plant safety parameters are never challenged (i.e., a sufficient margin must be observed so the figure-of-merits are not in danger of being violated). A figure-of-merit is a key parameter indicative of whether or not a safety limit or an equivalent failure limit has been breached. By the way of example, important figures-of-merit are fuel temperature and Reactor Pressure Vessel (RPV) wall temperature.

Each figure-of-merit has the potential to limit the operational envelope of the plant in some fashion such that restrictions (e.g., special precautions, operational procedures, or equivalent limitations) will be required to ensure the figure-of-merit is not challenged. In some cases the restrictions translate in operating the plant at power levels that are less than the designed power level. For other cases the restrictions may translate in reducing the rate-of-change of an operational parameter in going from one condition to another and thus to increase the operational transit time. In any case, such restrictions have an economy penalty as shown in the Nuclear Regulatory Commission website (2009).

The figures-of-merit used for the present light water reactors (LWR) were traditionally calculated using conservative assumptions and approaches that were guaranteed to yield calculated results with very large safety margins. Models of this sort

were based on prescription of sometimes arbitrary restrictions to ensure a large safety factor was present in the licensing calculations. The major drawback of the conservative methodology is that the calculated uncertainty, while known to be large, and conservative, is not quantified.

Best-estimate approaches were developed after many LWRs were licensed applying conservative methodologies. These best-estimate approaches have been used to perform some plant license re-evaluations. The best-estimate approaches have the advantage of enabling the calculational uncertainties to be defined and quantified. However, one-dimensional fluid flow models were almost exclusively used to calculate average or bulk values of the figures-of-merit in the various regions of the plant. Thus, to account for potential deviations from the one-dimensional model results, because of three-dimensional behavior, safety factors have been used to provide a sufficient margin from the limiting value.

For LWR analysis one-dimensional techniques were usually adequate for calculating the plant thermal-hydraulic behavior since the fluid temperatures, even under arduous conditions, were considerably less than the temperatures that challenge the structural materials limits, for example the reactor pressure vessel. This is not the case for the VHTR. Bulk outlet temperature for the VHTR must be in excess of 900 °C and as close to 1000 °C as possible is what is meant by having the VHTR meet generation IV plant operating requirements.

The main goal of the NGNP Methods is to develop and benchmark state-of-the-art analysis tools that will enable analysts to accurately calculate the core power

distribution, the core bypass, the peak outlet temperatures such that localized hot spots can be identified and either eliminated by design or quantified to a degree that licensing calculations can demonstrate the VHTR plant operation without challenging the safety margins, plant parameters, or figures-of-merit. Advanced tools for analyzing the VHTR are consistent with the new safety concerns inherent to the new design and the new system design requirements.

Reduced design uncertainty and risk due to the known uncertainty on the local conditions, reduced design iterations and design costs, an accelerated licensing process due to the adoption of known quantities with quantified uncertainties instead of prescribed arbitrary safety factors, capability of quantifying the safety and operational margins to optimal values for maximum outlet temperatures and maximum operational efficiencies are some of the advantages that advanced analysis tools offer respect to older computational tools.

The identification of the most challenging scenarios together with the dominant phenomena for a generic PBR design and a generic prismatic design represents a fundamental step in the development of the advanced computational tools. The ranking of the phenomena allows the prioritization of model development for the design and safety tools and the planning of experimental facilities and experimental matrices.

Among all the possible design basis accidents identified for the VHTR, the loss of heat transport system and shutdown cooling system and the Loss of Coolant Accident (LOCA) event in conjunction with water ingress from failed shutdown cooling system [hereafter referred as Pressurized Conduction Cooldown (PCC) scenario, and

Depressurized Conduction Cooldown (DCC) scenario, respectively] are considered the most demanding and most likely to lead to maximum vessel wall and fuel temperatures.

The Phenomena Identification and Ranking Table (PIRT) process carefully identifies the most demanding scenarios, and the associated most demanding phenomena. Key phenomena are those showing a predominant influence on the path taken during the most demanding scenarios. The key phenomena for the PCC and DCC scenarios are those that exert the greatest influence on the peak core temperatures and peak vessel wall temperatures. A detailed PIRT is not available because of the lack of a specific VHTR design. In Table 1 is shown a "first-cut" PIRT, developed for the prismatic and pebble-bed reactors, based on the knowledge gained from present Gas-Cooled Reactors and engineering judgment [see Schultz (2007)].

The thermal-fluid behavior of VHTR can be analyzed with computational fluid dynamics (CFD) codes, system codes, and severe accident codes. Of these software types, CFD can be used to analyze the fluid dynamics in any portion of NGNP. The strength of CFD codes is their capability to analyze the presence of localized hot spots and thermal gradients. The largest impediment of using CFD codes is their computational requirements and the size of the problem that requires analysis. System analysis software can also be used to analyze the fluid dynamics in any portion of the NGNP. However, only one-dimensional analysis can be performed using system codes if high-fidelity is required.

Table 1 – PIRT for normal operation, PCC and DCC scenarios

Scenario	Upper Plenum	Core	RCCS	Lower Plenum
DCC	i. Mixing and stratification ii. Hot plumes iii. Thermal resistance of structures	i. Thermal radiation and conduction of heat across the core ii. Axial heat conduction and radiation iii. Natural circulation in the Reactor pressure vessel iv. Power distribution v. Core configuration vi. Decay heat vii. Flow distribution viii. Material properties ix. Pressure drop	i. Laminar-turbulent transition flow ii. Forced-natural mixed convection flow iii. Heat transfer/radiation and convection in duct	i. Thermal mixing and stratifi-cation ii. Flow distribution
PCC	i. Mixing and stratification ii. Hot plumes iii. Thermal resistance of structures	i. Thermal radiation and conduction of heat across the core ii. Axial heat conduction and radiation iii. Natural circulation in reactor pressure vessel iv. Power distribution v. Core configuration vi. Decay heat vii. Flow distribution viii. Material properties ix. Pressure drop	i. Laminar-turbulent transition flow ii. Forced-natural mixed convection flow iii. Heat transfer/radiation and convection in duct	i. Thermal mixing and stratifi-cation ii. Flow distribution

To describe the VHTR performance and safety analysis, one-dimensional (1-D) system type codes, like RELAP5 or MELCOR, and multi-dimensional CFD codes can be used. The choice of 1-D over multi-dimensional codes first involves identifying the main phenomena, and from this the dimensionless numbers which characterize the phenomena and their values. In principle CFD codes can be equipped to model all phenomena for which the 1-D codes are suited. On the other hand, CFD codes require more detailed problem definition input and orders of magnitude more computational

time. Since both types of codes are based on conservation laws and empirical models (i.e., correlations of dimensionless numbers), the validation process can be performed using the same approach. The codes differ primarily in the level of detail present in the models to describe the underlying process and, hence, the types of experiment datasets needed to calibrate the models. In general, for 1-D codes validation is achieved using integral experiments (i.e., more than one fundamental phenomenon is taken into account). For CFD codes a separate effects experiment focuses on a single phenomenon. Advanced CFD codes will be needed to simulate regions of complex turbulent flow in the plant. Thermal-hydraulics system analysis codes can be applied in conjunction with CFD codes to analyze the full plant (i.e., integral approach). The distinction between CFD codes and system analysis codes stem from the distinctions between the software tools themselves. CFD codes use first-principle based solutions and subdivide a problem domain into cells that are small with respect to the phenomena that requires modeling. System analysis codes use field equations that have been simplified (e.g., by not including the viscous stress terms) and subdivide the problem into a macroscopic structure that does not model phenomena such as turbulent eddies.

The objective of the present research was to develop a qualification framework for CFD codes in the nuclear system safety analysis. The CFD code identified was the CD-ADAPCO commercial code STAR-CCM+/V3.06.006. The outcome of the present work was to identify the weakness in the code models for representing thermal-hydraulic phenomena expected to occur in the VHTR both during normal operation and accident conditions. Once the models that need to be developed are identified, the experiments

that must be performed to support the model development will be identified. Then the scaled experiments for the models validation must be identified.

The R&D plan is based on the assumption that an ever-improving PIRT will be available. The software used to analyze the VHTR behavior must be validated for the scenarios of importance identified by the PIRT. Experiments must be defined and built, and data must be produced to provide the basis for software validation. Development must be done to improve the software till the validation studies show the software can adequately calculate the key phenomena in the important plant scenarios. Once the software has been validated and shown to be capable of calculating the important phenomena to the accuracy required, the best-estimate analysis may begin.

Both the experimental research areas and the software-directed research areas are outlined in Table 2. Key regions of concern are identified. In each case, the issues are whether the system will survive, particularly under the most challenging accident conditions, and whether the system will have an adequate operational lifetime for the conditions that are postulated (rated operational conditions, off-normal operational conditions, and accident conditions). The high-priority research areas include: (a) the core heat transfer; (b) mixing in the upper plenum, as well as the lower plenum, hot duct, and turbine inlet; (c) the heat transfer in the RCCS; (d) air ingress following a system depressurization; (e) the behavior of the integral system during the key scenarios, including the contributions of the balance-of-plant. In the present work the attention was focused on the heat exchange occurring in the RCCS cavity region. CFD tools were used to simulate the evolution of the transient in the RCCS following a PCC accident.

Table 2 – Thermal-fluids methods R&D areas

R&D	Related R&D	Study Area	Need
1. Core Heat Transfer	Mixed convection experiment heated experiments, core heat transfer modeling, bypass experiments, system performance enhancements, Sana experiments.	Experimen-tal (E), CFD, and system analysis codes (S)	The core heat transfer, both with cooling flow (operational conditions) and without cooling flow (DCC and PCC), are instrumental in setting the maximum temperature levels for fuel and material R&D (core graphite, structural materials, and heat load to RCCS). The core heat transfer will determine the material selection and configuration in the VHTR core, vessel, and RCCS designs.
2. Upper and Lower plenums (UP and LP)	HTTR UP and LP, HTR_10 UP and LP, MIR, heated experiments, scaled vessel, jets and cross-flow data, upper plenum experiments, system performance enhancements.	E and CFD	Circulation in the upper plenum is important during the PCC scenario since hot plumes rising from the hot core may impinge on the upper head structures and lead to a potential overheating of localized regions in the upper vessel. The degree of lower plenum mixing determines both the temperature variations and the maximum temperatures that are experienced by the turbine blades, the lower plenum, hot duct, and power generation vessel structural components. The lower plenum mixing will determine the material selection and configuration in the NGNP lower plenum, hot duct, power generation vessel and turbine designs.
3. RCCS	ANL (air-cooled), Seoul National University (water-cooled), HTTR RCCS, fission product transport, system performance enhancements.	E, CFD, and S	The heat transfer efficiency of the RCCS will determine the overall design concept (whether air-cooled is sufficient or water-cooled is required in accordance with either a confinement or containment RCCS design), plus material selection of outer vessel wall, coatings (e.g., selection of materials with emissivities that change with surface temperature), natural circulation characteristics, etc.
4. Air Ingress	Diffusion model development, NACOK experiment.	E, CFD, and S	A gas-cooled very high temperature reactor should be able to survive the most challenging accident scenarios with minimal damage and thus should be able to resume operation in a minimum time frame. The system must be shown to sustain minimal damage following potential air ingress into the core region.
5. Integral System Behavior	HTTR, HTR_10, AVR, fission product transport, CFD and systems analysis code coupled calculations, behavior of balance –of-plant components (intermediate heat exchanger, turbine, compressor, reheater), analyses of pre-conceptual design, preliminary design, and final design.	E, CFD, and S	The ultimate system characterization, to show the final design is capable of meeting all operational expectations and of surviving the most challenging accident conditions, is performed using validated software tools. The tools consist of the neutronics and thermal-hydraulics software (coupled CFD and system analysis software) used in concert. This step is the culmination of the comprehensive R&D effort outlined herein.

2. SYSTEM DESCRIPTION AND PHENOMENA IDENTIFICATION AND RANKING TABLES

The reference gar-cooled VHTR designs are an extension of the earlier designs of the General Atomics' Gas Turbine-Modular Helium Reactor (GT-MHR) and the PBMR. The GT-MHR is a 600 MWth direct cycle gas reactor with a prismatic core as shown in Fig. 1. The reactor operating pressure is 70 bars and the outlet temperature is 850 °C. The reference PBMR is a 400 MWth direct cycle gas reactor with a pebble-bed core as shown in Fig. 2. The reactor operating pressure is 90 bars and the outlet temperature is 900 °C. The target gas-cooled VHTR differs from these designs, mainly in that the target reactor outlet temperature may be higher, although a specific value has not been defined, and the VHTR is to produce hydrogen in addition to electricity.

Both designs are assumed to have confinements. That is, the reactor cavity is vented to the atmosphere if the cavity is over-pressurized. However, the vent (pressure relief valve) is fitted with a filter to minimize the release of harmful material to the environment and the pressure relief valve will close once the confinement pressure is reduced to an acceptable value. As the figures show, the two reactor system designs mainly differ in the core configuration, which is the prismatic or pebble-bed form of the reactor fuel. This has implications in the layout of the vessel and its internals particularly from the functional viewpoint of fueling and defueling. The basic concept of the system layout is the same for both designs (i.e., both are direct cycle) as far as the components of the balance of plant (BOP) is concerned.

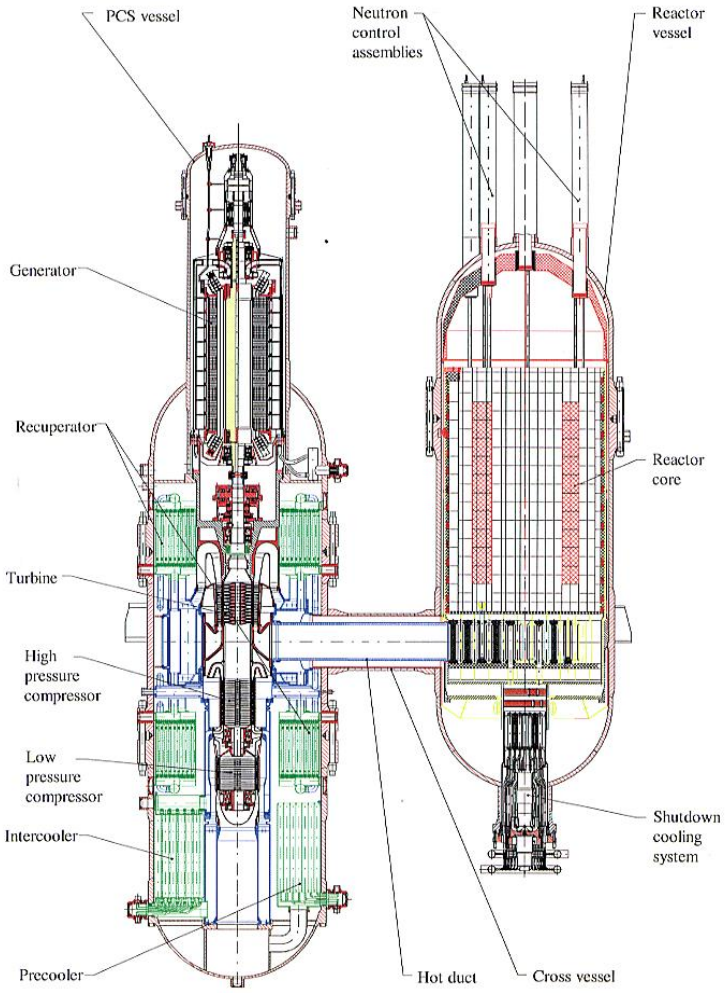

a) System Design Configuration and Helium Flow Path

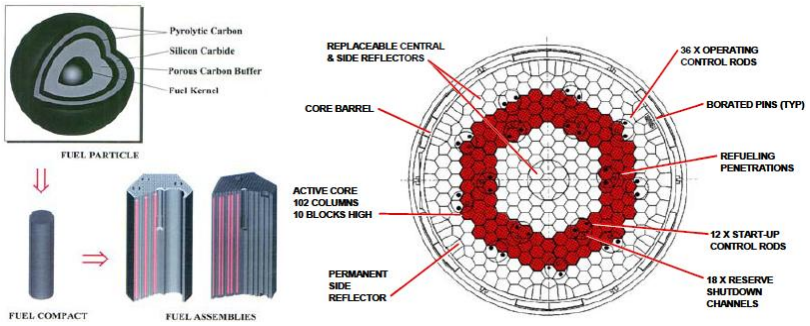

b) Prismatic Core Layout

Fig. 1 – HT-MHR design

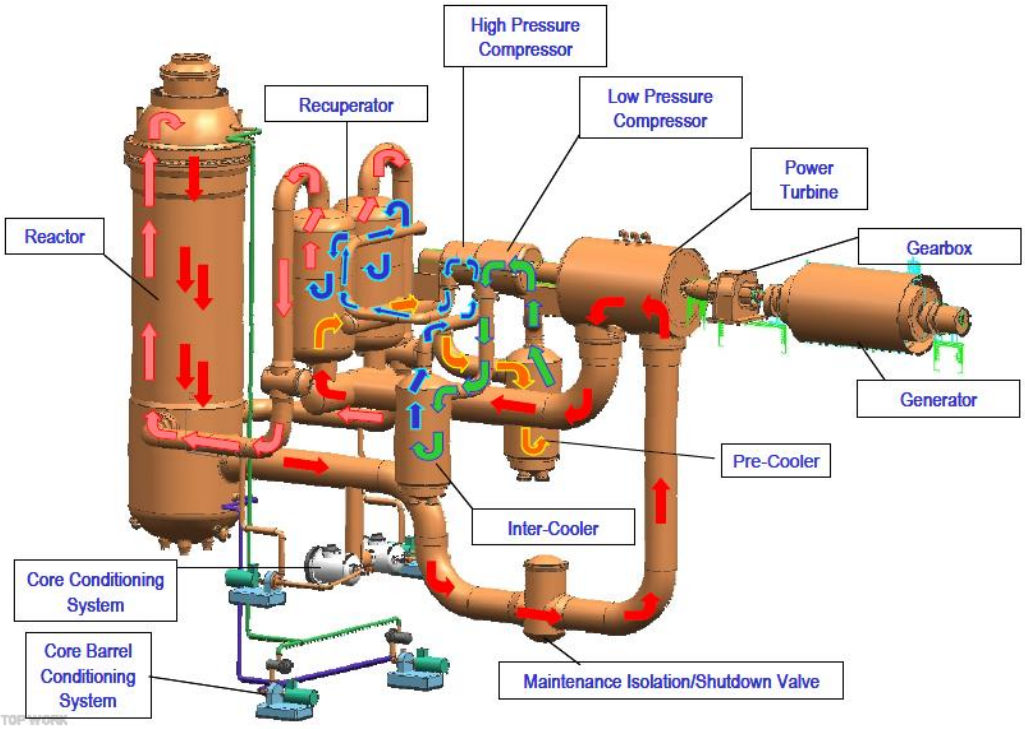

a) System design configuration and helium flow path

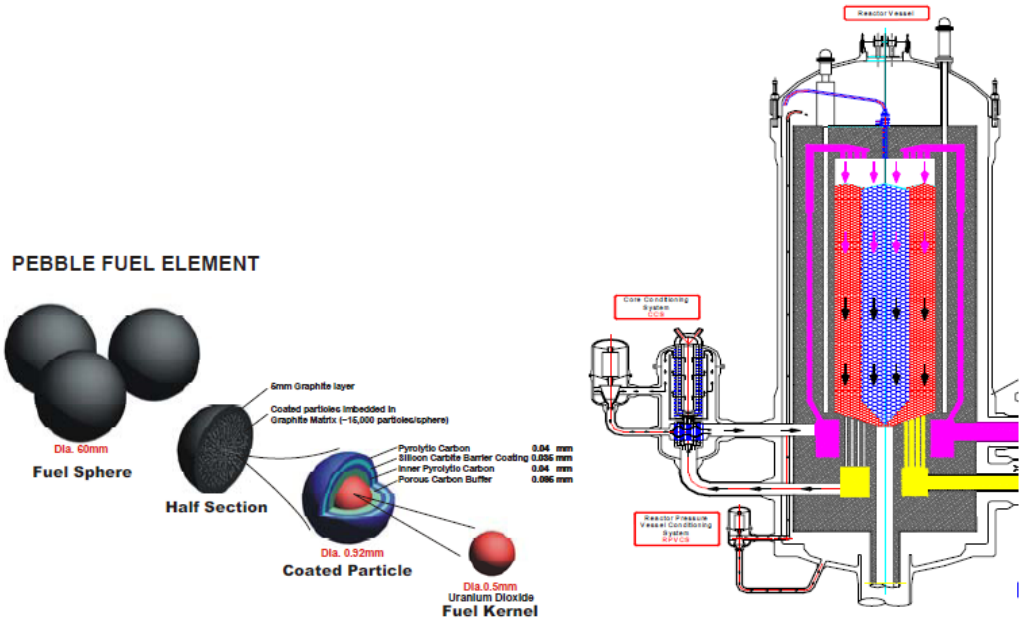

b) Pebble Core and Reactor Vessel Configuration

Fig. 2 – PBMR design

The variation of the Brayton cycle utilized is similar for both plants. However, the GT-MHR design adopts an integral power conversion unit (PCU) in a vessel and a concentric hot/cold duct that connects the reactor system vessel and the PCU system vessel. This leads to a very compact design layout with minimal ducting. On the other hand, the PBMR design adopts distributed PCU components and separated hot and cold ducts. This leads to a larger footprint for the BOP with major lengths of ducting. Thermal stratification in the ducting may be quite different. This is an example of event phenomena differences which the diversity in the design may lead to and which will be detailed in the PIRTs [see Schultz (2007)].

The prismatic core consists of an inner reflector region surrounded by an annulus of fuel blocks which is in turn surrounded by an annulus of outer reflector elements. The fuel blocks are composed of hexagonal columns of graphite with circular holes that run the full length of the column. The fueled holes contain fuel compact that contains Tri-isotopic (TRISO) particles, while the coolant holes align axially to form coolant channels.

The 400 MWth pebble bed core consists of approximately 450,000 fuel pebbles that are stacked in a graphite reflector structure. The pebbles are continuously refueled during plant operation. Central reflector pebbles have been replaced by central graphite reflector columns in the recent design. In Table 3 are shown the characteristic parameters and conditions for the GT-MHR and PBMR reactors, respectively.

Table 3 – Core parameters and full operating working conditions

Parameter	GT-MHR	PBMR
Reactor Power, Q (MWth)	600	400
T_{in}/T_{out} (°C)	491/850	500/900
Reactor Pressure (bars)	70	90
Power Density (W/cm^3)	~5	~6.6
Reactor Mass Flow Rate, W (kg/s)	320	147
Effective Core Height (m)	7.93	~11
Core Diameter (m)	2.96 ID/4.83 OD	2 ID/3.7 OD
Number of Fuel Blocks/Pebbles	1020	~450,000
Design Bypass Flow Fraction (%)	10 ~ 15	Not applicable

2.1 Characteristics Common to Both Configurations

The working fluid for both reactors is helium. The helium enters the vessel through either a circular cross-section or a pipe annulus near the bottom of the vessel in a direction that is at right angles to the axis of the reactor vessel. Then, the helium makes a 90-degree turn upwards and is distributed, via an upper plenum, into riser channels that lead upwards to an upper plenum that is over the core itself. At this point the helium is directed downwards from the upper plenum into the core. The helium moves from the core into a lower plenum and is directed to a circular cross-section pipe (the hot duct) that is mounted at right angle to the reactor vessel centerline. As the helium transit the core the gas temperature increases (by 400 °C to 500 °C). From the hot duct the helium enters the power conversion vessel and then is directed to the turbine inlet.

The helium coolant flow distribution in the core is governed by differential pressure between the upper and lower plena, the friction in the respective flow paths, and the local power generation. The moderator for both reactor configurations is graphite. Moreover, the fuel in both designs consists of TRISO fuel-particles dispersed in a

matrix. However, the matrix for the prismatic design is formed into a fuel pin compact while the matrix for the pebble bed design is formed into a sphere. Both designs rely on forced flow, provided by blowers, of the helium coolant during operation. Both designs rely on passive cooling during any loss-of-power scenarios or loss-of-coolant scenarios. The ultimate heat sink is the environment and all excess heat can be transported to the environment without natural circulation cooling inside the vessel via heat conduction and radiation to the vessel walls. From the vessel walls the heat is transported to the environment via a combination of radiation and natural circulation transport using some form of RCCS. Air is present in the confinement such that if the reactor depressurizes due to a leak in a pipe, air will ultimately enter the vessel by diffusion.

2.2 Fundamental Differences Between the Two Configurations

Core Thermal-Fluids: in the prismatic core, the helium coolant, within the prismatic blocks, follows well defined one-dimensional flow paths described by the coolant channels. However, an undefined quantity of bypass flow, ranging from ~10% to ~25% of the total coolant moves between the blocks.

In contrast, for a pebble bed reactor, the helium coolant moving through the pebble beds, follows multi-dimensional flow paths defined by the pebble-void fraction, which varies as function of core radius, and the individual contact points described by the pebble-bed column. During accidents, radiation and contact heat transfer between pebbles plays an important role in transmitting core afterheat to the reactor vessel walls. The core axial power distribution in the pebble core is more likely to be top-skewed than in the prismatic core due to the on-line refueling of fresh pebbles from the top.

Reactor Vessel Thermal-Fluids: even though the underlying design characteristics of both candidates are similar, the detailed designs of the reactor vessel internals are different in the two cases as shown in Fig. 3 and Fig. 4. In the prismatic design, helium flowing from the power conversion unit is mixed and redistributed in the lower plenum and flows upwards through six square riser ducts between the core barrel and the vessel wall. It is collected in the hemispheric upper plenum and then flows downwards into the core. In order to prevent overheating at the vessel, a thermal insulator is provided at the inner side of the vessel head. The helium jets discharged from the core are collected and mixed in the lower plenum. The helium then flows out of the vessel to the PCU.

In the pebble-bed reactor design, helium flow from the PCU is distributed in a doughnut-like inlet plenum and flows upwards through the riser which consists of 36 circular channels inside the outer reflector. The helium passes through the slots at the top of the riser and collects in the cylindrical upper plenum inside the upper graphite structure. It then flows downwards to the core. Helium from the core is collected and mixed in the lower plenum and then flows out of the vessel to the PCU.

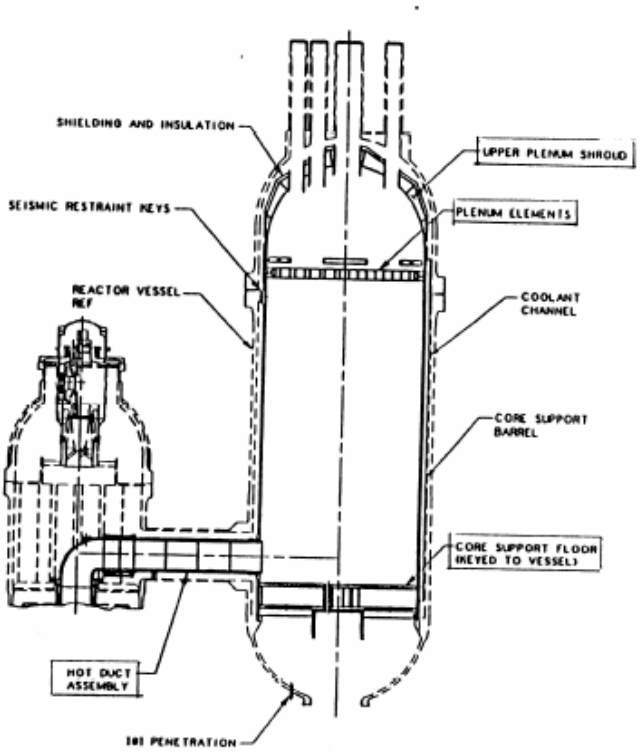

a) Vessel Metallic Structures

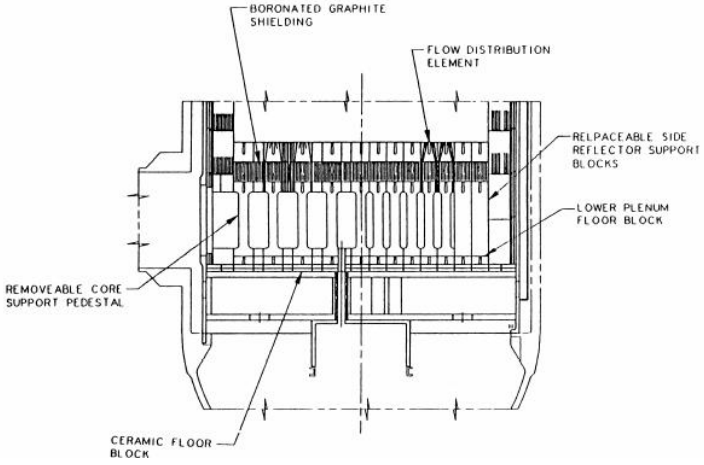

b) Vessel Lower Plenum

Fig. 3 – Prismatic reactor vessel internals

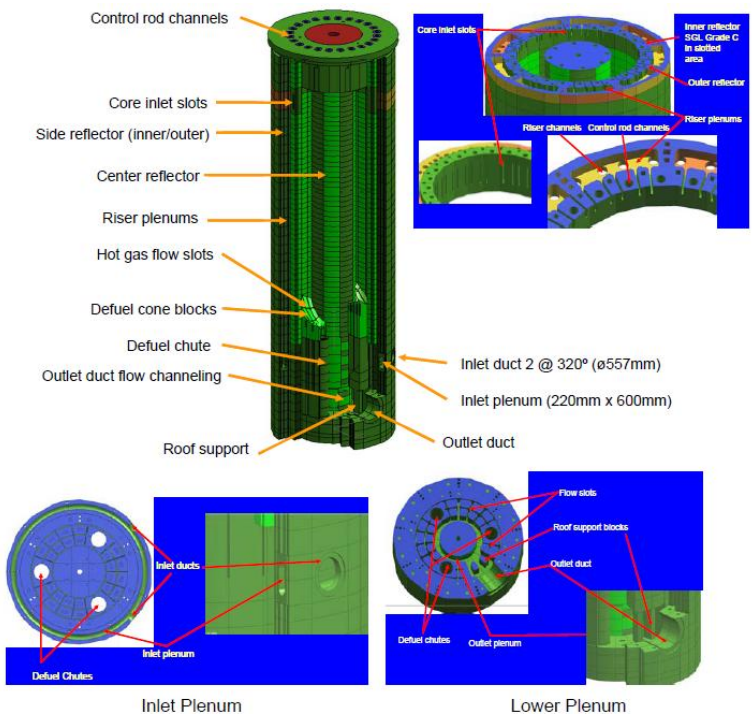

Fig. 4 – Pebble bed reactor vessel internals

The pebble-bed core slowly moves downwards, while the prismatic core is stationary. The cycle time through the core for an individual pebble is approximately 60 to 80 days. The transit distance is ~9.5 m.

The reactor kinetics and burnup characteristics are functions of the fuel and moderator geometry, the fuel enrichment, and the refueling characteristics of the respective designs. Because the pebble-bed core is continuously being replenished as spent pebbles are removed from the system (each pebble is cycled through the core approximately 9 times), the pebble-bed core generally has wider spectrum of depletion during operation than the prismatic reactor.

2.3 Reactor Cavity Cooling System (RCCS)

There is a major difference in the RCCS design between the two reference reactor configurations. The GT-MHR design has an air – cooled RCCS, while the PBMR design has a water-cooled RCCS. However, since the details of how the PBMR RCCS functions and its particular design features are still under development, an air-cooled RCCS was assumed to be present in both reference designs.

For the assumed air-cooled RCCS design, heat is radiated from the exterior of the reactor vessel wall to a series of heat exchangers that are oriented vertically and arranged in a circle around the exterior of the reactor vessel. Air flowing within these heat exchangers (ducts or standpipes) transports the heat to the exterior of the containment. The air is ducted in from outside the containment to these heat exchangers and then outside the confinement. The heat exchangers are rectangular ducts with a large aspect ratio and arranged so that one of the short sides faces the reactor vessel. These requirements dictate that the flow exiting the heat exchangers and the ducts that connect to them provide a barrier that separates the coolant flowing through the heat exchangers from the atmosphere inside the reactor/silo confinement. The air-cooled RCCS system is designed to be totally passive under all operating conditions and has no blowers to power the air flow through the heat exchangers. There are 292 risers, each a 5 by 25.4 cm rectangular duct. There is a 5 cm gap between adjacent risers and the short side of each riser faces the reactor vessel or the downcomer. The full power thermal-fluid conditions are given in Table 4. In Fig. 5 is shown a schematic of the air-cooled RCCS configuration.

Table 4 – RCCS duct dimensions and operating conditions

Parameter	**Air-cooled RCCS**
RCCS Power (MWth)	3.3
RCCS Air Flowrate (kg/s)	14.3
Number of Ducts	292
Average Duct Air Flowrate (kg/s)	0.049
Duct Dimensions (m)	0.05 x 0.25
Hydraulic Diameter (m)	0.083
Length of Active Core Region (m)	7.93

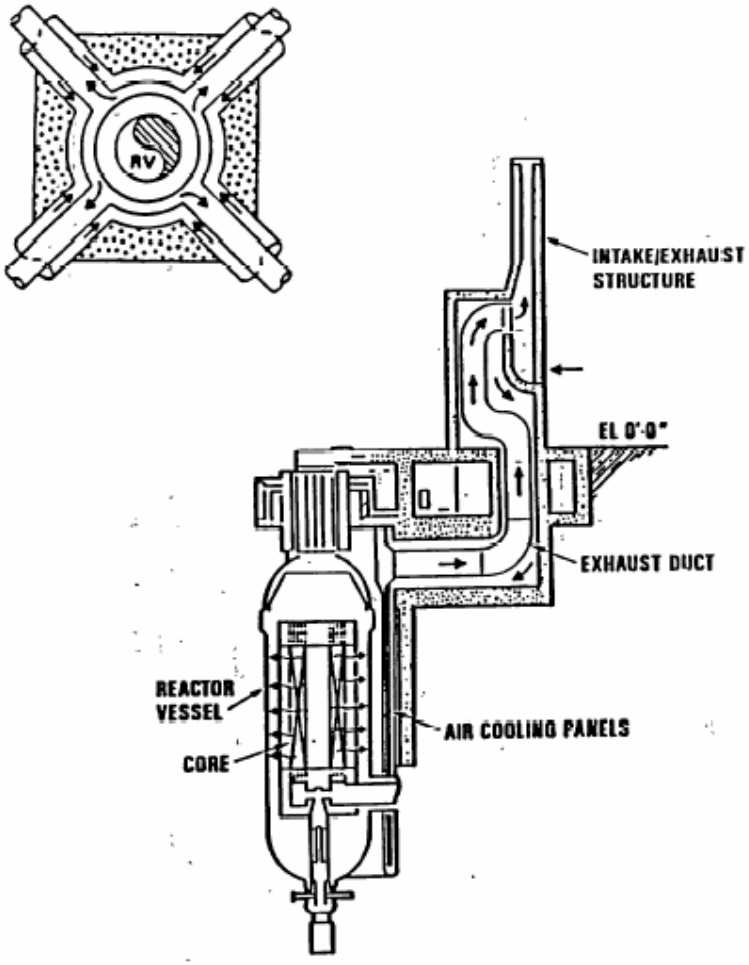

Fig. 5 – Schematics of air-cooled RCCS

2.4 Selection of the Reference Accident Scenarios

The complete spectrum of scenarios of importance is not yet defined for the VHTR, since it is strictly linked to the presently undefined VHTR design. However, it is expected that the following reference scenarios must be analyzed:

1. Anticipated operational occurrences:
    a) Main loop transient with forced core cooling;
    b) Loss of main and shutdown cooling loops;
    c) Accidental withdrawal of group of control rods followed by reactor shutdown;
    d) Small break LOCA (~1 in^2 area break).
2. Design basis accidents (assuming that only "safety-related" systems can be used for recovery):
    a) Loss of heat transport system and shutdown cooling system (similar to scenario 1b);
    b) Loss of heat transport system without control rod trip;
    c) Accidental withdrawal of a group of control rods followed by reactor shutdown;
    d) Unintentional control rod withdrawal together with failure of heat transport systems and shutdown cooling system;
    e) Earthquake-initiated trip withdrawal together with failure of heat transport systems and shutdown cooling system;

f) LOCA event in conjunction with water ingress from failed shutdown cooling system;
g) Large break LOCA;
h) Small break LOCA.

On the basis of the experience gained on gas-cooled reactor designers and experimentalists [see Ball (2003), Krüger et al. (1991)], scenario 2a and 2g (PCC and DCC, respectively) are considered the most demanding and most likely to lead to maximum vessel wall and fuel temperatures. Hence the PCC and the DCC events were selected as reference accident scenarios. The primary safety criteria are defined to be the fuel and vessel temperatures for both the PCC and DCC scenarios.

Since each part of the system might show a different response to each reference event, the phenomena of importance which are specific to each system region must be specified. The reactor vessel is composed of an inlet plenum, the risers, the upper plenum, reflectors, bypass, the core and fuel, and the lower plenum. The inlet plenum is located just downstream of the vessel inlet helium gas duct and is the volume that feeds the helium risers. Helium flows through the risers into the upper plenum, and from the upper plenum downwards through the core cooling channels and then to the lower plenum. From the lower plenum, the working fluid moves into the hot duct and from there into the power conversion system (i.e., a direct cycle system is considered). For the PCC and the DCC events specific scenario are defined and divided into time phases reflecting the major thermal-fluid processes and operational characteristics.

2.4.1 Pressurized Conduction Cooling (PCC) Event

The PCC scenario begins from a 100% power condition and is initiated by a loss-of-forced flow and simultaneous failure of shutdown cooling system to start. The forced flow is assumed to ramp to zero in conjunction with the blower coastdown characteristics. The reactor trips immediately. However, the coastdown of the primary flow results in rapid increase of the fuel temperature, while the vessel temperature decreases by the loss of forced flow. Because the forced flow coasts down to zero, the power conversion unit also is taken off line.

Once the system coastdown is completed, the system is left in a state where the controlling boundary conditions that govern the peak system temperatures are the system power level, the heat transfer from the fuel to the core, to the vessel, and then to the environment via the RCCS. The core heat-up slows down by the natural circulation cooling developed inside the core and the increase of heat removal by conduction and radiation cooling to the RCCS.

Eventually, the core cools down when the heat removal by conduction and radiation becomes larger than the core decay heat, and the system approaches a safe shutdown state. The temperatures of concern are the fuel temperature and that of the vessel structural components. Consequently there are two phases envisioned: (1) the coastdown, and (2) the heat-up and passive cooling phases. In Table 5 are summarized the accident phases of the PCC scenario.

Table 5 – PCC scenario and accident phases

Phases	Phase ID	Event Scenario and Major Processes
1	Coastdown	Event initiated by loss of offsite power and failure of shutdown cooling system to start. Reactor trips. Coastdown of primary flow results in "rapid" increase of fuel temperature, while reactor vessel temperature decreases with the loss of forced flow.
2	Heat-up and Passive Cooling	Core heat-up slows down by the natural circulation cooling inside the core and the increase of heat removal by conduction and radiation cooling to RCCS. Core cools down when the heat removal by conduction and radiation cooling to the RCCS becomes larger than core decay heat.

2.4.2 Depressurized Conduction Cooling (DCC) Event

The DCC scenario begins from a 100% power condition and is initiated by a double-ended guillotine break of both the cold and hot ducts. After the break, the reactor system blows down quickly. Reactor trips immediately to decrease the core power down to decay heat level. Nevertheless, core heats up rapidly by the decrease in heat removal by the loss of forced convection and the depressurization. Due to the loss of coolant, the power conversion unit is disconnected and does not significantly affect the progression of the transient. Helium discharge into the reactor cavity stops when the pressures of the reactor system and cavity equalize. Helium discharge from the reactor system purges part of the air in the cavity into the compartments in the confinement. Thus, the gas species in the cavity is redistributed. During blowdown, graphite dust accumulated in the reactor system is also transported into the confinement and eventually released to the environment through confinement relief valve. Filtered venting can reduce the release of dust to the environment.

Once the blowdown is complete, the system is left in a state where the controlling boundary conditions that govern the peak system temperatures are the system power level, the heat transfer from the fuel to the core, to the vessel, and then to the environment via the RCCS. The fuel temperature continues to increase and experiences the first peak when the core decay heat is balanced by the conduction and radiation cooling to the RCCS. During this phase, air remaining in the reactor cavity continuously enters into the reactor vessel by molecular diffusion. Because the diffusion process is very slow, the graphite chemical reaction rate with oxygen is very slow. Core heat-up slows down by the increase of heat removal to the RCCS. There exists a very weak natural circulation inside the core even at low pressure, but, it is not sufficient to redistribute the core temperature profile. With the increase of RCCS heat removal, the fuel temperature turns down after the first peak. Due to continuous air inflow, the density of the gas mixture in the core gradually increases. The temperatures of concern are the fuel temperature and that of the vessel structural components.

Once the bulk of the air diffuses into the reactor vessel, onset of bulk natural circulation is initiated by the density differences in the air mixture. Then, the extensive graphite oxidation occurs and generates a large amount of heat, which results in a second peak in the core temperature. Graphite oxidation stops when the air in the reactor vessel is depleted, and then, the fuel temperature starts to decrease. The core decay heat is continually removed by the bulk natural circulation cooling and by the conduction and radiation cooling to the RCCS.

Eventually, the core cools down when the heat removal by conduction and radiation cooling becomes larger than the core decay heat and the core reaches a safe shutdown state. The temperatures of concern are the fuel temperature and that of the vessel structural components. Three phases can be individuated for the DCC event: (1) the blowdown; (2) the molecular diffusion, and (3) the air mixture natural convection phase. In Table 6 is summarized the DCC scenario and the event phases addressed above.

Table 6 – DCC scenario and accident phases

Phases	**Phase ID**	**Event Scenario and Major Processes**
1	Blowdown	Event initiated by a double ended break of both cold and hot ducts. System depressurizes and reactor trips immediately. He discharge into the reactor cavity stops when the pressures of primary system and cavity equalize. He discharge from the primary system purges part of the air in the cavity, thus, gas species in cavity are redistributed. “Rapid” heat-up of core occurs by the loss of forced convection. Graphite dust from core is transported to the cavity then to the confinement. The confinement relief valves lift and effluent is released to the environment.
2	Molecular Diffusion	Air remaining in the reactor cavity enters into the reactor vessel by molecular diffusion. Thus, graphite chemical reaction rate is very slow. Very weak natural circulation occurs inside the core. First peak of fuel temperature occurs; then core temperature start to decrease when the heat removal by conduction and radiation cooling to the RCCS overrides core decay heat.
3	Natural convection	Large amount of air ingresses into the reactor vessel at onset of natural circulation due to density difference of gas mixture. Second peak of fuel temperature occurs with graphite oxidation. Graphite oxidation stops when air is depleted. Then, fuel temperature starts to decrease. Core cools down when the heat removal by conduction and radiation cooling to the RCCS becomes larger than core decay heat and the heat produced by oxidation. Core reaches a safe shutdown state.

2.4.3 Identification of Major Phenomena Components

The important phenomena that are expected to occur in the RCCS component during the progress of events are identified in this section together with their rankings. The following tables (Table 7 and Table 8) summarize the phenomena of major concern for the RCCS safety system identified for each time phase of the PCC and DCC event scenarios. Each phenomenon was ranked in two levels, either high (H), or medium (M).

Table 7 – RCCS phenomena ranking

Phenomena	**PCC**		**DCC**		
	1	**2**	**1**	**2**	**3**
Flow distribution		**H**		**H**	**H**
Heat transfer (mixed and free convection)		**H**		**H**	**H**
Pressure drop (mixed and free convection)		**M**		**M**	**M**
Radiation heat transfer		**H**		**H**	**H**
Gas conduction		**M**		**M**	**M**
Conduction to ground		**M**		**M**	**M**
Dust from core			**H**		
Air purge and gas species distribution			**H**	**H**	**H**

Table 8 – RCCS tube (air duct) phenomena ranking

Phenomena	**PCC**		**DCC**		
	1	**2**	**1**	**2**	**3**
Heat transfer (forced convection)		**H**		**H**	**H**
Heat transfer (mixed and free convection)		**H**		**H**	**H**
Pressure drop (forced convection)		**H**		**H**	**H**
Pressure drop (mixed and free convection)		**H**		**H**	**H**
Radiation heat transfer		**H**		**H**	**H**
Gas conduction		**M**		**M**	**M**
Fluid properties (humidity)		**M**		**M**	**M**

Heat removal by the RCCS during PCC event is the main path for cooling the vessel. The radial temperature gradient developed across the core heats the vessel wall.

The transfer of heat from the vessel wall to the air ducts is mainly by radiation heat transfer. Simulations with CFD codes indicate that this is more than 80 percent of the total heat transfer, with convection by air in the cavity making up the balance. The view factors for the reactor vessel communicating with the ducts are especially complex because both the vessel and standpipes geometry is cylindrical. In the cooldown phase, the hot plumes in the vessel head raise the temperature of the vessel wall at the top such that the vessel temperature might be the limiting condition.

The energy conducted through the duct walls (i.e., standpipes) from the reactor cavity is convected to the air inside the duct and is also radiated by the inner surfaces of the duct to adjacent surfaces. A buoyant head is established inside the ducts as the air heated by the duct walls expands, rises, and draws air in the duct inlet. The heat transfer and pressure loss phenomena inside the ducts depend on the velocity profile at the wall. If local buoyancy at the wall is introduced, then the heat transfer and pressure loss processes operate in the mixed rather than forced convection mode.

Considering the DCC event, the air in the reactor cavity before the onset of the upset will contain water vapor. Some of this water vapor will be present in the mixture of gases that enter the break site during the air ingress phase. In addition, the PBMR may include a source of cooling water that might enter the reactor cavity and, during the air ingress and natural convection phase, graphite dust may be discharged into the reactor cavity. If the cavity acts as a confinement, then the release of this radioactive dust into the environment through a relief valve must be considered. The dust may settle on the RCCS heat transfer surfaces in the cavity changing their heat transfer characteristics.

During the air ingress and natural convection phases, some of the air in the cavity that was not vented to the environment will move into the reactor vessel and oxidize graphite surfaces. For the air in the ducts apply the same considerations as for the PCC. In Table 9 are summarized the major phenomena identified for the PCC and the DCC accidents.

Table 9 – Summary of identified phenomena for RCCS

Phenomena	**Issue**
Fluid properties	Accurate prediction of gas properties is a basic requirement for analyzing gas flow and heat transfer
Convective Heat transfer	Accurate representation of heat transfer is to ensure adequate heat removal rate Heat transfer regime tends to be in mixed or free convection heat transfer during accident conditions
Pressure drop	Accurate representation of pressure drop is to ensure adequate design flow rate and flow distribution
Radiation heat transfer	Accurate representation of radiation heat transfer in a complex geometry is to ensure adequate heat removal from the core to the RCCS
Contact heat transfer	Accurate representation of contact heat transfer in a complex geometry is to ensure adequate heat removal from the core to the RCCS
Gas conduction heat transfer	Accurate representation of gas conduction is to ensure adequate heat removal from the core to the RCCS
Air purge and gas species distribution	Accurate prediction of gas species distribution in reactor cavity is to define oxygen supply to reactor vessel
Dust from the core	Graphite dust from the core is source term for fission product and aerosol transport in confinement
Conduction to ground	Conduction to ground is a final success path for core afterheat removal
Flow mixing in piping plenums	Flow mixing in RCCS plenums affects the flow distribution in RCCS
Buoyancy flow in chimney	Accurate prediction of buoyancy flow in chimney is to ensure RCCS heat removal rate

3. REACTOR CAVITY COOLING SYSTEM EXPERIMENTS

The RCCS research is essential since the heat transfer from the reactor pressure vessel to the RCCS is a key ingredient in defining the peak core and vessel wall temperatures during postulated accident scenarios. Two RCCS experimental efforts are presently underway. The first, at Argonne National Laboratory (ANL), aims to characterize the heat removal capabilities of both an air-cooled RCCS and a water-cooled RCCS designs. The second, at the Seoul National University, aims to characterize the heat removal capabilities of a water-cooled RCCS.

3.1 Argonne National Laboratory (ANL) RCCS Design

The objective of the experimental facility built at ANL is to acquire the model/code validation data for natural convection and radiation heat transfer in the reactor cavity and the RCCS by performing experiments in the ANL Natural Convection Shutdown Heat Removal Test Facility (NSTF). The NSTF will be used as an experiment "simulator". In Fig. 6 is shown a schematic of the ANL NSTF Test Facility. A scaling analysis will be performed on the facility. The scaling study will identify the important non-dimensional parameters for each separate-effects study for both air-cooled and water-cooled systems. Based on the results of the scaling/feasibility study, the range of experimental conditions will be determined as well as the appropriate experiment scale and appropriate fluids to be used that most effectively simulate full-scale system behavior. Based on the results of these scaling/feasibility studies and the analyses carried out on the RCCS, a test matrix will be developed. The ANL RCCS experimental results will capture key phenomena

expected to be present in the RCCS and provide data of sufficient resolution for development and assessment of applicable CFD and system codes.

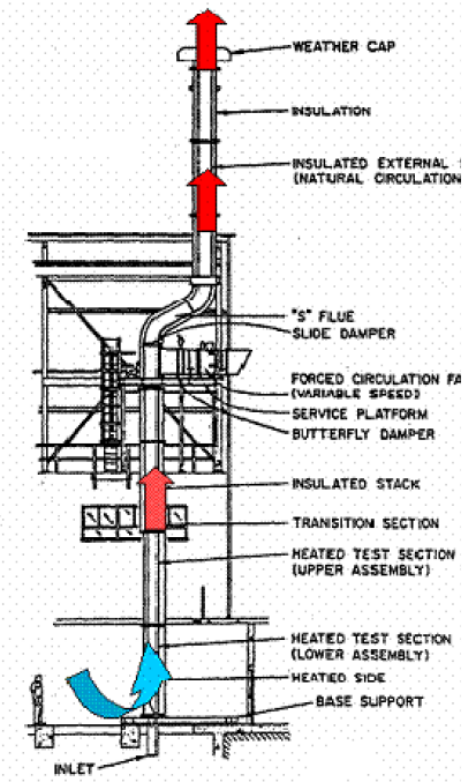

Fig. 6 – Schematics of natural convection shutdown heat removal test facility

3.2 Seoul National University (SNU) Water-Cooled RCCS

A water-cooled RCCS design may be preferred since its heat removal capability is larger per unit heat transfer area than a comparable air-cooled design. Hence a water-cooled design would be more desirable if a high-pressure containment is required for the VHTR instead of a low-pressure confinement system.

The SNU RCCS facility consists of three parts: the reactor vessel, an air cavity, and a water pool. In Fig. 7 is shown the SNU water-cooled RCCS experiment. The SNU

experiments are being performed using various gas mixtures in the gap and with various water pool elevations. The temperatures on the various surfaces are measured together with the surface emissivities and water pool characteristics. Heat from the reactor vessel is transferred to the RCCS by radiation, natural convection, and conduction. The data provided by these experiments are basis for validation CFD calculations specific to the behavior of water-cooled RCCS.

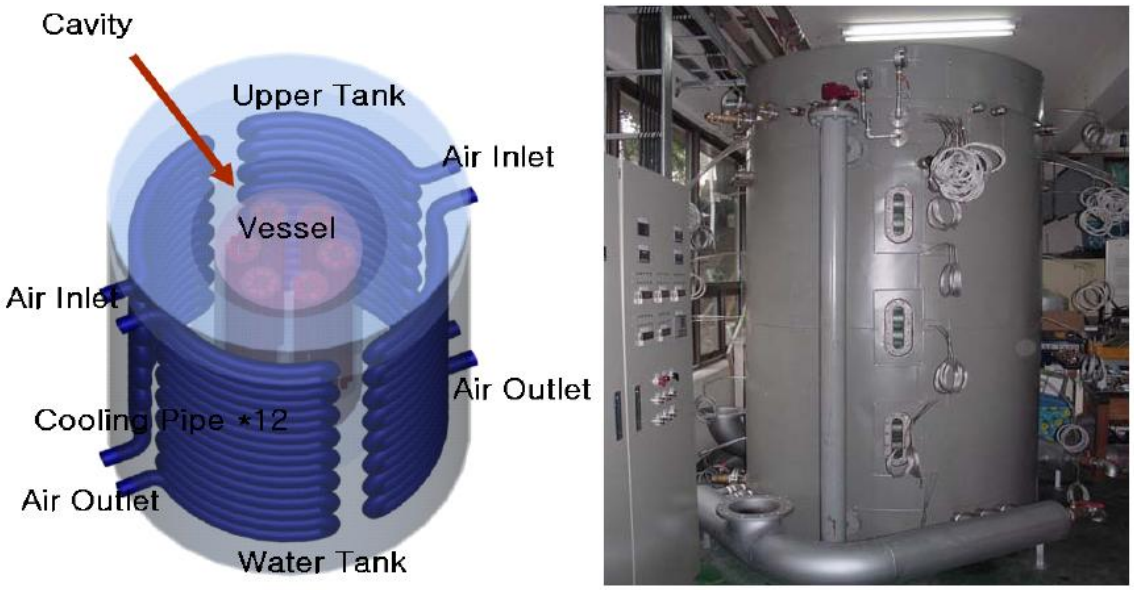

a. Schematic of test facility

b. Photograph of test facility

Fig. 7 – SNU water-cooled RCCS experiment

3.3 Larger Scale Vessel Experiments and Prototypical Concept Experiments

Code development and assessment activities for other reactor designs have required integral experiments at various scales to verify that small-scale laboratory experiments, experiments using simulated fluids, and experiments at non-rated conditions have been

properly scaled for the full-scale plant. This premise also holds true for any VHTR design.

Two approaches will be used to obtain applicable integral facility data to validate the software for NGNP VHTR. The first will be to use existing data from the High-Temperature Engineering Test Reactor (HTTR) and/or the Chinese High Temperature Gas-Cooled Reactor (HTR-10) research reactors. The second will be to build integral facilities based on need.

3.3.1 Integral Reactor Experiments – HTTR and HTR-10

Presently there are two operational gas-cooled test reactors: the HTR-10 and the HTTR. These experiments are located in Beijing, China at the Institute of Nuclear Energy Technology (INET) and in Oarai, Japan, at Japan Atomic Energy Agency (JAEA), respectively. Integral experiments are the only experimental sources that may be able to produce the complex interactions between dominant phenomena identified in the VHTR system specific PIRT. Therefore, the integral experiments are essential for systems analysis and CFD code validation studies. Undoubtedly data from both the HTTR and the HTR-10 will be included in the calculational matrix required for plant licensing by the NRC. In Fig. 8 and Fig. 9 are shown the schematic of the HTR-10 and HTTR respectively.

The HTR-10 is a 10 MW pebble bed high temperature gas-cooled reactor that became operational in 2000. INET plans to perform a spectrum of experiments essential to the VHTR project. Among the experiments may be a LOCA, a pressurized conduction

cooldown experiment, a rod ejection experiment, and an anticipated transient without scram.

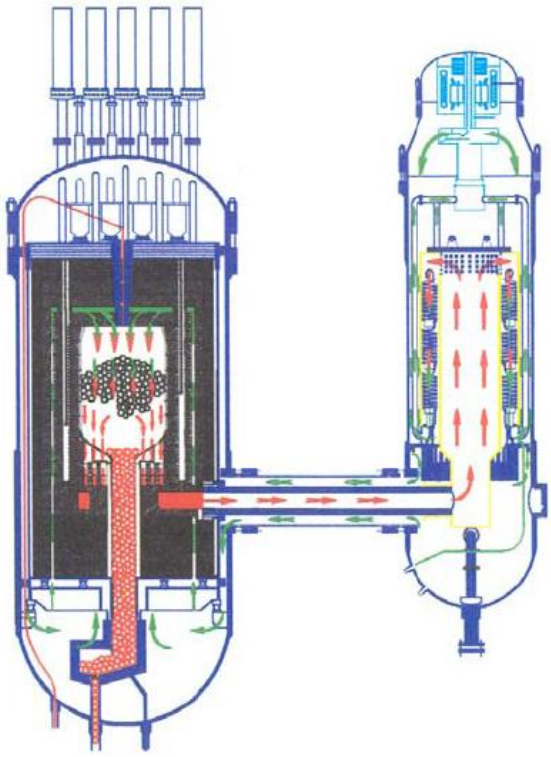

Fig. 8 – Schematic of the HTR-10

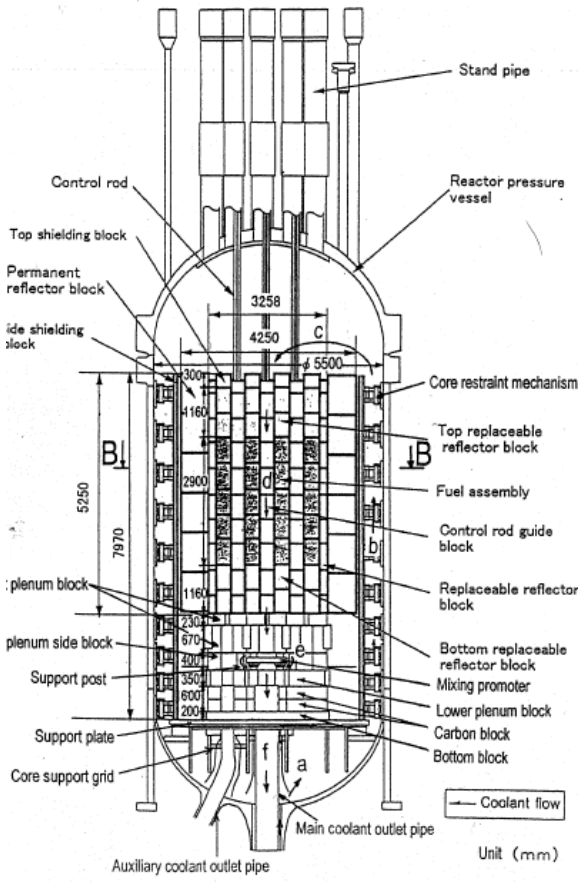

Fig. 9 – Schematic of the HTTR

The HTR-10 reactor vessel (see Fig. 8) is approximately 11.2 m in height and contains a 1.8 m diameter core that is 1.97 m high with ~ 27,000 pebbles. The reactor was designed to operate at 10 MWt. The average power density is 2 MW/m^3. The core inlet temperature is 250 to 300 °C, and the core outlet temperature will range from 700 to 900 °C. Benchmark experiments performed in the HTR-10 are available via International Atomic Energy Agency (IAEA).

The HTTR project is centered on the 30 MWt prismatic engineering test reactor (see Fig. 9). The HTTR project also has a number of support projects that provide useful data

(e.g., the Vessel Cooling System test series based on cooling panels inside a vessel containing heating elements). JAEA plans to perform a spectrum of HTTR experiments that may include a LOCA, a pressurized conduction cooldown experiment, a rod ejection experiment, and an anticipated transient without scram.

The HTTR became operational in 1998. The reactor vessel is 13.2 m tall (inner dimension) and has a 5.5 m inner diameter. The core has 30 fuel columns and 7 control rod guide columns. There are 12 replaceable reflector columns and 9 control rod guide columns. The HTTR is fitted with an RCCS. The HTTR operates at 4 MPa with a core inlet temperature of 395 °C and an outlet temperature of 850 °C, as shown in the IAEA report (2000). Cooling panels were placed inside a pressure vessel and experiments were performed by varying the gas in the reactor pressure vessel to change the natural convection characteristics.

3.4 Texas A&M University RCCS Facility

A simple small test facility was constructed at Texas A&M University [Capone et al. (2010)] to measure the temperature distributions in the RCCS cavity. The vessel was made of copper and electrically heated via electrodes. The flange for the connection of the top and bottom parts of the pressure vessel was taken into account. The external box (resembling the RCCS concrete walls) was made of glass, and aluminum rising pipes (i.e., standpipes) were placed inside the cavity. A movable rack with thermocouples was used to measure the axial temperature profile inside the cavity. This allowed temperature measuring at various radial positions from the vessel wall. The air in the region between

the vessel and the standpipes is at ambient pressure. In Fig. 10 is shown the RCCS model of the experimental facility.

In Fig. 11 is shown the rack plane location for temperature measurement in the RCCS cavity. As the figure shows, the rack plane can be moved radially from the RPV wall to the gap between the central standpipe and the adjacent one in such a way to have temperature measurements along the cavity height at different distances from the RPV wall, and in the gap between the standpipes.

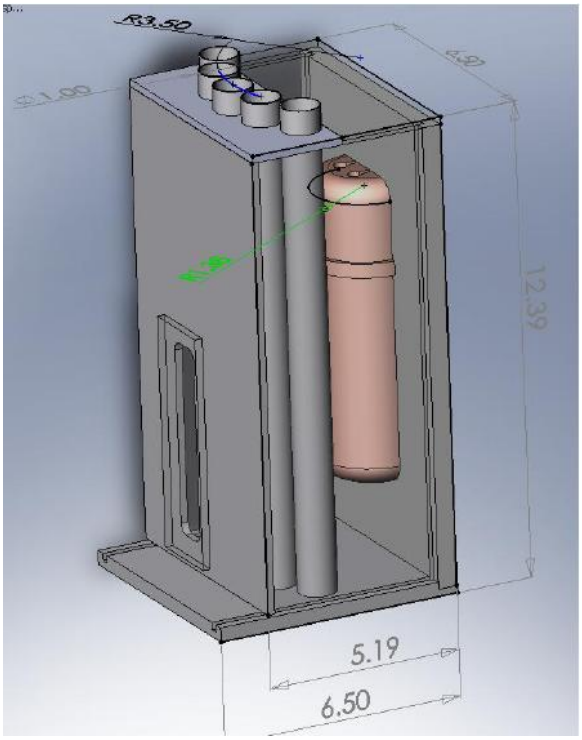

Fig. 10 – Model of the Texas A&M University RCCS experimental facility

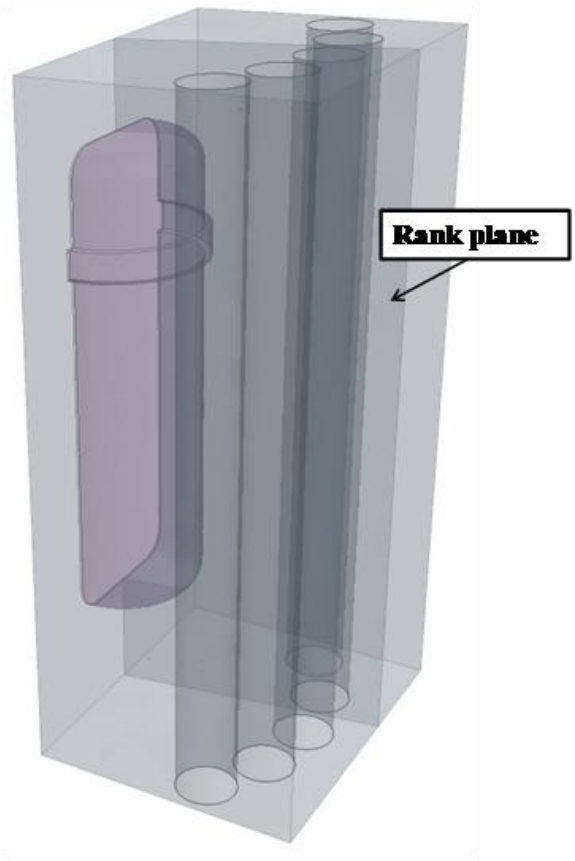

Fig. 11 –Texas A&M University RCCS experimental facility rack plane location

The five standpipes were realized with an internal tube representing the downcomer and an external tube representing the riser. The cooling fluid (air or water depending on the RCCS configuration chosen) enters the inner tube (i.e., the downcomer) flowing downwards. Close to the bottom of the cavity two opening per standpipe on the inner tube surface allow the cooling fluid to be directed in the annulus between the inner and outer tubes. Due to buoyancy forces, the fluid moves upwards in the riser cooling the standpipes in such a way to reduce the temperature at the RPV wall.

4. SCALING ANALYSIS OF THE TEXAS A&M RCCS EXPERIMENTAL FACILITY

A scaling analysis of the RCCS Texas A&M University experimental facility was performed to demonstrate that the mockup built well addresses the main physical phenomena in the RCCS cavity for both the water-cooled and air-cooled configurations. Since no analytical information is available on the performance of a reference water-cooled and/or air-cooled RCCS, the scaling analysis presented here had the dual goal of showing the ability of the experimental facility in addressing the physics inside the RCCS cavity and the standpipes, and benchmarking CFD codes against experimental data. The analysis of the RCCS performance by CFD codes presents a number of challenging aspects as strong 3D effects in the RCCS cavity region and inside the standpipes, simulation of turbulence in flows characterized by natural circulation, high Rayleigh numbers and low Reynolds numbers, boundary layer separation and reattachment phenomena, radiation in very complex geometries, the potential of nucleate boiling in the tubes of the water-cooled configuration, very strong temperature gradients close to the vessel wall which require an accurate modeling for the change of air properties with temperature, etc.

In the following sections are presented the non-dimensional conservation equations, from which it is possible to determine the similarity groups that describe the underlying physics of the RCCS cavity and the standpipes for both the real plant and the scaled facility.

4.1 RCCS Non-Dimensional Conservation Equations

4.1.1 RCCS Standpipes Similarity Groups

In this section the simplified one-dimensional momentum equation and energy equation are presented for the standpipes in the RCCS cavity. The equations were non-dimensionalized to determine the similarity groups relevant to address the distortion effects of the scaling from the real plant configuration down to the experimental facility. The analysis was carried out considering only the RCCS at steady state conditions. The integral momentum equation in the standpipes side of the RCCS can be written as:

$$p_{in} + \int_0^{L_h} \left(\rho g dL\right)_d = p_{out} + \int_0^{L_h} \left(\rho g dL\right)_u + \delta p_f + \delta p_l \tag{1}$$

The integral on the left side of eq. (1) is the gravitational head of the cold leg in the heated section (i.e., standpipes downcomer), and the integral on the right side is the gravitational head of the hot leg in the same section (i.e., standpipes riser). The frictional pressure drop in the *i* th section can be written as:

$$\delta p_{f,i} = \frac{1}{2D_i} f_i \rho_i U_i^2 L_i \tag{2}$$

The form pressure losses in the *i* th section can be written as:

$$\delta p_{l,i} = \frac{1}{2} K_i \rho_i U_i^2 \tag{3}$$

where K_i is the localized pressure loss coefficient in the *i* th section. The Boussinesq approximation can be used to link the change in temperature to change in density for the fluid:

$$\rho(T) = \rho_0 \left[1 - \beta (T - T_0)\right] \tag{4}$$

where ρ_0 is the reference density, β is the volumetric coefficient of thermal expansion and T_0 is the reference temperature. The non-dimensional temperature θ is defined in terms of a characteristic temperature rise, T_r-T_0, as:

$$\theta = \frac{(T - T_0)}{(T_r - T_0)} \tag{5}$$

Using eq. (4) and eq. (5), it is possible to write the density as function of the non-dimensional temperature θ:

$$\rho(\theta) = \rho_0 \left[1 - \beta\theta (T_r - T_0)\right] = \rho_0 - \rho_0 \beta\theta (T_r - T_0) \tag{6}$$

Considering the integral momentum equation between the inlet and outlet sections of the heated region, eq. (1) can be written as:

$$\begin{aligned} & p_{in} - p_{out} + \int_0^{L_h} \left(\left[\rho_0 - \rho_0 \beta\theta (T_r - T_0) \right] g dL \right)_d = \\ & = \int_0^{L_h} \left(\left[\rho_0 - \rho_0 \beta\theta (T_r - T_0) \right] g dL \right)_u + \frac{1}{2} \sum_i \frac{f_i \rho_i U_i^2 L_i}{D_i} + \frac{1}{2} \sum_i K_i \rho_i U_i^2 \end{aligned} \tag{7}$$

After rearrangement, eq. (7) can be written as:

$$\begin{aligned} & p_{in} - p_{out} - \rho_0 g \beta (T_r - T_0) \int_0^{L_h} (\theta dL)_d = \\ & = -\rho_0 g \beta (T_r - T_0) \int_0^{L_h} (\theta dL)_u + \frac{1}{2} \sum_i \frac{f_i \rho_i U_i^2 L_i}{D_i} + \frac{1}{2} \sum_i K_i \rho_i U_i^2 \end{aligned} \tag{8}$$

Defining a characteristic velocity U_0 and a characteristic length L_r, and dividing both sides of eq. (8) by the term $\rho_0 U_0^2$, the non-dimensional integral momentum equation is obtained:

$$\frac{\Delta p}{\rho_0 U_0^2} - \frac{g\beta\left(T_r - T_0\right)L_r}{U_0^2}\int_0^{l_h}\left(\theta dl\right)_d = \\ = -\frac{g\beta\left(T_r - T_0\right)L_r}{U_0^2}\int_0^{l_h}\left(\theta dl\right)_u + \frac{1}{2\rho_0}\sum_i\left[\frac{f_i\rho_i u_i^2 l_i}{d_i} + K_i\rho_i u_i^2\right] \tag{9}$$

where:

$$l_i = \frac{L_i}{L_r}, u_i = \frac{U_i}{U_0}, d_i = \frac{D_i}{L_r} \tag{10}$$

The Richardson number *Ri* is defined as:

$$Ri = \frac{g\beta\left(T_r - T_0\right)L_r}{U_0^2} = \left(\frac{g\left(T_r - T_0\right)L_r}{U_0^2}\right)\cdot\left(-\frac{1}{\rho_0}\frac{\Delta\rho}{\Delta T}\right) = \frac{g\left|\Delta\rho\right|L_r}{\rho_0 U_0^2} = \frac{buoyancy\ forces}{inertia\ forces} \tag{11}$$

Using eq. (11), it is possible to rewrite eq. (9) as:

$$\Delta P + Ri\left[\int_0^{l_h}\left(\theta dl\right)_u - \int_0^{l_h}\left(\theta dl\right)_d\right] = \frac{1}{2\rho_0}\sum_i\left[\frac{f_i\rho_i u_i^2 l_i}{d_i} + K_i\rho_i u_i^2\right] \tag{12}$$

where $\Delta P = \frac{\Delta p}{\rho_0 U_0^2}$. The energy equation for the fluid in the inner pipe (i.e., the downcomer) can be written as:

$$\frac{\pi}{4}D_{Ip}^2 U\rho c_p\frac{\partial T_I}{\partial Z} = \pi D_{Ip}h_I\left(T_{sI} - T_I\right) \tag{13}$$

Eq. (13) can be written as:

$$U\rho c_p\frac{\partial T_I}{\partial Z} = \frac{4h_I}{D_{Ip}}\left(T_{sI} - T_I\right) \tag{14}$$

Defining the non-dimensional variables:

$$z = \frac{Z}{L_r}, u = \frac{U}{U_0} \tag{15}$$

the non-dimensional energy equation can be written as:

$$u\frac{\partial \theta_I}{\partial z} = \frac{4h_I L_r}{\rho c_p U_0 D_{Ip}}\left(\theta_{sI} - \theta_I\right) \tag{16}$$

The definition of the Stanton number is:

$$St_I = \frac{4h_I L_r}{\rho c_p U_0 D_{Ip}} = \frac{h_I \pi D_{Ip} L_r \Delta T}{\rho c_p U_0 \pi \frac{D_{Ip}^2}{4}\Delta T} = \frac{h_I A_c \Delta T}{\dot{m} A_0 \Delta T} = \frac{heat\ transfered\ to\ the\ fluid}{thermal\ capacity\ of\ the\ fluid} \tag{17}$$

Using eq. (17), the non-dimensional energy equation can be written as:

$$u\frac{\partial \theta_I}{\partial z} = St_I\left(\theta_{sI} - \theta_I\right) \tag{18}$$

The energy equation for the annulus between the tubes is:

$$A_\alpha U \rho c_p \frac{\partial T_\alpha}{\partial Z} = P_e h_e \left(T_{se} - T_e\right) - P_I h_{IO}\left(T_e - T_{sI}\right) \tag{19}$$

Defining the modified Stanton numbers for the outer and inner walls of the annulus:

$$St_e = \frac{P_e h_e L_r}{\rho c_p U_0 A_\alpha} \tag{20}$$

$$St_\alpha = \frac{P_I h_{IO} L_r}{\rho c_p U_0 A_\alpha} \tag{21}$$

the energy equation for the annulus between the tubes can be non-dimensionalized as:

$$u\frac{\partial \theta_\alpha}{\partial z} = St_e\left(\theta_{se} - \theta_e\right) - St_\alpha\left(\theta_e - \theta_{sI}\right) \tag{22}$$

4.1.2 RCCS Cavity Region Similarity Groups

Using the symmetry of the RCCS cavity, it is possible to assimilate its geometry to a rectangular two-dimensional cavity with one vertical wall heated, the other vertical wall

cooled, and the two horizontal walls insulated. The conservation of mass, momentum and energy equations can be written as:

$$\frac{\partial W}{\partial Z}+\frac{\partial V}{\partial Y}=0 \tag{23}$$

$$\rho\left(W\frac{\partial W}{\partial Z}+V\frac{\partial W}{\partial Y}\right)=-\frac{\partial P}{\partial Z}-\rho_0 g\left[1-\beta\left(T-T_0\right)\right]+\mu\left(\frac{\partial^2 W}{\partial Z^2}+\frac{\partial^2 W}{\partial Y^2}\right) \tag{24}$$

$$\rho\left(W\frac{\partial V}{\partial Z}+V\frac{\partial V}{\partial Y}\right)=-\frac{\partial P}{\partial Y}+\mu\left(\frac{\partial^2 V}{\partial Z^2}+\frac{\partial^2 V}{\partial Y^2}\right) \tag{25}$$

$$\rho c_p\left(W\frac{\partial T}{\partial Z}+V\frac{\partial T}{\partial Y}\right)=k\left(\frac{\partial^2 T}{\partial Z^2}+\frac{\partial^2 T}{\partial Y^2}\right) \tag{26}$$

where P is the pressure, W and V are the velocity component in the vertical and horizontal direction respectively, and ρ_0 is the density at the reference temperature T_0. The following non-dimensional variables are defined:

$$z=\frac{Z}{H}, y=\frac{Y}{H}, w=\frac{W}{u^*}, v=\frac{V}{u^*}, p=\frac{P+\rho_0 gZ}{\rho u^{*2}}, \theta=\frac{T-T_0}{T_h-T_c} \tag{27}$$

where T_h and T_c are the average temperature of the RPV wall and the standpipes external wall, respectively. Eqs. (23) – (26) can be written in non-dimensional form as:

$$\frac{u^*}{H}\left(\frac{\partial w}{\partial z}+\frac{\partial v}{\partial y}\right)=0 \tag{28}$$

$$\frac{\rho u^{*2}}{H}\left(w\frac{\partial w}{\partial z}+v\frac{\partial w}{\partial y}\right)=-\frac{\partial P}{\partial Z}-\rho_0 g+\rho_0 g\beta\left(T_h-T_c\right)\theta+\frac{\mu u^*}{H^2}\left(\frac{\partial^2 w}{\partial z^2}+\frac{\partial^2 w}{\partial y^2}\right) \tag{29}$$

$$\frac{\rho u^{*2}}{H}\left(w\frac{\partial v}{\partial z}+v\frac{\partial v}{\partial y}\right)=-\frac{\partial P}{\partial Y}+\frac{\mu u^*}{H^2}\left(\frac{\partial^2 v}{\partial z^2}+\frac{\partial^2 v}{\partial y^2}\right) \tag{30}$$

$$\frac{\rho c_p u^* \left(T_h - T_c\right)}{H}\left(w\frac{\partial\theta}{\partial z} + v\frac{\partial\theta}{\partial y}\right) = \frac{k\left(T_h - T_c\right)}{H^2}\left(\frac{\partial^2\theta}{\partial z^2} + \frac{\partial^2\theta}{\partial y^2}\right) \tag{31}$$

After rearrangement, eqs. (28) – (31) can be written as:

$$\frac{\partial w}{\partial z} + \frac{\partial v}{\partial y} = 0 \tag{32}$$

$$w\frac{\partial w}{\partial z} + v\frac{\partial w}{\partial y} = -H\frac{\partial\left(\frac{P + \rho_0 gZ}{\rho u^{*^2}}\right)}{\partial Z} + \frac{g\beta\left(T_h - T_c\right)H}{u^{*^2}}\theta + \frac{H}{\rho u^{*^2}}\frac{\mu u^*}{H^2}\left(\frac{\partial^2 w}{\partial z^2} + \frac{\partial^2 w}{\partial y^2}\right) \tag{33}$$

$$w\frac{\partial v}{\partial z} + v\frac{\partial v}{\partial y} = -H\frac{\partial\left(\frac{P + \rho_0 gZ}{\rho u^{*^2}}\right)}{\partial Y} + \frac{H}{\rho u^{*^2}}\frac{\mu u^*}{H^2}\left(\frac{\partial^2 v}{\partial z^2} + \frac{\partial^2 v}{\partial y^2}\right) \tag{34}$$

$$w\frac{\partial\theta}{\partial z} + v\frac{\partial\theta}{\partial y} = \frac{H}{\rho c_p u^*\left(T_h - T_c\right)}\frac{k\left(T_h - T_c\right)}{H^2}\left(\frac{\partial^2\theta}{\partial z^2} + \frac{\partial^2\theta}{\partial y^2}\right) \tag{35}$$

Considering the non-dimensional variables defined in eq. (27), and simplifying eqs. (33) – (35), it is possible to obtain:

$$w\frac{\partial w}{\partial z} + v\frac{\partial w}{\partial y} = -\frac{\partial p}{\partial z} + \frac{g\beta\left(T_h - T_c\right)H}{u^{*^2}}\theta + \frac{\mu}{\rho u^* H}\left(\frac{\partial^2 w}{\partial z^2} + \frac{\partial^2 w}{\partial y^2}\right) \tag{36}$$

$$w\frac{\partial v}{\partial z} + v\frac{\partial v}{\partial y} = -\frac{\partial p}{\partial y} + \frac{\mu}{\rho u^* H}\left(\frac{\partial^2 v}{\partial z^2} + \frac{\partial^2 v}{\partial y^2}\right) \tag{37}$$

$$w\frac{\partial\theta}{\partial z} + v\frac{\partial\theta}{\partial y} = \frac{k}{\rho c_p u^* H}\left(\frac{\partial^2\theta}{\partial z^2} + \frac{\partial^2\theta}{\partial y^2}\right) \tag{38}$$

Forced/mixed/free convection is described by the non-dimensional Grashof number divided by the square of the non-dimensional Reynolds number:

$$\frac{Gr}{\mathrm{Re}^2}=\frac{\left(\dfrac{g\rho^2\beta\left(T_h-T_c\right)H^3}{\mu^2}\right)}{\left(\dfrac{\rho u^* H}{\mu}\right)^2}=\frac{g\beta\left(T_h-T_c\right)H}{u^{*2}}=\frac{g\left|\Delta\rho\right|H}{\rho_0 u^{*2}}=\frac{buoyancy\ forces}{inertia\ forces} \tag{39}$$

The Gr/Re^2 is the ratio between the buoyancy and the inertial forces. For large Gr/Re^2 (i.e. $Gr/Re^2>>1$) buoyancy forces prevails over inertial forces. This flow regime is called free convection. Vice versa, for small Gr/Re^2 (i.e., $Gr/Re^2<<1$) inertia forces prevail over buoyancy forces. In these conditions the flow is in forced convection. If Gr/Re^2 is of the order of unity, then mixed convection is present. Using the definition of *Gr* and *Re* numbers, eqs. (36) and (37) can be written as:

$$w\frac{\partial w}{\partial z}+v\frac{\partial w}{\partial y}=-\frac{\partial p}{\partial z}+\frac{Gr}{\mathrm{Re}^2}\theta+\frac{1}{\mathrm{Re}}\left(\frac{\partial^2 w}{\partial z^2}+\frac{\partial^2 w}{\partial y^2}\right) \tag{40}$$

$$w\frac{\partial v}{\partial z}+v\frac{\partial v}{\partial y}=-\frac{\partial p}{\partial y}+\frac{1}{\mathrm{Re}}\left(\frac{\partial^2 v}{\partial z^2}+\frac{\partial^2 v}{\partial y^2}\right) \tag{41}$$

If the Prandlt non-dimensional number *Pr* is introduced:

$$\mathrm{Pr}=\frac{\mu c_p}{k}=\frac{\mu}{\rho}\cdot\frac{\rho c_p}{k}=\frac{\nu}{\alpha}=\frac{molecular\ diffusivity}{thermal\ diffusivity} \tag{42}$$

then the product of the *Pr* number by the *Re* number gives the Peclet number *Pe*:

$$\mathrm{P}e=\mathrm{Re}\cdot\mathrm{Pr}=\frac{\rho u^* H}{\mu}\frac{\mu c_p}{k}=\frac{\rho c_p u^*\Delta T}{k\dfrac{\Delta T}{H}}=\frac{heat\ transfer\ by\ advection}{heat\ transfer\ by\ conduction} \tag{43}$$

Using the definition of the *Pe* number, eq. (38) can be rewritten as:

$$w\frac{\partial\theta}{\partial z}+v\frac{\partial\theta}{\partial y}=\frac{1}{Pe}\left(\frac{\partial^2\theta}{\partial z^2}+\frac{\partial^2\theta}{\partial y^2}\right) \tag{44}$$

The *Gr* number as written in eq. (39) can also be rearranged as:

$$Gr = \frac{g\rho^2\beta\left(T_h - T_c\right)H^3}{\mu^2} = \left(\frac{g\rho^2\left(T_h - T_c\right)H^3}{\mu^2}\right)\cdot\left(-\frac{1}{\rho}\frac{\Delta\rho}{\Delta T}\right) = \frac{g\rho\left|\Delta\rho\right|H^3}{\mu^2} = \frac{g\left|\Delta\rho\right|H}{\left(\frac{\mu^2}{\rho H^2}\right)} \quad (45)$$

The meaning of the *Gr* number is clear if we take a reference velocity such that the Re number is normalized to unity. Since the Re number is defined as:

$$\mathrm{Re} = \frac{\rho u^* H}{\mu} = \frac{\rho u^{*2}}{\mu\frac{u^*}{H}} = \frac{inertia\ forces}{viscous\ forces} \quad (46)$$

To have a *Re* number equal to one, the reference velocity *u** must be equal to:

$$\frac{\rho u^* H}{\mu} = 1 \Rightarrow u^* = \frac{\mu}{\rho H} \quad (47)$$

This means that we are implicitly assuming that inertia forces are of the same order of magnitude of viscous forces. Under this assumption, using eq. (47), eq. (45) can be written as:

$$Gr = \frac{g\left|\Delta\rho\right|H}{\left(\frac{\mu^2}{\rho H^2}\right)} = \frac{g\left|\Delta\rho\right|H}{\left(\frac{\mu}{H}\cdot\frac{\mu}{\rho H}\right)} = \frac{g\left|\Delta\rho\right|H}{\left(\frac{\mu}{H}\cdot u^*\right)} = \frac{buoyancy\ forces}{viscous\ forces} \quad (48)$$

Therefore, under the conditions that inertia forces are of the same order of magnitude of viscous forces, the *Gr* number gives the ratio of buoyancy forces over viscous forces, where buoyancy forces are the driving phenomenon, and viscous forces are the dissipative phenomenon.

Using the definition of *Gr* number, another non-dimensional group used to describe the convection regime is the Rayleigh number *Ra*, which is defined as:

$$Ra = Gr \cdot \mathrm{Pr} = \left(\frac{g\rho^2 \beta \left(T_h - T_c\right) H^3}{\mu^2} \right) \cdot \left(\frac{\mu c_p}{k} \right) = \frac{c_p g \rho^2 \beta \left(T_h - T_c\right) H^3}{\mu k} \tag{49}$$

The Ra number still represents a ratio between buoyancy forces (i.e., the driving phenomenon in free convection) and viscous forces (i.e., the dissipative phenomenon).

The heat transferred from the reactor vessel to the RCCS cavity at time *t*, *Q(t)*, can be roughly approximated by:

$$Q(t) = A_c h_{cav} \left(T_h - T_c\right) + A_{rad} \varepsilon \sigma \left(T_h^4 - T_c^4\right) \tag{50}$$

where A_c and A_{rad} are the equivalent areas of heat transfer by convection and radiation, respectively; h_{cav} is the reactor cavity heat transfer coefficient by convection; T_h is the average temperature of the reactor vessel wall, and T_c is the average temperature of the external standpipes surface; σ is the Stefan-Boltzmann constant, and ε is the surface emissivity. At steady-state conditions:

$$Q(0) = Q_0 = A_\alpha U_0 \rho_0 c_p \left(T_r - T_0\right) \tag{51}$$

where the product $A_\alpha U_0 \rho_0$ is the total mass flow rate throughout all the standpipes available, T_0 and T_r are the inlet and outlet temperature respectively at the heated section of the standpipes. Eq. (50) can be written in a non-dimensional form by using eq. (51) as:

$$\frac{Q(t)}{A_\alpha U_0 \rho_0 c_p \left(T_r - T_0\right)} = f(t) = \frac{A_c h_{cav} \left(T_h - T_c\right)}{A_\alpha U_0 \rho_0 c_p \left(T_r - T_0\right)} + \frac{A_{rad} \varepsilon \sigma \left(T_h^4 - T_c^4\right)}{A_\alpha U_0 \rho_o c_p \left(T_r - T_0\right)} \tag{52}$$

Considering the non-dimensional temperature θ [see eq. (5)], eq. (52) can be written as:

$$f(t)=\frac{A_c h_{cav}}{A_\alpha U_0 \rho_0 c_p}(\theta_h-\theta_c)+\frac{A_{rad}\varepsilon\sigma T_0^4}{A_\alpha U_0 \rho_0 c_p (T_r-T_0)}\left\{\left[\theta_h\left(\frac{T_r}{T_0}-1\right)+1\right]^4-\left[\theta_c\left(\frac{T_r}{T_0}-1\right)+1\right]^4\right\} \quad (53)$$

Eq. (53) introduces three non-dimensional groups:

$$N_c=\frac{A_c h_{cav}}{A_\alpha U_0 \rho_0 c_p}, N_r=\frac{A_{rad}\varepsilon\sigma T_0^4}{A_\alpha U_0 \rho_0 c_p (T_r-T_0)}, N_t=\left(\frac{T_r}{T_0}-1\right) \quad (54)$$

which represent the cavity convective number, the cavity radiation number and the temperature ratio number, respectively.

Considering eq. (51), it is possible to relate the reference change in water/air temperature between the inlet and outlet standpipes sections and the heat transferred from the reactor vessel to the RCCS cavity:

$$(T_r-T_0)=\frac{Q_0}{A_\alpha U_0 \rho_0 c_p} \quad (55)$$

The Richardson number *Ri* can be written using eq. (55) as:

$$Ri=\frac{g\beta(T_r-T_0)L_r}{U_0^2}=\frac{g\beta L_r}{U_0^2}\frac{Q_0}{A_\alpha U_0 \rho_0 c_p}=\frac{g\beta L_r Q_0}{A_\alpha \rho_0 c_p U_0^3} \quad (56)$$

The cavity radiation number can be written using eq. (55) as:

$$N_r=\frac{A_{rad}\varepsilon\sigma T_0^4}{A_\alpha U_0 \rho_0 c_p (T_r-T_0)}=\frac{A_{rad}\varepsilon\sigma T_0^4}{A_\alpha U_0 \rho_0 c_p}\frac{A_\alpha U_0 \rho_0 c_p}{Q_0}=\frac{A_{rad}\varepsilon\sigma T_0^4}{Q_0} \quad (57)$$

The temperature ratio number N_t can be written using eq. (55) as:

$$N_t=\left(\frac{T_r}{T_o}-1\right)=\frac{(T_r-T_0)}{T_0}=\frac{Q_0}{T_0 A_\alpha U_0 \rho_0 c_p} \quad (58)$$

In conclusion we obtain ten independent similarity groups:

1. $Ri = \frac{g\beta L_r Q_0}{A_\alpha \rho_0 c_p U_0^3}$;

2. $St_I = \frac{4h_I L_r}{\rho c_p U_0 D_{Ip}}$;

3. $St_e = \frac{P_e h_e L_r}{\rho c_p U_0 A_\alpha}$;

4. $St_\alpha = \frac{P_I h_{IO} L_r}{\rho c_p U_0 A_\alpha}$;

5. $\frac{Gr}{\mathrm{Re}^2} = \frac{g\beta(T_h - T_c)H}{u^{*2}}$; or $Ra = \frac{c_p g \rho^2 \beta (T_h - T_c) H^3}{\mu k}$ *if we assume* $u^* = \frac{\mu}{\rho H}$;

6. $\mathrm{P}e = \mathrm{Re}\cdot \mathrm{Pr} = \frac{\rho c_p u^* H}{k}$;

7. $\mathrm{Re} = \left(\frac{\rho u^* H}{\mu}\right)$;

8. $N_c = \frac{A_c h_{cav}}{A_\alpha U_0 \rho_0 c_p}$;

9. $N_r = \frac{A_{rad}\varepsilon\sigma T_0^4}{Q_0}$;

10. $N_t = \frac{Q_0}{T_0 A_\alpha U_0 \rho_0 c_p}$;

Using the definition of the Nusselt number and the Dittus-Boelter correlation for the heat exchange coefficient at the wall of circular tubes:

$$Nu = \frac{hD}{k} = 0.023\cdot \mathrm{Re}^{0.8}\cdot \mathrm{Pr}^{0.4} = \frac{k}{D}\cdot 0.023\cdot \left(\frac{\rho U_o D}{\mu}\right)^{0.8}\left(\frac{\mu c_p}{k}\right)^{0.4} \quad (59)$$

$$h = \frac{k}{D} \cdot 0.023 \cdot \mathrm{Re}^{0.8} \cdot \mathrm{Pr}^{0.4} = \frac{k}{D} \cdot 0.023 \cdot \left(\frac{\rho U_o D}{\mu} \right)^{0.8} \left(\frac{\mu c_p}{k} \right)^{0.4} \quad (60)$$

where D is the hydraulic diameter defined as $D=4A/P_w$, and P_w is the wetted perimeter. Using eq. (60), it is possible to write the heat transfer coefficients at the inner tube wall h_I, the heat transfer coefficient at the annulus external wall h_e, and the heat transfer coefficient at the annulus inner wall h_{IO} as functions of the *Re* and *Pr* numbers. Therefore, the ten similarity groups contain twelve independent parameters:

$$Q_0, L_r, U_0, P_e = \pi D_3, P_I = \pi D_2, \left(T_h - T_c\right), D_{Ip}, u^*, h_{cav}, A_{cav}, A_{rad}, T_0$$

4.1.3 Simplified Analysis of RCCS Similarity Groups

A simplified geometry for the standpipes is considered, where the effect of the downcomer in the standpipes is neglected, and the water flows upwards in the annulus along the heated section. In this simplified geometry the similarity groups reduce to 8, which are:

1. $Ri = \dfrac{g \beta L_r Q_0}{A_\alpha \rho_0 c_p U_0^3}$;
2. $St_e = \dfrac{P_e h_e L_r}{\rho c_p U_0 A_\alpha}$;
3. $\dfrac{Gr}{\mathrm{Re}^2} = \dfrac{g \beta \left(T_h - T_c\right) H}{u^{*2}}$; or $Ra = \dfrac{c_p g \rho^2 \beta \left(T_h - T_c\right) H^3}{\mu k}$ *if we assume* $u^* = \dfrac{\mu}{\rho H}$;
4. $\mathrm{P}e = \mathrm{Re} \cdot \mathrm{Pr} = \dfrac{\rho c_p u^* H}{k}$;

5. $\mathrm{Re} = \left(\frac{\rho u^* H}{\mu} \right)$;

6. $N_c = \frac{A_c h_{cav}}{A_\alpha U_0 \rho_0 c_p}$;

7. $N_r = \frac{A_{rad} \varepsilon \sigma T_0^4}{Q_0}$;

8. $N_t = \frac{Q_0}{T_o A_\alpha U_0 \rho_0 c_p}$;

The eleven independent parameters are:

$$Q_0, L_r, U_0, P_e = \pi D_3, P_I = \pi D_2, \left(T_h - T_c\right), u^*, h_{cav}, A_{cav}, A_{rad}, T_0$$

4.2 Scaling Analysis of the RCCS Experimental Facility

Once similarity groups are determined for the physics of the problem under consideration, the objective of the scaling procedure is to determine the experimental facility geometrical dimensions and working conditions which would give similarity groups values very close to those obtained for the plant working conditions. This means that the goal of a scaling procedure is to obtain a unity ratio of as many as possible similarity groups between the experimental facility (Π_m) and the real plant (Π_p):

$$\Pi_R = \frac{\Pi_m}{\Pi_p} \tag{61}$$

Considering the 8 similarity groups identified in Section 4.1.3, the ratio between the experimental and the plant values gives:

$$Ri_R = \frac{Ri_m}{Ri_p} = \frac{\left(\frac{g\beta L_r Q_0}{A_\alpha \rho_0 c_p U_0^3}\right)_m}{\left(\frac{g\beta L_r Q_0}{A_\alpha \rho_0 c_p U_0^3}\right)_p} = \frac{L_{rR} Q_{0R}}{A_{\alpha R} U_{0R}^3} = \frac{L_{hR} Q_{0R}}{A_{\alpha R} U_{0R}^3} \tag{62}$$

$$St_{eR} = \frac{St_{em}}{St_{ep}} = \frac{\left(\frac{P_e h_e L_r}{\rho c_p U_0 A_\alpha}\right)_m}{\left(\frac{P_e h_e L_r}{\rho c_p U_0 A_\alpha}\right)_p} = \frac{P_{eR} h_{eR} L_{hR}}{U_{0R} A_{\alpha R}} \tag{63}$$

Considering eq. (60), h_{eR} can be written as:

$$h_{eR} = \frac{h_{em}}{h_{ep}} = \frac{\left[\frac{k}{D_m} \cdot 0.023 \cdot \left(\frac{\rho U_0 D_m}{\mu}\right)^{0.8} \left(\frac{\mu c_p}{k}\right)^{0.4}\right]_m}{\left[\frac{k}{D_p} \cdot 0.023 \cdot \left(\frac{\rho U_0 D_p}{\mu}\right)^{0.8} \left(\frac{\mu c_p}{k}\right)^{0.4}\right]_p} = U_{0R}^{0.8} D_R^{-0.2} \tag{64}$$

which gives for the Stanton number ratio:

$$St_{eR} = \frac{P_{eR} L_{hR}}{U_{0R} A_{\alpha R}} U_{0R}^{0.8} D_R^{-0.2} = \frac{P_{eR} L_{hR} U_{0R}^{-0.2} D_R^{-0.2}}{A_{\alpha R}} \tag{65}$$

$$\left(\frac{Gr}{\mathrm{Re}^2}\right)_R = \frac{\left(\frac{g\beta(T_h - T_c)H}{u^{*2}}\right)_m}{\left(\frac{g\beta(T_h - T_c)H}{u^{*2}}\right)_p} = \frac{(T_h - T_c)_R L_{hR}}{u_R^{*2}} \tag{66}$$

or:

$$Ra_R = \frac{\left(\frac{c_p g \rho^2 \beta (T_h - T_c) H^3}{\mu k}\right)_m}{\left(\frac{c_p g \rho^2 \beta (T_h - T_c) H^3}{\mu k}\right)_p} = (T_h - T_c)_R L_{hR}^3 \tag{67}$$

$$\mathrm{P}e_R = \frac{\left(\frac{\rho c_p u^* H}{k}\right)_m}{\left(\frac{\rho c_p u^* H}{k}\right)_p} = u_R^* L_{hR} = \mathrm{Re}_R \tag{68}$$

The implicit assumption made for eq. (62) throughout eq. (65) was that the coolant used for the model standpipes is the same as that used for the prototype. Also it was assumed that in eq. (66) throughout eq. (68) the air condition in the cavity for the plant and the experiment are the same. With the assumptions made the *Pr* number for the plant and the experiment are the same, and since *Pe=Re*Pr*, the ratio between the Peclet number in the plant and experiment is the same as the ratio of the Reynolds number. Since the air density, dynamic viscosity and thermal conductivity are all temperature dependent properties, only if the temperature distribution in the RCCS cavity is the same for the real plant and the experimental facility it is possible to assume that the Pr number is the same for both configurations. These considerations apply as well for the air in the standpipes when the air-cooled RCCS configuration is considered. On the other hand, for the standpipes in the RCCS water-cooled configuration, it is expected a negligible change of the water properties, since the temperature gradient across the heated part of the standpipes is of few degrees. This means that the standpipes coolant properties for the mockup are very close to those of the real plant standpipes, and no assumptions were needed.

It is also necessary to point out that eq. (66) and eq. (67) are not independent. Equation (67) can be derived from eq. (66) if the *Re* number is set equal to unity for both the plant and the experiment. For $Re_m = Re_p = 1$, using eq. (68) we have:

$$\mathrm{Re}_R = u_R^* L_{hR} = 1 \Rightarrow u_R^* = \frac{1}{L_{hR}} \tag{69}$$

Plugging eq. (69) into eq. (66) we obtain exactly eq. (67), which is:

$$\left(\frac{Gr}{\mathrm{Re}^2}\right)_R = \frac{\left(T_h - T_c\right)_R L_{hR}}{u_R^{*2}} = \frac{\left(T_h - T_c\right)_R L_{hR}}{\left(\frac{1}{L_{hR}^2}\right)} = \left(T_h - T_c\right)_R L_{hR}^3 = Ra_R \tag{70}$$

$$N_{cR} = \frac{\left(\frac{A_c h_{cav}}{A_\alpha U_0 \rho_0 c_p}\right)_m}{\left(\frac{A_c h_{cav}}{A_\alpha U_0 \rho_0 c_p}\right)_p} = \frac{A_{cR} h_{cavR}}{U_{0R} A_{\alpha R}} \tag{71}$$

$$N_{rR} = \frac{\left(\frac{A_{rad} \varepsilon \sigma T_0^4}{Q_0}\right)_m}{\left(\frac{A_{rad} \varepsilon \sigma T_0^4}{Q_0}\right)_p} = \frac{A_{radR} T_{0R}^4}{Q_{0R}} \tag{72}$$

$$N_{tR} = \frac{\left(\frac{Q_0}{T_o A_\alpha U_0 \rho_0 c_p}\right)_m}{\left(\frac{Q_0}{T_o A_\alpha U_0 \rho_0 c_p}\right)_p} = \frac{Q_{0R}}{U_{0R} A_\alpha T_{0R}} \tag{73}$$

Summarizing, the seven independent ratios of similarity groups are:

$$Ri_R = \frac{L_{hR} Q_{0R}}{A_{\alpha R} U_{0R}^3} \tag{74}$$

$$St_{eR} = \frac{P_{eR} U_{0R}^{-0.2} D_R^{-0.2} L_{hR}}{A_{\alpha R}} \tag{75}$$

$$\left(\frac{Gr}{\mathrm{Re}^2}\right)_R = \frac{\left(T_h - T_c\right)_R L_{hR}}{u_R^{*2}}, or\ Ra_R = \left(T_h - T_c\right)_R L_{hR}^3 \tag{76}$$

$$\mathrm{P}e_R = \mathrm{Re}_R = u_R^* L_{hR} \tag{77}$$

$$N_{cR} = \frac{A_{cR} h_{cavR}}{U_{0R} A_{\alpha R}} \tag{78}$$

$$N_{rR} = \frac{A_{radR} T_{0R}^4}{Q_{0R}} \tag{79}$$

$$N_{tR} = \frac{Q_{0R}}{U_{0R} A_{\alpha R} T_{0R}} \tag{80}$$

There are eleven independent variables and seven independent ratios of similarity groups. If the geometry of the experimental facility is fixed, then the variables L_r, D_3, D_2, u^*, h_{cav}, A_{cav} and A_{rad} become fixed, and the three independent variables are: Q_0, U_0, $(T_h - T_c)$ and T_0. As will be shown in the following sections, these independent parameters correspond to the boundary conditions to set for both the experimental facility and the CFD model. Therefore, the objective of the scaling analysis is to find the appropriate set of boundary conditions for the mockup/CFD model in such a way to satisfy as many as possible ratios of similarity groups.

4.3 Analyses on the Non-Dimensional Groups for the Water-Cooled and Air-Cooled RCCS Configurations

4.3.1 Sensitivity Analysis on the Standpipes Mass Flow Rate for the Water-Cooled RCCS Configuration

Experimental data were collected for different RCCS water-cooled standpipes volumetric flow rates and a fixed power generated inside the RPV region. CFD simulations were performed at the same boundary conditions set for the Texas A&M

University experimental facility in such a way to benchmark the code against experimental data. Another goal of the CFD simulations performed was to compare the performance of the RCCS cavity system for the scaled facility to those of the RCCS in the real plant configuration through the similarity groups identified in the scaling analysis. In Table 10 are shown the experimental data and the corresponding CFD simulations boundary conditions set for Test #1 through Test #7. In Table 11 are listed the plant [see IAEA (2000)] and experimental [see Capone et al. (2010)] independent parameters necessary to determine the ratio of the seven independent similarity groups eq. (74) – (80) for the water-cooled configuration. The non-dimensional analysis was performed for the case with standpipes volumetric flow equal to 1.0 gpm, which corresponds to Test #3.

Table 10 – Experimental/CFD simulations boundary conditions (Test#1-7)

Experimental/CFD simulation Test #	**RPW power generated (W)**	**Mass Flow Rate (kg/s) Volumetric flow[gpm]**	**U_0 (m/s)**
1	196.0	0.0/[0.0]	0.0
2	196.0	0.044/[0.7]	0.287
3	196.0	0.063/[1.0]	0.410
4	196.0	0.075/[1.2]	0.492
5	196.0	0.088/[1.4]	0.574
6	196.0	0.094/[1.5]	0.615
7	196.0	0.100/[1.6]	0.656

Table 11 – Plant/experiment independent parameters (water-cooled RCCS)

Scaling independent parameters	Plant	Experiment	Ratio Experiment/Plant
Q_0 (W)	1.22E6	196	1.606E-4
L_h (m)	28.0	0.29	1.036E-2
D_2 (m)	0.0	0.019	//
$D_3 = D_e$ (m)	0.049	0.0236	0.482
$P_e = \pi D_e$ (m)	0.1539	0.0741	0.482
$D_4 = D_{ext}$ (m)	0.057	0.0254	0.446
n standpipes	432	5	//
$A_\alpha = n*(\pi/4)*(D_3^2 - D_2^2)$ (m^2)	0.8146	0.00077	9.45E-4
hydraulic diameter $D=4A_\alpha/P_w$ (m^2)	0.049	0.0046	0.094
U_0 (m/s)	0.03627	0.410	11.304
T_c (K)	335.9	310.0	//
T_h (K)	573.0	560.0	//
T_h - T_c (K)	237.1	250.0	1.054
u^* (m/s)	3.92	0.35	0.089
h_{cav} (W/m^2 K)	30.0	950.0	31.667
$A_c = n*\pi*D_{ext}*H$ (m^2)	2166.04	0.1157	5.342E-5
$A_{radm} = n*(\pi/2)*D_{ext}*H$ (m^2)	1083.02	0.0578	5.342E-5
T_0 (K)	316.0	293.0	0.927
T_r (K)	325.895	293.149	//
$T_r - T_0$ (K)	9.895	0.149	0.015

Using the values given in Table 11, it is possible to determine the ratio of the independent similarity groups:

$$Ri_R = \frac{L_{hR} Q_{0R}}{A_{\alpha R} U_{0R}^3} = \frac{\left(1.036 \cdot 10^{-2}\right) \cdot \left(1.606 \cdot 10^{-4}\right)}{\left(9.45 \cdot 10^{-4}\right) \cdot \left(11.304\right)^3} = 1.219 \cdot 10^{-6} \tag{81}$$

$$St_{eR} = \frac{P_{eR} U_{0R}^{-0.2} D_R^{-0.2} L_{hR}}{A_{\alpha R}} = \frac{0.482 \cdot \left(11.304\right)^{-0.2} \cdot \left(0.094\right)^{-0.2} \cdot \left(1.036 \cdot 10^{-2}\right)}{9.45 \cdot 10^{-4}} = 5.22 \tag{82}$$

$$\left(\frac{Gr}{\mathrm{Re}^2}\right)_R = \frac{\left(T_h - T_c\right)_R L_{hR}}{u_R^{*2}} = \frac{\left(1.054\right) \cdot \left(1.036 \cdot 10^{-2}\right)}{\left(0.089\right)^2} = 1.378 \tag{83}$$

$$\mathrm{P}e_R = \mathrm{Re}_R = u_R^* L_{hR} = \left(0.089\right) \cdot \left(1.036 \cdot 10^{-2}\right) = 9.22 \cdot 10^{-4} \tag{84}$$

$$N_{cR} = \frac{A_{cR} h_{cavR}}{U_{0R} A_{\alpha R}} = \frac{\left(5.342 \cdot 10^{-5}\right) \cdot \left(31.667\right)}{\left(11.304\right) \cdot \left(9.45 \cdot 10^{-4}\right)} = 0.158 \quad (85)$$

$$N_{rR} = \frac{A_{radR} T_{oR}^4}{Q_{0R}} = \frac{\left(5.342 \cdot 10^{-5}\right) \cdot \left(0.927\right)^4}{\left(1.606 \cdot 10^{-4}\right)} = 0.246 \quad (86)$$

$$N_{tR} = \frac{Q_{0R}}{U_{0R} A_{\alpha R} T_{oR}} = \frac{\left(1.606 \cdot 10^{-4}\right)}{\left(11.304\right) \cdot \left(9.45 \cdot 10^{-4}\right) \cdot \left(0.927\right)} = 0.0162 \quad (87)$$

If the non-dimensional *Ra* number similarity group is used instead of the Gr/Re^2 number, then for the air in the RCCS cavity region, it is necessary to respect the condition $Re_m=Re_p=1$, which means:

$$u_m^* = \frac{\mu}{\rho H_m}; u_p^* = \frac{\mu}{\rho H_p} \quad (88)$$

Taking for the air dynamic viscosity $\mu=17.5E\text{-}6\ Pa/s$, and for the air density $\rho=0.877\ Kg/m^3$, the respective reference velocity for air in the experimental facility and plant RCCS cavity are:

$$u_m^* = \frac{\mu}{\rho H_m} = \frac{17.5 \cdot 10^{-6}}{0.877 \cdot 0.29} = 6.881 \cdot 10^{-5}\ m/s; u_p^* = \frac{\mu}{\rho H_p} = \frac{17.5 \cdot 10^{-6}}{0.877 \cdot 28.0} = 7.126 \cdot 10^{-7}\ m/s \quad (89)$$

Using these air reference velocity instead of the values used in Table 11, the ratio of *Ra* number can be calculated:

$$Ra_R = \left(T_h - T_c\right)_R L_{hR}^3 = 1.054 \cdot \left(0.01036\right)^3 = 1.172 \cdot 10^{-6} \quad (90)$$

The change in the ratio of similarity groups with the mockup standpipes volumetric flow is addressed in Table 12 and figures Fig. 12 throughout Fig. 17.

Table 12 – Ratio of similarity groups for Test #1-7

Ratio of similarity groups	Test #1	Test #2	Test #3	Test #4	Test #5	Test #6	Test #7
Ri_R	152.51	3.55E-6	1.22E-6	7.06E-7	4.45E-7	3.61E-7	2.98E-7
St_R	18.08	5.60	5.22	5.03	4.88	4.81	4.75
$(Gr/Re^2)_R$	1.35	1.40	1.38	1.37	1.35	1.35	1.34
Ra_R	1.15E-6	1.20E-6	1.17E-6	1.17E-6	1.15E-6	1.15E-6	1.14E-6
Nc_R	79.221	0.226	0.158	0.132	0.113	0.105	0.099
Nr_R	0.245	0.245	0.245	0.245	0.245	0.245	0.245
Nt_R	8.114	0.023	0.016	0.013	0.012	0.011	0.010

In Fig. 12 is shown the ratio of *Ri* number function of the mockup standpipes annulus average velocity (i.e., standpipes volumetric flow). As it is possible to see from eq. (81):

$$Ri_R = \frac{L_{hR} Q_{0R}}{A_{\alpha R} U_{0R}^3} \tag{81}$$

for very small values of the mockup standpipes volumetric flow (i.e. U_{0R} approaching zero), the ratio of *Ri* number goes rapidly to infinity, since it is inversely proportional to the third power of U_{0R}. The *Ri* number represents the ratio between buoyancy and inertia forces; a good scaling of the plant would require very small volumetric flow in the mockup standpipes. To obtain a Ri_R equal to one, a volumetric flow rate approximately equal to 0.01 gpm would be required. The experiments and CFD simulations were performed with a larger volumetric flow rate (i.e., 0.7, 1.0, 1.2, 1.4, 1.5 and 1.6 gpm). Therefore, both the experiments and the CFD simulations were expected to underestimate the effect due to buoyancy in the standpipes for Test #1-7, which means the experiments were performed under forced circulation standpipes conditions, and the contribute of buoyancy in the momentum equations can be neglected.

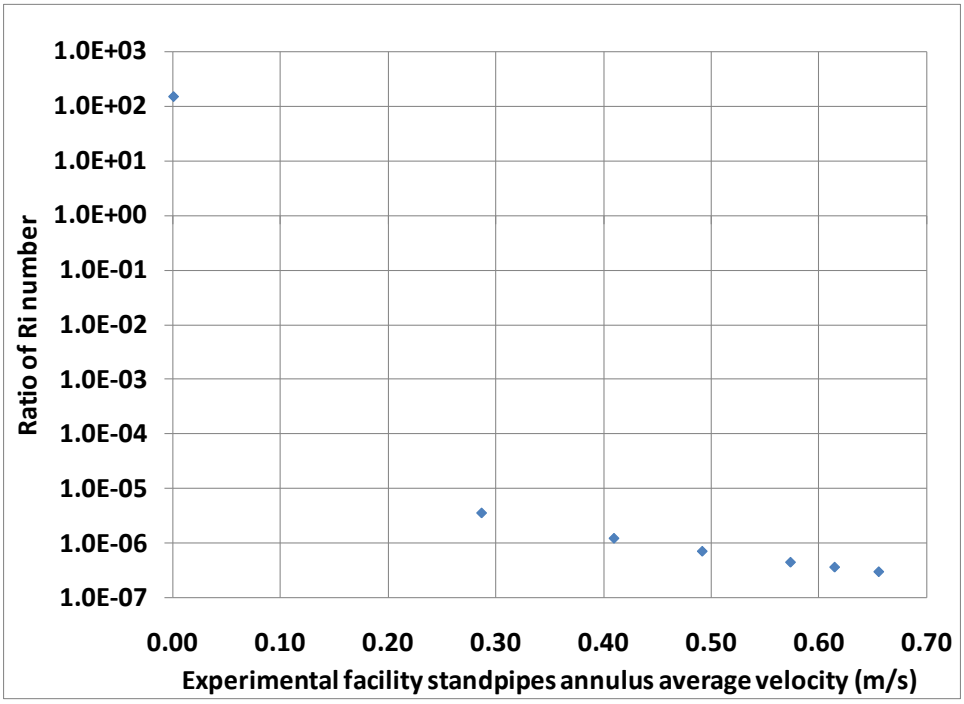

Fig. 12 – Ratio of *Ri* number (Test #1-7)

In Fig. 13 is shown the ratio of the *St* number function of the mockup annulus average velocity. From eq. (82) it is possible to see that also St_R goes to infinity for U_{0R} going to zero, but with a slower rate than *Ri* number:

$$St_{eR} = \frac{P_{eR} U_{0R}^{-0.2} D_R^{-0.2} L_{hR}}{A_{\alpha R}} \tag{82}$$

The *St* number measures the ratio of heat transferred to a fluid respect to the fluid thermal capacity. The ratio of *St* number shows an asymptote for increasing volumetric flow in the mockup standpipes around 4.5. This means that for very large mockup standpipes volumetric flow, St_R will show only slight changes. Since the fluid is the same for the experimental facility and the plant (i.e., water), the ratio of *St* number gives

an estimate of the heat transferred in the standpipes for the mockup with respect to the heat transferred in the standpipes for the real plant. A value of St_R larger than unity addresses the larger heat transfer in the experimental facility standpipes with respect to the plant standpipes. This means that the experimental facility and the CFD simulations will predict an increased heat transfer capability in the standpipes with respect to the real plant conditions. This result is justified comparing the number of standpipes present in the experimental facility (i.e., 5 standpipes) to the 432 standpipes present in the real plant RCCS configuration. In the scaling analysis each standpipe in the experimental facility will have a much larger fraction of heat dissipated with respect to those in the real plant configuration.

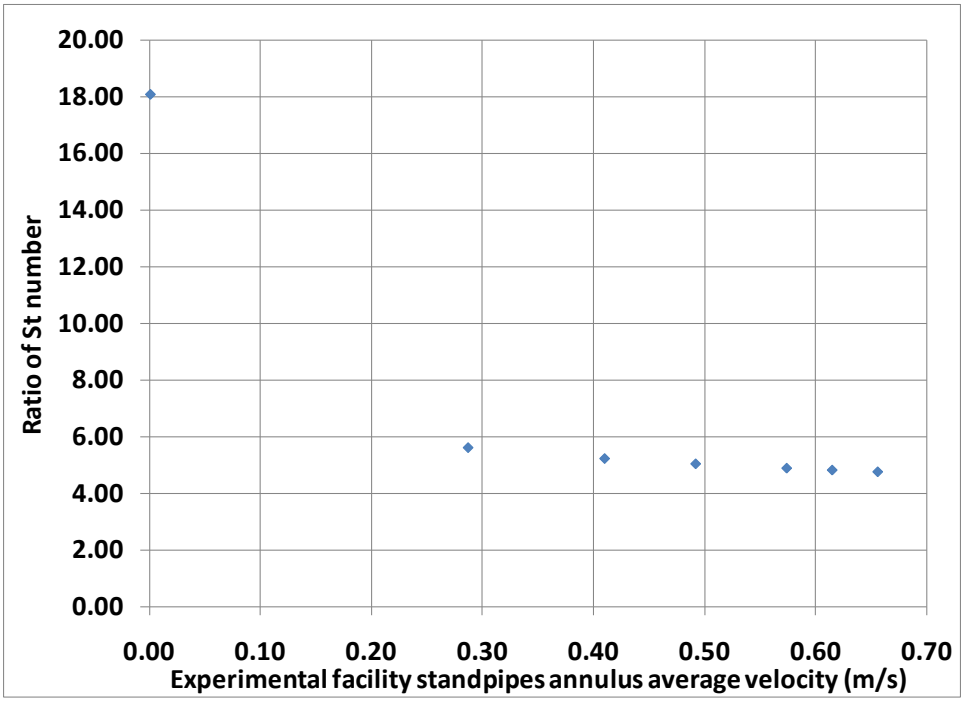

Fig. 13 – Ratio of *St* number (Test #1-7)

In Fig. 14 is shown the ratio of the Gr/Re^2 number. From eq. (83) it is possible to say that Gr/Re^2 depends on the temperature difference between the vessel wall and the standpipes external wall, the RCCS cavity height, and the square of the reference velocity in the cavity region:

$$\left(\frac{Gr}{\mathrm{Re}^2}\right)_R = \frac{\left(T_h - T_c\right)_R L_{hR}}{u_R^{*2}} \tag{83}$$

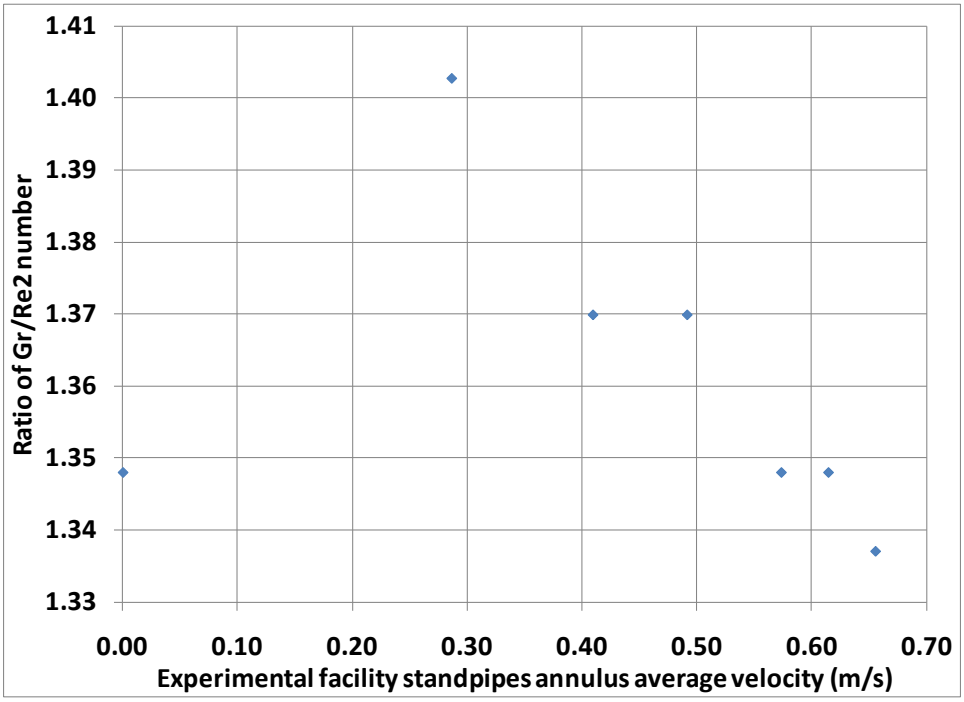

Fig. 14 – Ratio of Gr/Re^2 number (Test #1-7)

The Gr/Re^2 number addresses the importance of buoyancy respect to inertia forces. Taking as reference velocities for the mockup and the real plant the maximum value of the air velocity in the cavity (i.e., the air velocity in the proximity of the RPV upper head wall), the ratio of Gr/Re^2 between the experimental facility and the plant is very close to

one for all experiments and CFD simulations performed. This means that the air conditions in the RCCS mockup are very similar to those of the air in the cavity of the real plant. This implies that the distortions introduced by the scaling are of the same order of magnitude for buoyancy and inertia forces.

From eq. (39), it is possible to determine the value of Gr/Re^2 for the experimental facility considering one of the tests performed. If the case with a volumetric flow of 1 gpm (i.e. Test #3) is considered:

$$\left(\frac{Gr}{\mathrm{Re}^2}\right)_m = \left(\frac{g\beta\left(T_h - T_c\right)H}{u^{*2}}\right)_m = \left(\frac{9.81 \cdot 0.0023 \cdot 250.0 \cdot 0.29}{0.35^2}\right) = 13.35 \tag{91}$$

As addressed before, for $Gr/Re^2 >> 1$, buoyancy forces dominate over inertia forces and a free convection regime is present in the RCCS cavity.

In Fig. 15 is shown the ratio of the *Ra* number function of the standpipes annulus average velocity. The figure shows that, the ratio of the *Ra* number is not sensibly affected by the change in the standpipes volumetric flow. This is due to the fact that, for fixed geometries (i.e., fixed L_{hR}), the change in the standpipes external wall temperature with volumetric flow rate is influenced almost in the same way for the experimental facility and the plant. This means that the ratio of temperature difference between the RPV wall and the standpipes external wall $(T_h\text{-}T_c)_R$ will slightly change with the standpipes volumetric flow. The expression of *Ra* number ratio:

$$Ra_R = \left(T_h - T_c\right)_R L_{hR}^3 \tag{90}$$

Looking at eq. (90) it is easy to understand that the ratio of *Ra* number is slightly influenced by the volumetric flow. Fig. 15 also points out that the *Ra* number for the

experimental facility is about one million times smaller than the *Ra* of the real plant. This discrepancy is due to the different heated length for the mockup and the real plant. The experimental facility/CFD model have a heated length two orders of magnitude smaller than the real plant heated length. The ratio of Ra number is proportional to the third power of the heated length ratio, as eq. (90) shows. The ratio of the temperature difference across the cavity region is of the same order of magnitude for the experimental facility and the real plant (see Table 11). This explains the large difference in the mockup *Ra* number respect to the real plant *Ra* number. Since the *Ra* number can be seen as a ratio between buoyancy forces and viscous forces, the conclusion is that the buoyancy forces which drive the flow in the experimental facility are much smaller than those present in the real plant. This result is in agreement with the physics of the problem represented. A system with a larger vertical heated length will always provide a larger buoyancy force respect to a system with smaller vertical heated length, if the other conditions are similar. The comparison on the *Ra* number between mockup and real plant, though, should be considered in combination with the result obtained for the ratio of Gr/Re^2. For one side, it is true that buoyancy is strongly underestimated in the experimental facility, but the ratio of buoyancy forces/inertia forces (i.e., Gr/Re^2) is correctly scaled and, therefore, the main features of the flow inside the RCCS cavity are not distorted, even if the effect of buoyancy is actually reduced.

Using the definition of the Rayleigh number *Ra* for the model, which is:

$$Ra_m = Gr_m \cdot \mathrm{Pr}_m = \left(\frac{g\rho^2 \beta \left(T_h - T_c\right) H^3}{\mu^2} \right)_m \cdot \left(\frac{\mu c_p}{k} \right)_m = \left(\frac{c_p \rho^2 g \beta \left(T_h - T_c\right) H^3}{\mu k} \right)_m \qquad (92)$$

it is possible to determine the *Ra* number for the conditions specified in the experimental facility. If Test #3 is considered, then:

$$Ra = \frac{c_p \rho^2 g \beta \left(T_h - T_c\right) H^3}{\mu k} = \frac{1003.6 \cdot 1.16^2 \cdot 9.81 \cdot 0.0023 \cdot 250 \cdot 0.29^3}{17.5 \cdot 10^{-6} \cdot 0.027} = 3.93 \cdot 10^8 \qquad (92)$$

For these values of *Ra* number, the RCCS is in free convection regime. This result is in agreement with the conclusion obtained looking at the Gr/Re^2 similarity group.

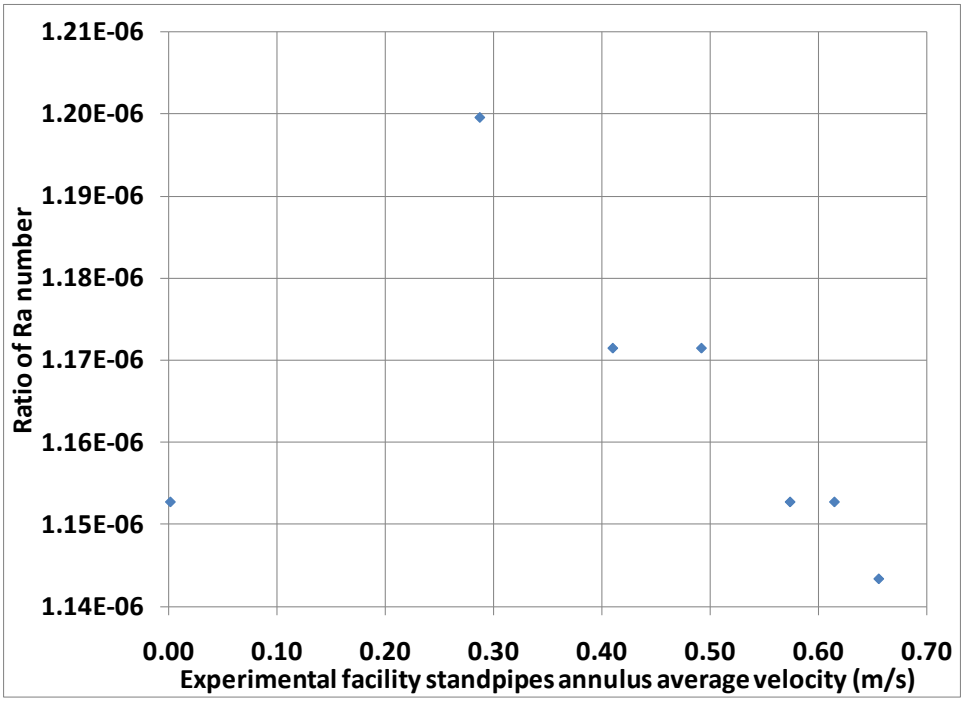

Fig. 15 – Ratio of *Ra* number (Test #1-7)

In Fig. 16 is shown the cavity convective number ratio Nc_R. The cavity convective number *Nc* represents a ratio between the heat transferred from the reactor vessel to the standpipes by convection and the total heat transferred to the standpipes by convection and radiation. If the mockup standpipes volumetric flow decreases to zero, the

standpipes temperature will rapidly increase. This will determine a strong reduction in the fraction of energy transferred from the RPV to the standpipes wall by radiation, and almost all the energy is transferred to the standpipes by convection. This is the reason why the ratio of the convective number increases with the reduction in the experimental facility standpipes volumetric flow. The figure shows that for the volumetric flow rates set in the experiment the scaled model introduces distortions for the convective heat exchange phenomenon.

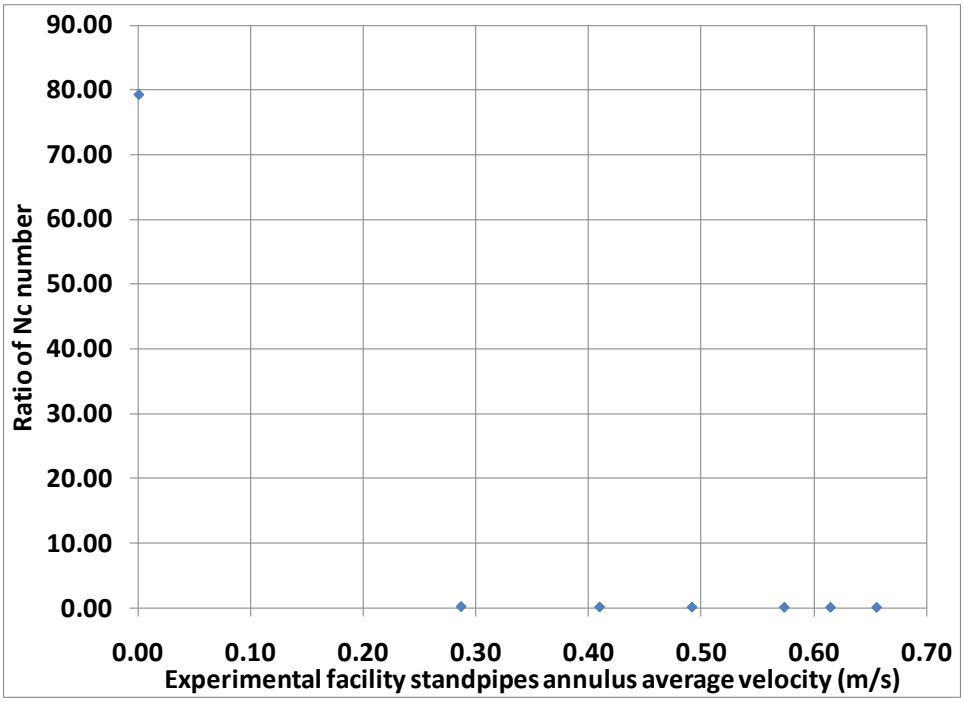

Fig. 16 – Ratio of *Nc* number (Test #1-7)

In Fig. 17 is shown the ratio of radiation number *Nr*. To a first approximation the *Nr* number can be considered as the fraction of the heat transferred from the RPV to the standpipes by radiation and the total heat transferred to the standpipes. This means that

the ratio of convective *Nc* and radiation *Nr* numbers give a good estimate of the energy exchanged in the RCCS by convection and radiation heat transfer phenomena, respectively.

The ratio of the radiation number Nr is independent from the standpipes volumetric flow. This can be easily explained by looking at the definition of the similarity group for the ratio of the radiation number: $N_{rR} = \frac{A_{radR} T_{oR}^4}{Q_{0R}}$. Since for Test #1-7 the power generated inside the RPV region was set constant, the temperature at the standpipes inlet T_o did not change and the A_{radR} is a geometrical factor (i.e., a constant value), the ratio of radiation number *Nr* does not change with the standpipes volumetric flow, as shown in Fig. 17.

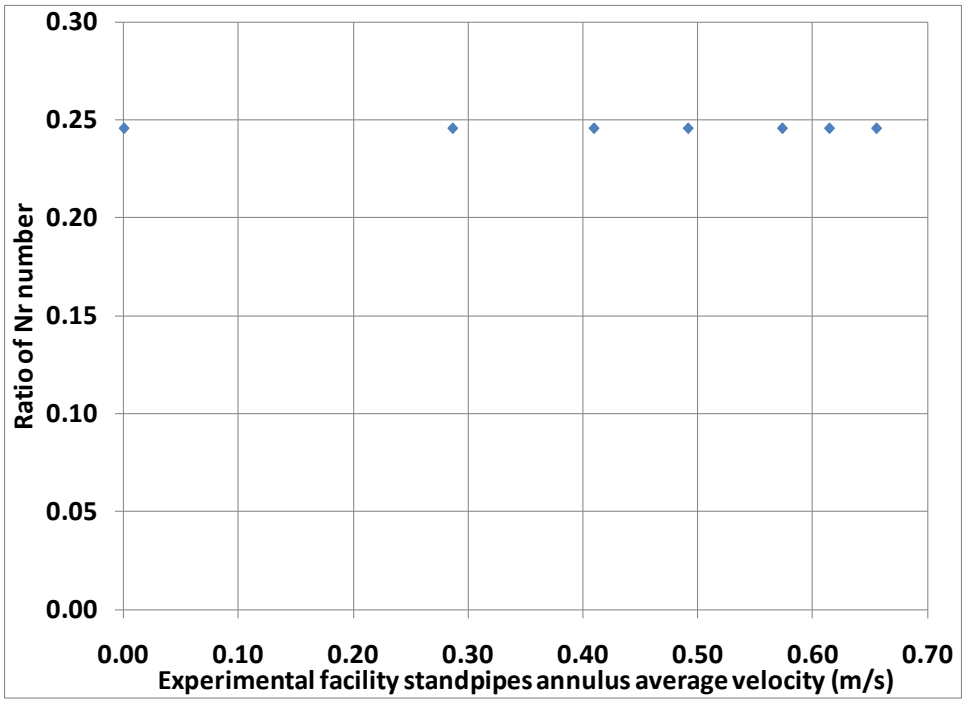

Fig. 17 – Ratio of *Nr* number (Test #1-7)

In Fig. 18 is shown the ratio of Nr and Nc normalized to the sum of Nr+Nc in percentage. The figure addresses how the experimental facility scaled the contribution of radiation and convection to the heat transfer between the RPV and the standpipes walls changing the standpipes volumetric flow with respect to the real plant conditions. For the conditions imposed in the experiments/CFD simulations, the percentage of heat removed from the RPV wall by radiation ranges between the 50% and the 70%, with convection making up for the balance. As will be shown later, the experimental results well agreed with the results from CFD simulations. Also considering that water is cooling the standpipes, lower temperatures are expected for the RPV wall. The fraction of heat removed from the RPV wall varies with the fourth order of the temperature difference between the RPV wall and the standpipes wall. This explains the fact that radiation heat transfer is below the 80% of the total energy removed from the RPV wall.

Fig. 16 and Fig. 17 address the fact that the ratio of the cavity convective number Nc_R and the radiation number Nr_R are not close to one, which means the mockup introduces some distortions with respect to the plant for both convection and radiation phenomena. On the other hand, Fig. 18 shows that the proportions between radiation and convection in the cavity of the experimental facility are still respected. This means that the mockup/CFD model introduce the same amount of distortions for convective and radiation heat exchange phenomena. Considering that the Gr/Re^2 ratio is close to one, it is possible to conclude that the experimental facility/CFD model give a satisfactory description of the main phenomena in the cavity region and of the heat exchange

between the RPV and the standpipes, which means the physics inside the RCCS cavity is properly scaled by the experimental facility and the CFD model.

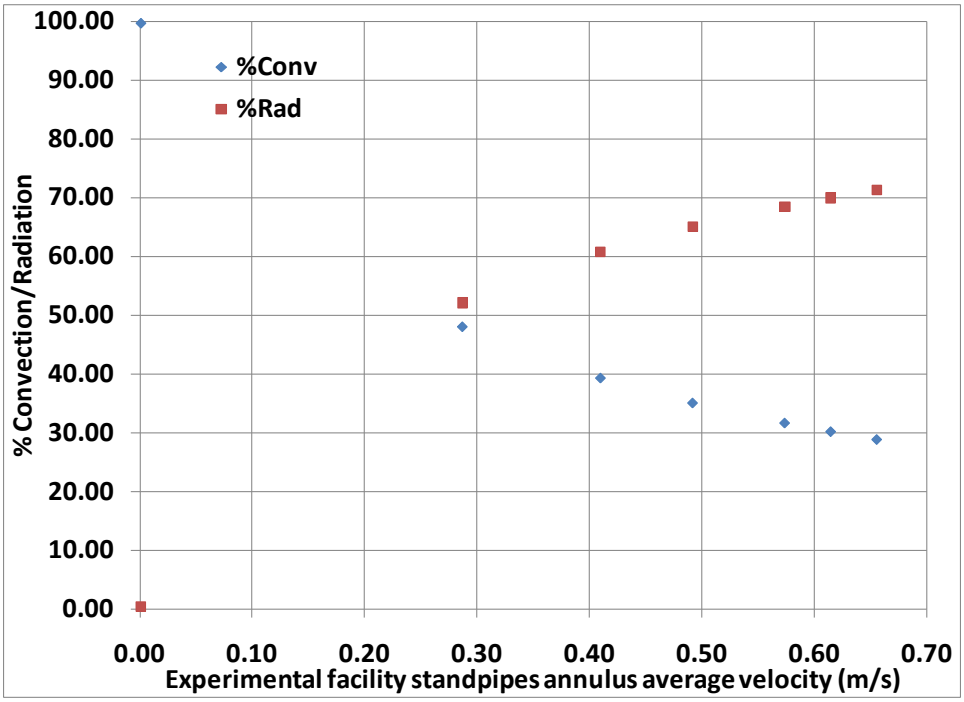

Fig. 18 – Percentage of *Nc* and *Nr* numbers (Test #1-7)

4.3.2 Sensitivity Analysis on the RPV Power Generated for the Water-Cooled RCCS Configuration

CFD sensitivity analyses were performed for the RCCS model, setting as reference parameter the heat source inside the RPV region. In Table 13 are shown the CFD simulations performed for the water-cooled RCCS configuration, setting a constant standpipes mass flow rate, and increasing the RPV power generated (Test #8-10). The objective of these analyses was to simulate the real plant standpipes flow conditions, and to study the behavior of the CFD model for convective and radiation numbers very close

to those of the real plant configuration. A very small standpipes mass flow rate is required to simulate the same flow regime present in the real plant standpipes (i.e., natural circulation). In Table 14 are shown the ratio of similarity groups for Test #8-10.

Table 13 – CFD simulations performed boundary conditions (Test #8-10)

CFD simulation Test #	**RPW power generated (W)**	**Mass Flow Rate (kg/s)**	**U_o (m/s)**
8	27.0	7.2E-04	0.0047
9	50.0	7.2E-04	0.0047
10	175.0	7.2E-04	0.0047

Table 14 – Ratio of similarity groups for Test #8-10

Ratio of similarity groups	**Test #8**	**Test #9**	**Test #10**
Ri_R	0.112	0.208	0.728
St_R	12.76	12.76	12.76
$(Gr/Re^2)_R$	0.335	0.649	1.364
Ra_R	2.87E-7	5.55E-7	1.17E-6
Nc_R	2.916	1.458	0.262
Nr_R	1.690	1.058	0.302
Nt_R	0.190	0.353	1.234

In Fig. 19 is shown the ratio of *Ri* number for Test #8-10. With the low values of standpipes mass flow rate set, the CFD simulations introduce a limited distortion on the scaling of the buoyancy forces respect to the inertia forces, which means that the ratio of *Ri* number is close to unity, as the figure shows.

Table 14 addresses the fact that the CFD model standpipes have an increased heat exchange capacity if scaled to the real plant (i.e., the ratio of *St* number is larger than

one). The ratio of the *St* number is not directly influenced by the change in the RPV power generated (a constant value is obtained for Test #8-10).

From Table 14 is also possible to note that the ratio of Gr/Re^2 is very close e to one, meanwhile the ratio of *Ra* number is much smaller than one. This means that buoyancy over inertia forces are well scaled in the CFD model. On the other hand, buoyancy forces are underestimated in the CFD model with respect to the real plant conditions.

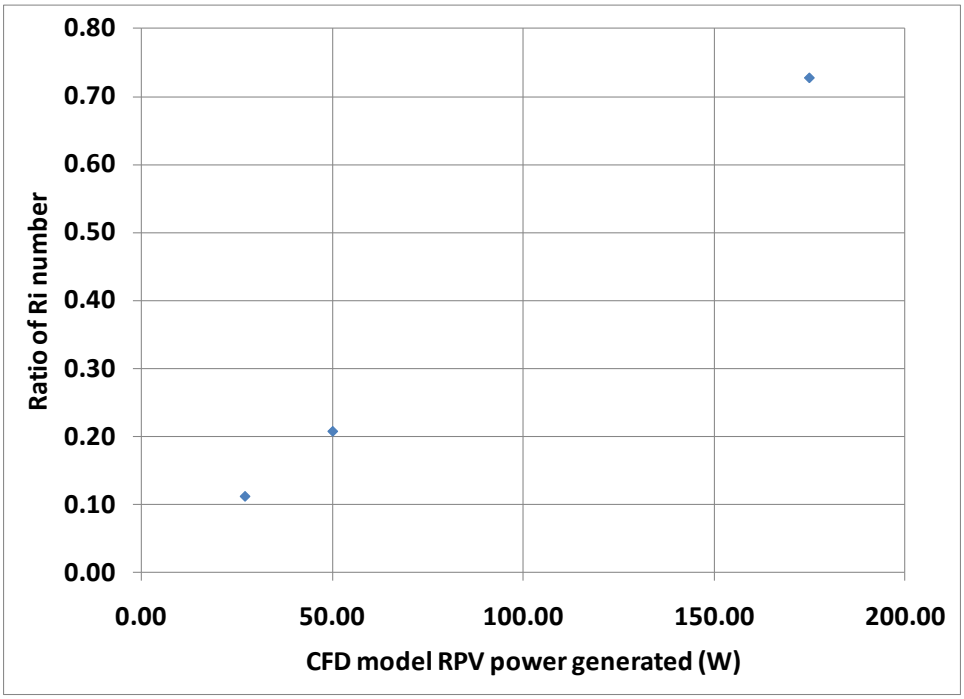

Fig. 19 – Ratio of *Ri* number (Test #8-10)

In Fig. 20 is shown the ratio of *Nc* number, which addresses the distortion introduced by the scaling on the heat transfer by convection in the RCCS cavity region. For the boundary conditions chosen for Test #8 through #10, the ratio of *Nc* number is

close to unity, which means that the scaled facility well addresses the convective heat transfer phenomena in the RCCS cavity region.

In Fig. 21 is shown the ratio of Nr number. The ratio of *Nr* number addresses the distortion introduced by the CFD model respect to the real plant in scaling the radiation heat transfer phenomenon inside the RCCS cavity. Also for the ratio of Nr number, the CFD simulations show there is a small distortion introduced by the scaling on the radiative heat exchange in the RCCS cavity region.

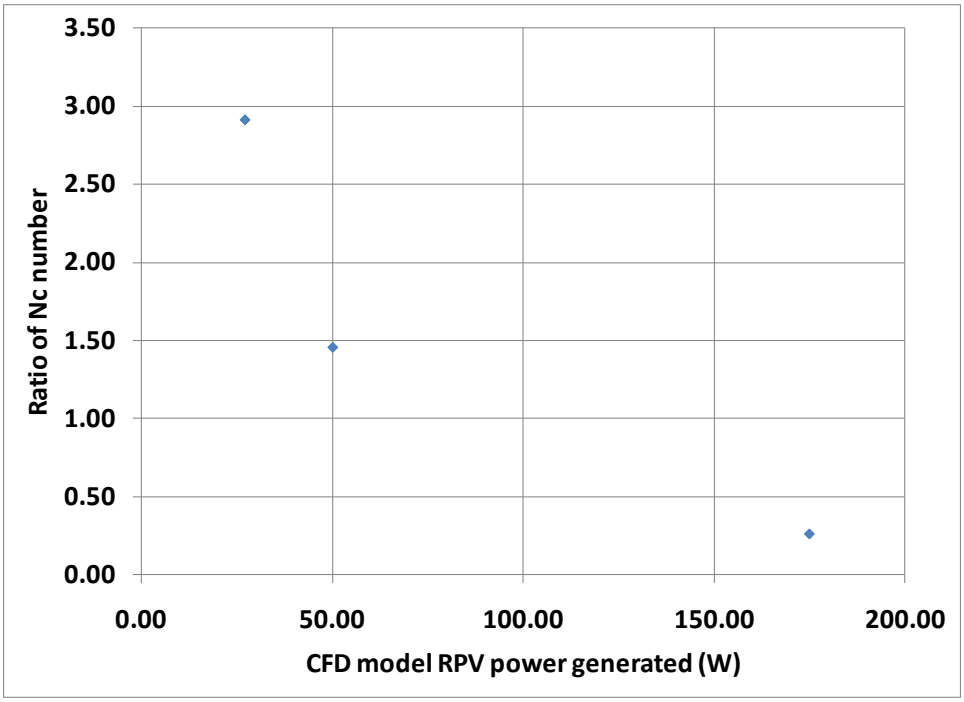

Fig. 20 – Ratio of *Nc* number (Test #8-10)

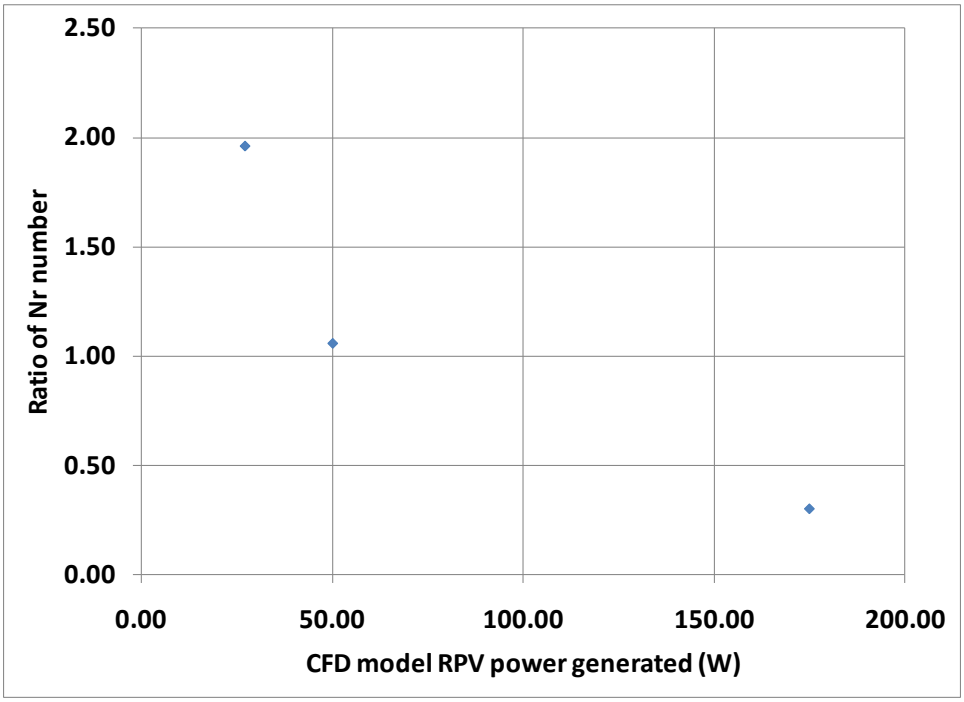

Fig. 21 – Ratio of *Nr* number (Test #8-10)

In Fig. 22 is shown the percentage of convection and radiation phenomena for the CFD simulations with boundary conditions corresponding to Test #8-10. The figure shows that, increasing the RPV power boundary condition from 27 W up to 175 W for the CFD model, the fraction of heat exchange due to radiation progressively increases becoming larger than that due to convection. This behavior of the RCCS can be explained looking at the temperature difference across the RCCS cavity between the RPV wall and the standpipes wall, which increases for larger RPV power generated. This temperature difference determines the amount of energy exchanged in the cavity by radiation. Increasing the power generated inside the RPV region, there will be an increase in the heat exchanged between RPV and standpipes by radiation with respect to the heat exchanged by convection. If for a RPV power of 27 W the percentage is about

61% convection and 39% radiation, with 175 W the percentage is about 43% convection and 57% radiation. This result is in agreement with the experimental facility RCCS behavior and the estimate from other experimental facilities [see IAEA (2000), Capone et al. (2010), Vilim and Feldman (2005)].

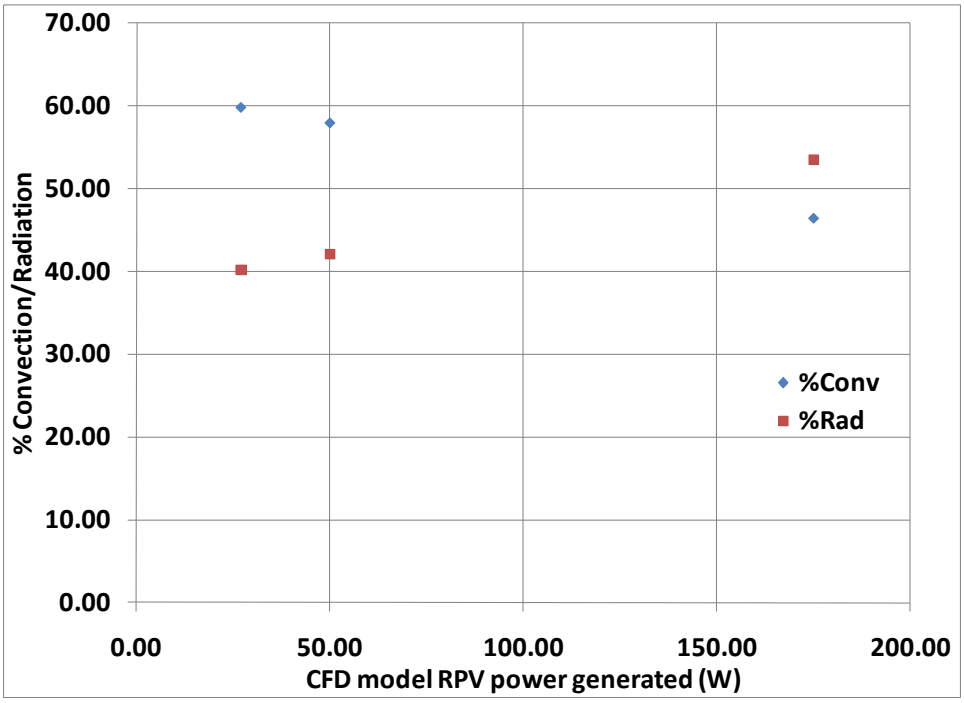

Fig. 22 – Percentage of *Nc* and *Nr* numbers (Test #8-10)

4.3.3 Sensitivity Analysis on the RPV Power Generated for the Air-Cooled RCCS Configuration

CFD analyses were performed with air as cooling fluid in the RCCS standpipes. Based on the benchmark with the experimental data collected at Texas A&M University facility [see Capone et al. (2010), Frisani and Capone et al. (2009), Frisani and Ugaz et al. (2009)], and on the scaling analysis performed for the water-cooled configuration, the

CFD model realized allows to have a preliminary understanding of the RCCS system performances if air was used instead of water in the standpipes. The numerical simulations performed for the RCCS with the air-cooled configuration covered a wide range of operating conditions. This allowed to address what are the main differences between the two configurations, and at the same time to have an estimate if the air-cooled configuration is suitable for maintaining the RCCS concrete wall temperature below design limits. A sensitivity analysis was performed on the power generated inside the RPV region, with the mass flow rate in the standpipes being constant. In Table 15 are shown the boundary conditions set for the CFD simulations on the RPV power generated sensitivity. The scaling analysis was carried out comparing the CFD model developed with the Natural Convection Shutdown Heat Removal Test Facility (NSTF) following the approach of Vilim and Feldman. (2005).

In Table 16 are listed the plant and experimental independent parameters necessary to determine the ratio of the seven independent similarity groups eq. (74) – (80) for the boundary conditions specified in Test #15. In Table 17 are shown the ratio of similarity groups for Test #11-15.

Table 15 – CFD simulations performed boundary conditions (Test #11-15)

CFD simulation Test #	**RPW power generated (W)**	**Mass Flow Rate (kg/s)**	**U_o (m/s)**
11	23.4	0.024	0.156
12	43.16	0.024	0.156
13	65.5	0.024	0.156
14	104.2	0.024	0.156
15	131.0	0.024	0.156

Table 16 – Plant/CFD model independent parameters (air-cooled RCCS)

Scaling independent parameters	Plant	Experiment	Ratio Experiment/Plant
Q_0 (W)	3.3E6	131.0	3.97E-5
L_h (m)	16.0	0.29	0.0181
D_2 (m)	0.0	0.019	//
$D_3 = D_e$ (m)	0.083	0.0236	0.2843
P_e (m)	0.60	0.0741	0.1235
$D_4 = D_{ext}$ (m)	0.089	0.0254	0.2853
n standpipes	292	5	//
A_α (m^2)	3.65	0.0007695	2.108E-4
hydraulic diameter $D=4A_\alpha/P_w$ (m^2)	0.083	0.0046	0.0554
U_0 (m/s)	3.03	0.1562	0.0515
T_c (K)	432.0	390.0	//
T_h (K)	650.0	561.0	//
$T_h - T_c$ (K)	218.0	171.0	0.784
u^* (m/s)	3.0	0.35	0.116
h_{cav} (W/m^2 K)	1.10	0.29	0.2636
A_c (m^2)	2877.95	0.1157	4.02E-5
A_{radm} (m^2)	252.29	0.0578	2.29E-4
T_o (K)	316.0	305.0	0.965
T_r (K)	590.0	388.61	//
$T_r - T_o$ (K)	274.0	83.61	0.305

Table 17 – Ratio of similarity groups for Test #11-15

Ratio of similarity groups	Test #11	Test #12	Test #13	Test #14	Test #15
Ri_R	4.442	8.194	12.436	19.783	24.871
St_R	34.306	34.306	34.306	34.306	34.306
$(Gr/Re^2)_R$	0.356	0.452	0.729	0.910	1.044
Ra_R	1.59E-6	2.02E-6	3.26E-6	4.07E-6	4.67E-6
Nc_R	16.805	8.403	5.042	1.846	0.975
Nr_R	29.186	15.216	10.026	6.302	5.013
Nt_R	0.669	1.246	1.891	3.008	3.782

For the mass flow rate imposed at the standpipes inlet in Test 11-15 the scaling of buoyancy over inertia forces is distorted, since Ra_R is larger than one (see Table 17). This means that, with the imposed mass flow rate in the CFD simulations, buoyancy

effects in the standpipes will be overestimated from the CFD modeling with respect to the real plane standpipes conditions.

Also for the air-cooled RCCS configuration the standpipes geometry determines a larger heat exchange capacity for the scaled model with respect to the prototype. As addressed in Table 17, the ratio of *St* number is larger than one for Test #11-15. This means that the CFD simulations introduce a distortion in scaling the heat exchange at the standpipes wall determining an increased heat removal capability if compared to the real plant standpipes conditions.

The ratio of Gr/Re^2 number shown in Fig. 23 addresses the conditions for the CFD model in the RCCS cavity with respect to the real plant cavity conditions. Also for the air-cooled configuration, and boundary conditions set in Test #11-15, the ratio of Gr/Re^2 is very close to unity, which means the CFD scaled model does not introduce large distortions in simulating the physics inside the RCCS cavity region. Therefore, a good scaling of the buoyancy over inertia phenomena is obtained in the CFD simulations.

On the other hand, the CFD model strongly underestimates the importance of buoyancy in the RCCS cavity region respect to the real plant conditions being the ratio of *Ra* number six orders of magnitude smaller (see Table 17). With a simulated heated length two order of magnitude smaller, and about the same temperature difference across the RCCS cavity walls, buoyancy forces are strongly reduced in the CFD model with respect to the real plant cavity region conditions.

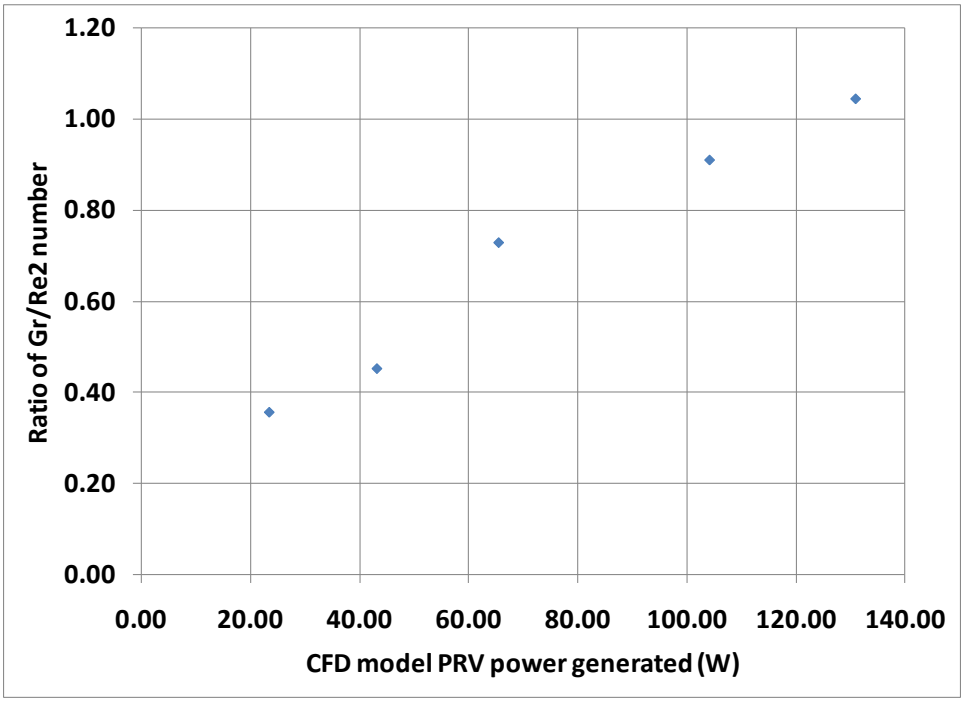

Fig. 23 – Ratio of Gr/Re^2 number (Test #11-15)

From Table 17 it is possible to say that the CFD model introduces some distortions in simulating the heat exchange by radiation and convection inside the RCCS cavity region for the boundary conditions set in Test #11-15. On the other hand, Fig. 24 addresses that also for the air-cooled configuration, the right percentage of convection and radiation heat transfer is predicted by the CFD scaled model. This means that, even if the scaled model introduces some distortions in the calculation of heat exchange by radiation and convection, the two phenomena are properly scaled if considered together in the balance of the heat exchange across the RCCS cavity.

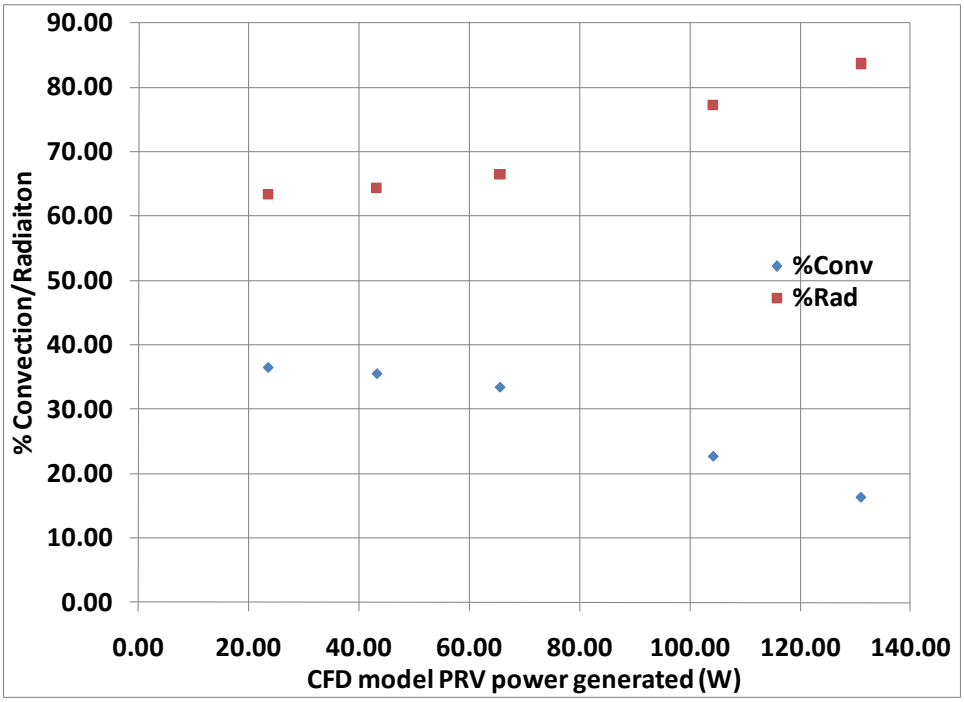

Fig. 24 – Percentage of *Nc* and *Nr* numbers (Test #11-15)

As expected, for the largest value of RPV power boundary condition imposed (i.e., Test #15), the CFD model predicts about 84% of the total power exchanged between the RPV wall and the standpipes due to radiation and the remaining 16% is due to convection, in agreement with the experimental results on the facility and with the values expected for the real plant working conditions [see IAEA (2000), Capone et al. (2010), Vilim and Feldman (2005)].

4.3.4 Sensitivity Analysis on the Standpipes Mass Flow Rate for the Air-Cooled RCCS Configuration

CFD simulations were performed for the RCCS cavity with the air-cooled standpipes configuration using as sensitivity parameter the mass flow rate at the

standpipes inlets. The objective of these analyses was to address different cooling pipes working conditions and flow regimes. In Table 18 are shown the boundary conditions imposed for Test #16-18. In Table 19 is shown the ratio of similarity groups for the boundary conditions imposed in Test #16-18.

Table 18 – CFD simulations performed boundary conditions (Test #16-18)

CFD simulation Test #	**RPW power generated (W)**	**Mass Flow Rate (kg/s)**	**U_o (m/s)**
16	16.7	0.0024	0.0156
17	23.4	0.024	0.156
18	30.0	0.24	1.56

Table 19 – Ratio of similarity groups for Test #16-18

Ratio of similarity groups	**Test #16**	**Test #17**	**Test #18**
Ri_R	3170.65	4.442	0.0057
St_R	54.371	34.306	21.645
$(Gr/Re^2)_R$	0.384	0.356	0.601
Ra_R	1.72E-6	1.59E-6	2.06E-6
Nc_R	16.805	16.805	6.722
Nr_R	40.895	29.186	21.891
Nt_R	4.775	0.669	0.086

In Fig. 25 is shown the ratio of *Ri* number for Test #16-18. Since the ratio of *Ri* number is inversely proportional to the third power of the standpipes fluid velocity ratio U_{0R}, for U_{0R} going to zero, Ri_R diverges. Physically this means that the buoyancy forces become progressively more important than inertia forces in governing the momentum equation. On the other hand, for very large standpipes fluid velocity, the buoyancy forces become negligible with respect to inertia forces, and the ratio of *Ri* number

becomes smaller than unity. Changing the CFD model standpipes annulus average velocity from 0.0156 m/s (i.e., Test #16) up to 1.56 m/s (i.e., Test #18), the ratio of Ri number goes from 3,170 down to 0.0057.

As addressed before, the CFD model based on the experimental facility realized at Texas A&M University [Capone et al. (2010)] overestimates the heat exchange capacity of the standpipes with respect to the real plant for both water-cooled and air-cooled configurations (see Table 19).

Also for Test # 16-18, the CFD model does not introduce large distortions in the scaling of buoyancy forces over inertia forces inside the RCCS cavity region with respect to the real plant conditions (see Table 19). On the other hand, the effect of buoyancy forces is strongly underestimated in the CFD model with respect to the real plant conditions (see ratio of *Ra* number in Table 19).

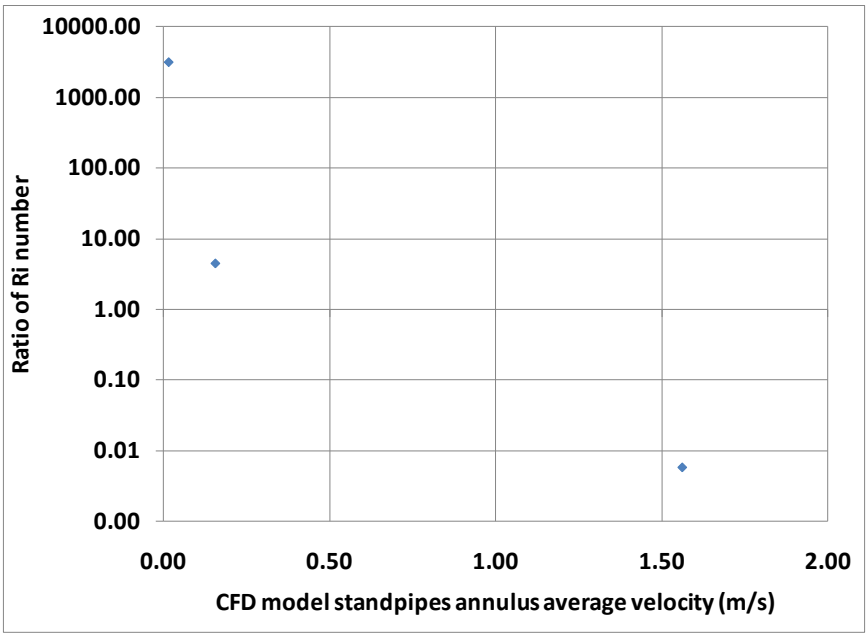

Fig. 25 – Ratio of *Ri* number function (Test #16-18)

The CFD model introduces some distortions in the scaling of convection and radiation heat transfer phenomena inside the RCCS cavity region (see N_{cR} and N_{rR} number in Table 19). In Fig. 26 is shown that even if the CFD model introduces distortions in the representation of the convective and radiation heat transfer phenomena inside the RCCs cavity region, the model can still determine a good repartition of the heat transfer due to the two phenomena. For boundary conditions close to the real plant RCCS cavity working conditions during normal operation and accident (i.e., Test #18), the percentages of radiation and convection heat exchange predicted by the CFD model are in good agreement with experimental results [see IAEA (2000), Capone et al. (2010) and Vilim and Feldman (2005)]. Therefore, the CFD model can address with reasonable accuracy the contribution of convection and radiation heat exchange in the RCCS cavity.

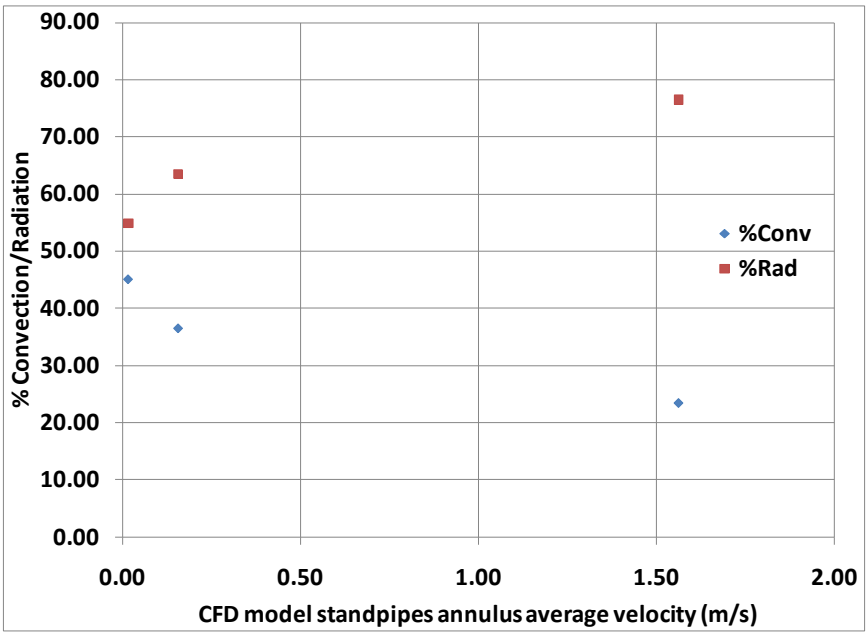

Fig. 26 – Percentage of *Nc* and *Nr* numbers (Test #16-18)

4.4 Conclusions on the Scaling Analysis

The non-dimensional analysis was carried out for two RCCS standpipes configurations: water-cooled and air-cooled, respectively. Experimental analyses were performed at different standpipes mass flow rate values for the water-cooled configuration. CFD analyses were performed at the same boundary conditions set for the experimental analyses, in such a way to benchmark the code respect to the experimental data available. Also CFD simulations for both the water-cooled and the air-cooled RCCS configurations were performed at different standpipes mass flow rate and RPV power generated boundary conditions, in such a way to span a wide range of RCCS operating conditions, and determine the best set of boundary conditions for the experimental facility to have as many as possible ratio of similarity groups close to one, which means to reduce the distortion introduced by the scaling (i.e., simulate the real plant working conditions).

The non-dimensional analysis performed showed that with the boundary conditions chosen for the experimental facility standpipes, buoyancy effects are strongly underestimated with respect to the real plant standpipes working conditions. Since the ratio of Richardson number is much smaller than unity for the experiments performed, buoyancy forces are much smaller than inertial forces for the mockup with respect to the real plant condition. Therefore, in the integral momentum equation, the buoyancy effects are strongly reduced in the experimental facility if compared to those present in the real plant standpipes. The CFD simulations for both the water-cooled and air-cooled RCCS configurations showed that, choosing the appropriate standpipes mass flow rate, it is

possible to have a *Ri* number ratio very close to one, which means the buoyancy forces are correctly modeled in the mockup with respect to the real plant configuration.

The ratio of the Stanton number was larger than one for all experiments performed and for all CFD simulation boundary conditions set. The ratio of *St* number being larger than one addresses the fact that the experimental facility standpipes have an increased heat transfer capability if compared to the standpipes of the real plant. This means that the experimental facility will overestimate the standpipes cooling capability with respect to that of the prototype standpipes.

As addressed before the ratio of Grashof over the square of Reynolds number gives the convection flow regime. Since the ratio of this value (i.e., Gr/Re^2 for the model respect to Gr/Re^2 for the real plant) is close to one for both the experiments and the CFD simulations performed, the experimental facility/CFD model address the air conditions in the cavity region. Also the analysis showed that Gr/Re^2 is larger than unity for both the experimental facility and the real plant, therefore, the air inside the cavity region is in free convection regime.

With an experimental facility heated length two order of magnitude smaller than that of the real plant, the buoyancy forces in the mockup are underestimated with respect to the real plant ones. Since the buoyancy forces are the driving phenomena in free convection regimes, the reference air velocity in the RCCS cavity will be smaller than the one in the RCCS plant. This implies that it is not possible to match the *Re* number ratio.

If an air reference velocity is defined in such a way to obtain a unitary *Re* number for both the mockup and the real plant, the viscous forces become of the same order of magnitude of the inertia forces. Then, the *Ra* number can be used to describe the convective conditions inside the RCCS cavity. The analysis showed that the experimental facility introduces distortion in the effect of buoyancy forces respect to the plant due to the reduced heated length. The ratio of *Ra* number is about 1E-6, which means buoyancy forces in the mockup are strongly underestimated with respect to the buoyancy forces in the real plant. As pointed out before, this result must be considered in combination with the ratio of Gr/Re^2 between the experimental facility and the real plant. The experimental facility introduces the same "amount" of distortions for inertia and buoyancy forces with respect to the plant conditions. This means that the flow regime inside the mockup RCCS cavity is consistent with that inside the real plant RCCS cavity, which is both the real plant and the mockup present a free convection regime. Therefore, the main features of the flow inside the RCCS cavity are not distorted, even if the effect of buoyancy is actually reduced.

The cavity convective number and the cavity radiation number address a very important characteristic of the experimental facility/CFD model. Even if the ratio of the two numbers for the experimental facility and the plant in not unity, the model introduces the same amount of distortions for convection and radiation heat transfer phenomena. This implies that in scaling down from the real plant to the model the two phenomena that control the heat exchange inside the cavity region, the correct repartition to the real plant.

The temperature ratio number addresses the total ΔT across the experimental facility standpipes with respect to the total ΔT for the real plant standpipes. For the water-cooled RCCS configuration the temperature ratio number is close to one when the ratio of *Ri* number is close to one. This implies that when the experimental facility/CFD model address the working condition of the real plane RCCS standpipes from a momentum equation point of view, also a correct scaling of the temperature gradient along standpipes streamwise direction is obtained.

For the air-cooled RCCS configuration the temperature ratio number is close to one when the ratio of *Ri* number is above one, which means buoyancy forces are overestimated respect to inertia forces in the model with respect to the real plant. This behavior is due to the thermal capacity of the mockup standpipes. To have the same temperature gradient of the real plant standpipes a reduced mass flow rate inside the experimental facility standpipes is required.

5. CFD SIMULATIONS OF THE RCCS CAVITY WITH BOTH WATER-COOLED AND AIR-COOLED CONFIGURATIONS

5.1 Introduction to the CFD Simulations Performed

There is great interest in the design of Reactor Cavity Cooling Systems (RCCS). Computational tools play a critical role in the design process, making it important to validate the predicted flow phenomena and demonstrate their reliability in the Very High Temperature Gas-Cooled Reactor (VHTR) scenarios during normal and up-normal conditions. The commercial Computational Fluid Dynamics (CFD) STAR-CCM+/V3.06.006 code was used to simulate heat exchange in the RCCS during the Pressurized Conduction Cooling (PCC) accident [IAEA (2000)]. The analyses performed covered a wide range of RCCS operating conditions. Two different geometries were considered, and two different cooling fluids for the standpipes were analyzed. The effects of imposing various different boundary conditions were also investigated. Also the performance of different turbulence models and near-wall treatments on the predicted heat exchange at the reactor vessel wall and inside the RCCS cavity were tested.

5.2 Description of the CFD Model

Two models were developed to analyze heat exchange in the RCCS. Both models incorporate a 180º section resembling the VHTR RCCS test facility built at Texas A&M University [Capone et al. (2010)]. All the key features of the experimental facility were taken into account. The main difference between the two models was in the geometry of

the standpipes. In the first configuration (referred as geometry I), a once-through geometry was taken into account for the standpipes (see Fig. 27). The cooling fluid enters the bottom of the system, becomes heated and leaves the system from the top. In the second geometry (referred as geometry II), the fluid enters the system from the top through an internal duct in each of the five tubes and moves downwards (see Fig. 28). Once the cooling fluid reaches the bottom of the standpipes, two openings per tube allow the fluid to enter an annulus, and the fluid moves upwards cooling the external pipe walls.

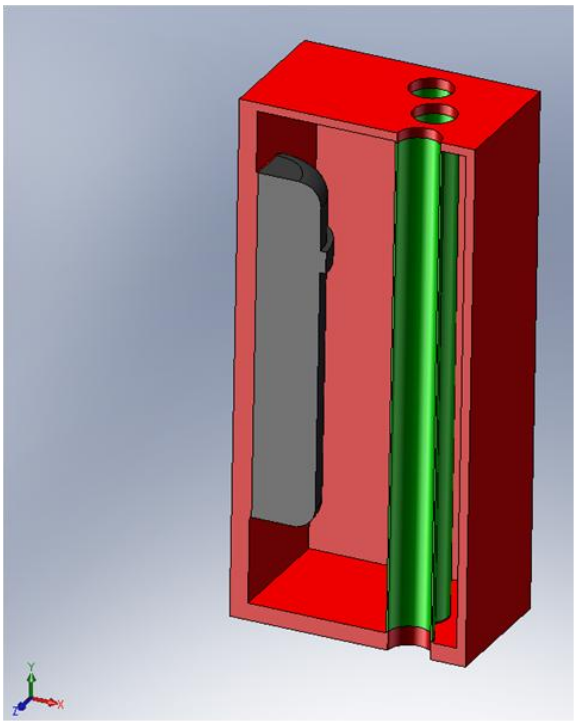

Fig. 27 – Solid works model of geometry I

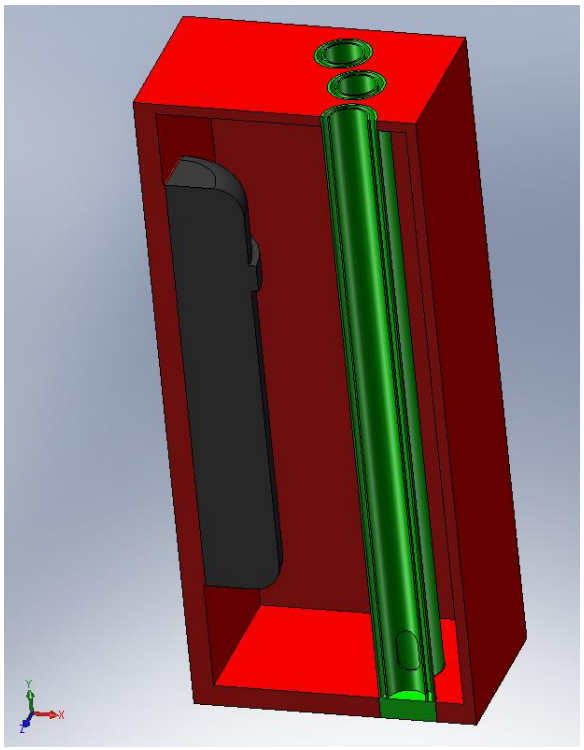

Fig. 28 – Solid works model of geometry II

In Fig. 29 is shown the CFD model of the RCCS, with the Vessel region, the five standpipes, each having a downcomer and riser region, the cavity region and the RCCS external “box” region. In Fig. 30 is shown the RCCS cavity region with the vessel wall interface and the five standpipes external wall interfaces.

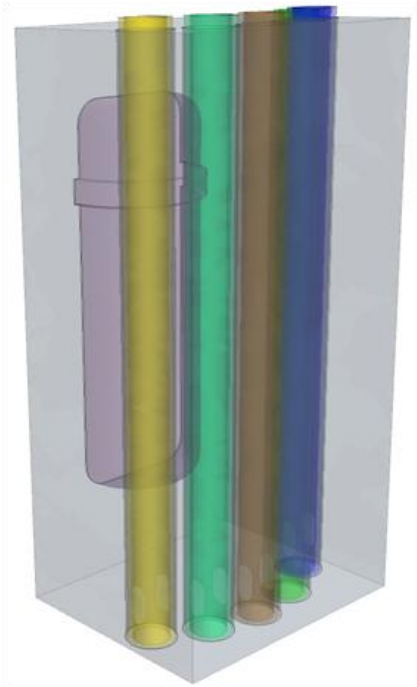

Fig. 29 – CFD model of the RCCS cavity and standpipes regions

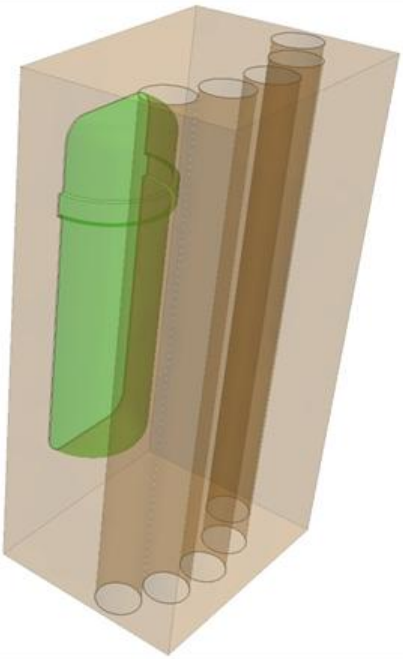

Fig. 30 – CFD model of the RCCS cavity region

For each geometry, two cooling fluids (water and air) were considered to test the capability of maintaining the RCCS concrete wall temperature below design limits. As outlined in Section IV, different boundary conditions were investigated to test the behavior of both water-cooled and air-cooled configurations under a wide range of RCCS working conditions.

The RPV wall temperature distribution for the CFD model was set equal to the one provided by experimental data available [see Capone et al. (2010), Frisani and Capone et al. (2009)] for the water-cooled RCCS configuration (i.e., Test #1-7). The parameter chosen for Test #1-7 was the mass flow rate inside the standpipes as addressed in Table 10. These analyses allowed to have a benchmark of the temperature distribution inside the RCCS cavity region between the values predicted by the CFD computations and the experimental data available. Also performing a sensitivity analysis over the standpipes mass flow rate allowed to describe the behavior of the mockup standpipes and the distortion introduced by the scaled model on the heat exchange at the standpipes wall.

A second set of analyses (Test #8 through #10) was performed for the water-cooled configuration, where the standpipes mass flow rate was kept constant, and a volumetric heat source boundary condition was imposed inside the RPV region. The sensitivity over the heat source boundary condition allowed to address the behavior of the RCCS cavity scaled model for a wide range of different scenarios from normal operation to transient conditions.

CFD simulations of the RCCS air-cooled configurations were performed [Frisani et al. (2009)] with both a fixed temperature profile at the RPV wall and constant standpipes

mass flow rate (Test #11 through #15), and a combination of both constant temperature profile at the RPV wall and different standpipes mass flow rates (Test #16 through #18), to cover a wide range of operating conditions for the air-cooled RCCS design.

Due to the high thermal conductivity of the material used for the mockup vessel (i.e., Cu), setting a constant heat source inside the RPV region is equivalent to an almost constant RPV wall temperature. On the other hand, setting a temperature profile at the RPV wall allows to address the non-uniform heat flux present on the vessel wall, due to the location of the core region and the heat exchange inside the vessel.

A key point in the simulations of the RCCS cavity is the large temperature gradient present across the cavity region. Both experiments and CFD simulations were performed with the RPV wall at a very high temperature, meanwhile the standpipes wall is at a relatively low temperature. For these conditions, it becomes very important to have an accurate estimate of the effect that buoyancy has on the air flow regime inside the RCCS cavity. Since the largest temperature gradients are close to the RPV wall, special care was taken in realizing the mesh close to the RPV wall. To reduce the errors due to mesh discretization, a very fine mesh was realized close to the RPV wall. Five prism layers were generated at the RPV wall, and at the interface between solid and fluid regions were conjugate heat transfer is present. The base size of the first prism layer was set equal to 0.1 mm, which translated in a maximum y^+ smaller than 0.1. This means that the viscous sub-layer was correctly resolved.

Another important issue for a good representation of the buoyancy forces inside the RCCS cavity is linked to the change of air properties with temperature. This aspect was

taken into account using the Sutherland's law for air dynamic viscosity and thermal conductivity. For air inside the RCCS cavity, the ideal gas model was used (i.e., compressibility effects were taken into account).

To test grid independence, five different meshes for the first geometry and six different meshes for the second geometry were considered. Mesh convergence was reached with 4,950,000 cells for geometry I, and 11,202,000 cells for geometry II. Table 20 shows the mesh sensitivity analysis performed on Geometry II.

In Fig. 31 is shown a section of the RCCS cavity mesh for geometry II. From the figure it is possible to distinguish the RCCS concrete walls (i.e., the experimental facility external box made of glass), the RPV region made of copper, the RCCS cavity region (empty region where air recirculates), and the five cooling pipes, simulating the experimental facility standpipes. In Fig. 32 is shown a detail of the central standpipe. The figure shows the external standpipe aluminum wall, the annulus region representing the riser where the cooling fluid flows upwards, the internal pipe also in aluminum, and the internal downcomer region, where the cooling fluid enters the standpipe.

In Fig. 33 is shown a detail of the central standpipe annulus region. As addressed before, for each region where conjugate heat transfer is present, a very fine mesh in proximity of the wall was realized, with five prism layers, and first layer thickness equal to 0.1 mm, in such a way to have a y^+ always smaller than 0.1.

To take into account the heat losses present at the experimental facility external walls with the environment, a convective heat boundary condition was set at the CFD model glass external wall. Sensitivity analyses were performed on the CFD model, in

such a way to have the same amount of energy dissipated by the experimental facility and the CFD simulations in the standpipes and at the external box walls. This allowed the CFD model to give a very close representation of the physics inside the experimental facility.

Table 20 – Geometry II mesh sensitivity analysis

Mesh ID	**Number of total cells**	**Number of prism layers**
I	2,360,842	2
II	3,305,360	2
III	5,191,149	2
IV	7,840,126	5
V	10,775,153	5
VI	11,202,322	5

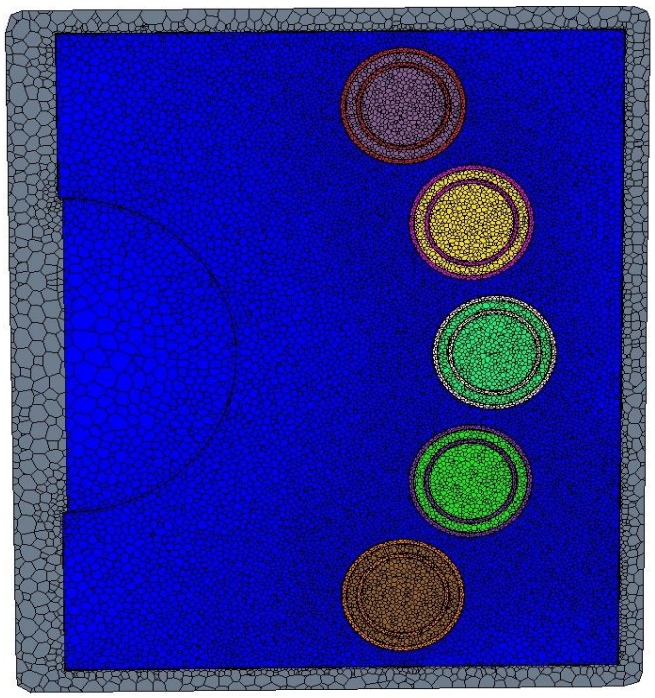

Fig. 31 – Cross section of the RCCS safety system CFD mesh for geometry II

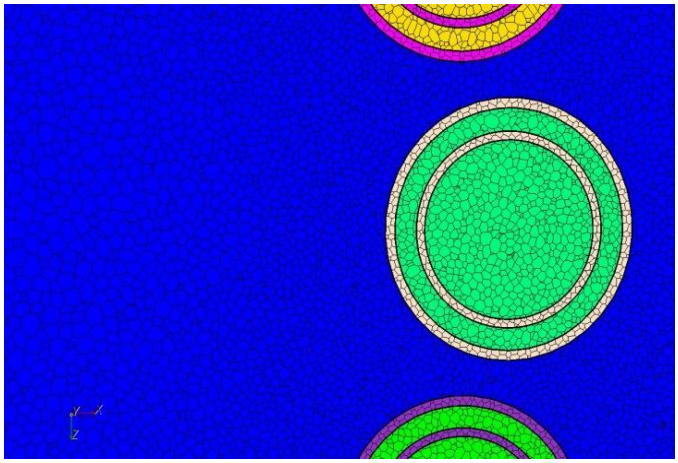

Fig. 32 – Detail of the RCCS central standpipe region for geometry II

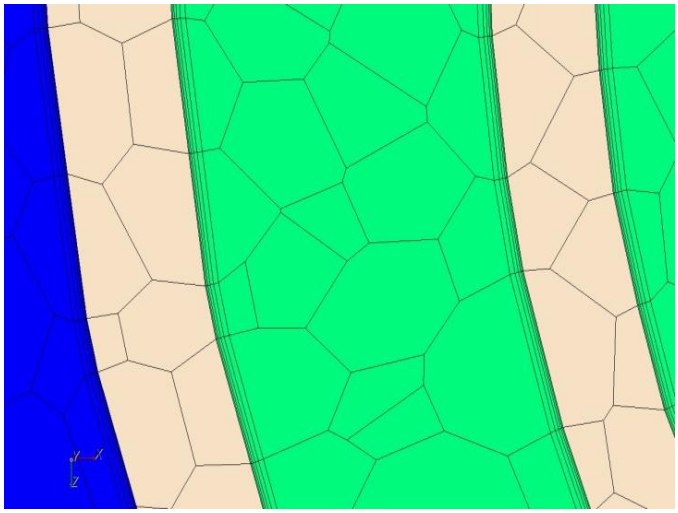

Fig. 33 – Detail of the RCCS central standpipe annulus region for geometry II

5.3 Description of the Turbulence Models Analyzed

To test the effect of turbulence modeling on the RCCS heat exchange, predictions using several different turbulence models and near-wall treatments were evaluated and compared (Table 21). The models considered included the first-moment closure Low-Reynolds Number Standard k-ε model [Lien et al. (1996)] without wall function (*low* y^+)

and a hybrid wall function (*all* y^+) treatment, the Two-Layer Standard *k*-*ε* model [see Jones and Launder (1972), Launder and Sharma (1974)] with a hybrid wall function (*all* y^+) treatment, the Two-Layer Realizable *k*-*ε* model [see Shih et al. (1997) with a hybrid wall function (all y^+) treatment, the Low-Reynolds Number Abe-Kondh-Nagano *k*-*ε* model [see Abe et. al. (1991)] without wall function (*low* y^+) and a hybrid wall function (*all* y^+) treatment, the Standard *k*-*ω* model [see Wilcox(1998)] without wall function (*low* y^+) and a hybrid wall function (*all* y^+) treatment, the SST *k*-*ω* model [see Menter (1994)] without wall function (*low* y^+) and a hybrid wall function (*all* y^+) treatment, the second-moment closure Two-Layer Reynolds Stress Transport (RST) model [see Gibson and Launder (1978), Sarkar and Balakrishnan (1990), Speziale et al. (1991)] with Linear Pressure Strain and a hybrid wall function (*all* y^+) treatment, and the first-moment closure one-equation Spalart-Allmaras [see Spalart and Allmaras (1992)] Two-Layer model without wall function (*low* y^+) and a hybrid wall function (*all* y^+) treatment.

Table 21 – Turbulence models analyzed

Turbulence model	**Near-wall approach**	**Wall treatment**
Standard k-ε	Low Reynolds-Number	low y^+
Standard k-ε	Low Reynolds-Number	all y^+
Standard k-ε	Two-Layer	all y^+
Realizable k-ε	Two-Layer	all y^+
AKN	Low Reynolds-Number	low y^+
AKN	Low Reynolds-Number	all y^+
Standard k-ω	Low Reynolds-Number	low y^+
Standard k-ω	Low Reynolds-Number	all y^+
SST k-ω	Low Reynolds-Number	low y^+
SST k-ω	Low Reynolds-Number	all y^+
RST	Two-Layer	all y^+
Spalart-Allmaras	//	low y^+
Spalart-Allmaras	//	all y^+

In the *low* y^+ wall treatment, it is assumed that the viscous sub-layer is well resolved and thus, wall laws are not needed. This means that the wall shear stress is computed as it would be in a Direct Numerical Simulation (DNS). Due to its nature, the *low* y^+ wall treatment can be used only for Low-Reynolds -Number turbulence models. The Low-Reynolds-Number approach employs a turbulence model that is valid throughout the boundary layer, including the viscous sub-layer. Damping functions are applied to the coefficients of the Low-Reynolds-Number models. These functions modulate the coefficients as functions of a turbulence Reynolds number, also incorporating the wall distance. For meshes sufficiently fine to resolve the viscous sub-layer, it is not necessary to model the wall boundary conditions. Therefore, in the *low-*y^+ wall treatments the viscous sub-layer is properly resolved all the way to the wall cell. There is no need for *wall laws*.

The all y^+ wall treatment is a hybrid formulation in which no assumption is made on how well the viscous sub-layer is resolved. A blended wall function is used to estimate shear stress close to the wall. This means that the *all* y^+ wall treatment attempts to emulate the *high* y^+ wall treatment for coarse meshes and the *low* y^+ wall treatment for fine meshes. Therefore, the result is close to the *low* y^+ wall treatment if the mesh is fine enough close to the wall ($y^+ < 1$). On the other hand, if the mesh is coarse enough ($y^+ > 30$), the wall law is equivalent to a logarithmic profile (i.e., *high* y^+ wall treatment). The *all* y^+ wall treatment should produce reasonable answers also for meshes of intermediate resolution, which means when the wall-cell centroid falls within the buffer region of the

boundary layer. The *all* y^+ wall treatments require the profile of the mean flow quantities to be specified in the near-wall region of turbulent boundary layers. These profiles are termed *wall laws*. To take into account the effect of the buffer layer, blended wall laws [see Kader (1981), Reichardt (1951)] are used.

An alternative to the Low-Reynolds-Number approach is to use the Two-Layer model (see Rodi (1991)]. In this approach, the computation is divided in two layers. In the layer adjacent to the wall, the turbulent dissipation rate ε and the turbulent viscosity μ_t are specified as function of wall distance. The values of ε specified in the near-wall layer are blended smoothly with the values computed from solving the transport equation far from the wall. The equation for the turbulent kinetic energy is resolved in the entire flow. This formulation works with either the Low-Reynolds-Number meshes (i.e., $y+ < 1$) or wall-function type meshes (i.e., $y+ > 30$). Two types of two-layer formulations are available in STAR-CCM+/3.06.06: the Shear Driven formulation of Wolfstein (1969), appropriate for flows that are not dominated by buoyancy forces, and the Buoyancy Driven formulation of Xu et al. (1998), to be used for flows that are dominated by buoyancy forces. The turbulence models applied in the RCCS cavity region used the Buoyancy Driven two-layer model due to the presence of strong temperature gradients which implies relevant buoyancy effects. Depending on the boundary conditions imposed in the standpipes, i.e. natural circulation due to buoyancy or forced circulation, the Buoyancy Driven or the Shear Driven two-layer model were applied, respectively.

For the Reynolds Stress Transport turbulence model applied, a linear pressure-strain model of Sarkar and Balakrishnan (1990) was used, which splits the pressure-strain term in a slow (return-to-isotropy) term, a rapid term, and a wall-reflection term. A Two-Layer formulation for resolving the viscous sub-layer was applied.

The segregated flow model for solving the momentum equations and the continuity equation for pressure was used for all simulations performed. For this solver the equations for the components of velocity and pressure are solved in an uncoupled manner. The linkage between the momentum and continuity equations is achieved with a predictor-corrector approach. The second-order upwind scheme was used for the convection term in all simulations performed.

6. RESULTS AND DISCUSSION

In the following pages will be presented the results relative to the CFD simulations for the RCCS water-cooled and air-cooled configurations. Comparisons with the experimental data available and between the different turbulence models used will be shown, and a discussion of the main physical phenomena present in the RCCS cavity and standpipes regions will be addressed.

6.1 Analysis of the RCCS Water-Cooled Configuration (Test #3)

Test #3 was performed setting a temperature profile for the CFD model RPV wall boundary condition, provided from a best fit of the experimental data available for the temperature distribution at the mockup vessel wall. The other boundary conditions are shown in Table 10. In Fig. 34 and Fig. 35 is shown the imposed PRV wall temperature distribution.

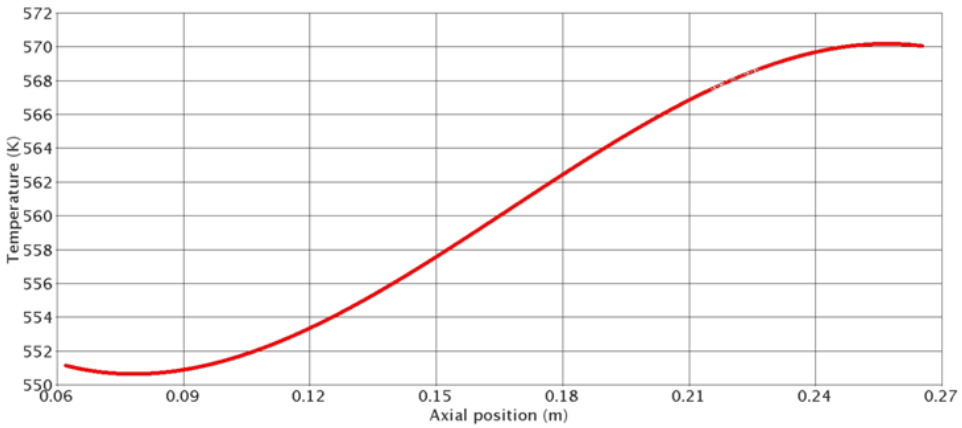

Fig. 34 – Imposed RPV wall temperature distribution (a) – Test #3

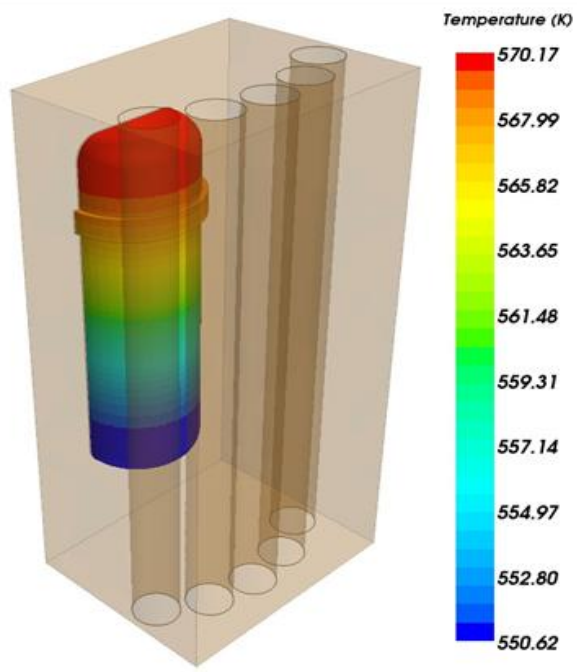

Fig. 35 – Imposed RPV wall temperature distribution (b) – Test #3

In Fig. 36 through Fig. 39 are shown the experimental results for the axial temperature distribution inside the RCCS cavity at 0.25 mm (line probe 1), 25.4 mm (line probe 2), 38.1 mm (line probe 3) and 50.8 mm (line probe 4) from the reactor vessel wall, respectively. The experimental data were collected taking the measurements of the air temperature in the RCCS cavity region through a rack plane (see Section 3.4). The figures also show the temperature distribution determined by the STRAR-CCM+ code for the different turbulence models analyzed. The figures show that the computational results are close to the experimental data, especially in the upper part of the RCCS cavity region. Some differences between the experimental data and the numerical results were present in the lower part of the RCCS cavity region. These discrepancies between computational and experimental results were due to the bottom

part of the RCCS cavity wall. In the experimental facility the bottom cavity wall was partially made of aluminum, meanwhile glass was assumed for the CFD model. The aluminum in the mockup determined a higher temperature for the lower part of the RCCS cavity due to radiation heat exchange between the RPV wall and the external box (i.e., back radiation from the bottom wall in the cavity region). This can be seen if the first temperature measurement at the bottom of the RCCS cavity is taken into account. Looking at Fig. 36, there is a difference of almost 40 K between the first and the second experimental measurements at the bottom of the RCCS cavity. This is due to the higher temperature of the bottom wall respect to the air in the RCCS cavity region. This behavior is not shown in the CFD simulations, since the bottom wall is at a lower temperature than the air in the RCCS cavity region. Due to this discrepancy between the experimental facility and the CFD model, the air temperature in the lower part of mockup cavity region is higher than the air temperature in the CFD model cavity region. Notwithstanding the differences between the CFD numerical simulations and the experimental data, it is possible to say that the numerical results show a good qualitative agreement with the experimental data.

Considering the sensitivity analysis over the different turbulence models analyzed, the figures show that all turbulence models can qualitatively predict the right temperature distribution inside the RCCS cavity, with relatively small differences among the models analyzed. In general it is possible to say that the k-ε models performed better than the k-ω models, if compared to both the experimental data and the RST results. Between the k-ε turbulence models, the ones using the Two-Layer approach performed

better than the turbulence models using the Low-Reynolds Number approach. For the treatment of the wall region, the *all* y^+ methodology resulted in a better convergence if compared to the *low* y^+ approach.

Among the k-ε models analyzed, the Realizable k-ε turbulence model performed better than the Standard and the Abe-Kondoh-Nagano k-ε models.

In Fig. 36 is possible to note the sharp air temperature increase in proximity of the RPV bottom head (i.e., around 0.06 m). The figure also shows the increase of air temperature along the RPV wall (i.e., buoyancy forces are driving the air upwards), and the sharp increase in the air temperature close to the RPV flange (i.e., about 0.21 m from the cavity bottom wall). The concave shape of the temperature distribution in the upper part of the cavity is due to the presence of the main recirculation region which moves colder air towards the upper part of the cavity region.

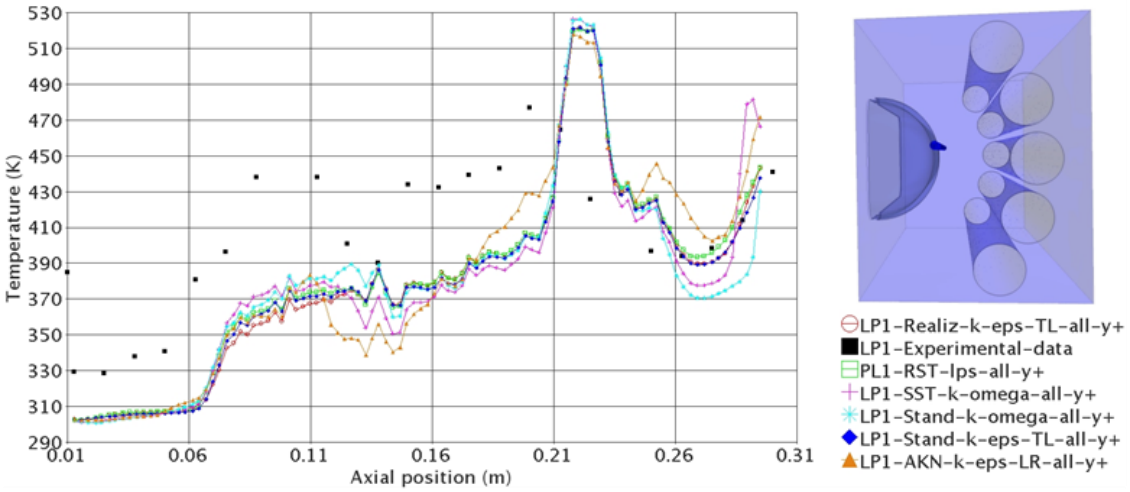

Fig. 36 – Cavity region axial temperature distribution (line probe 1) – Test #3

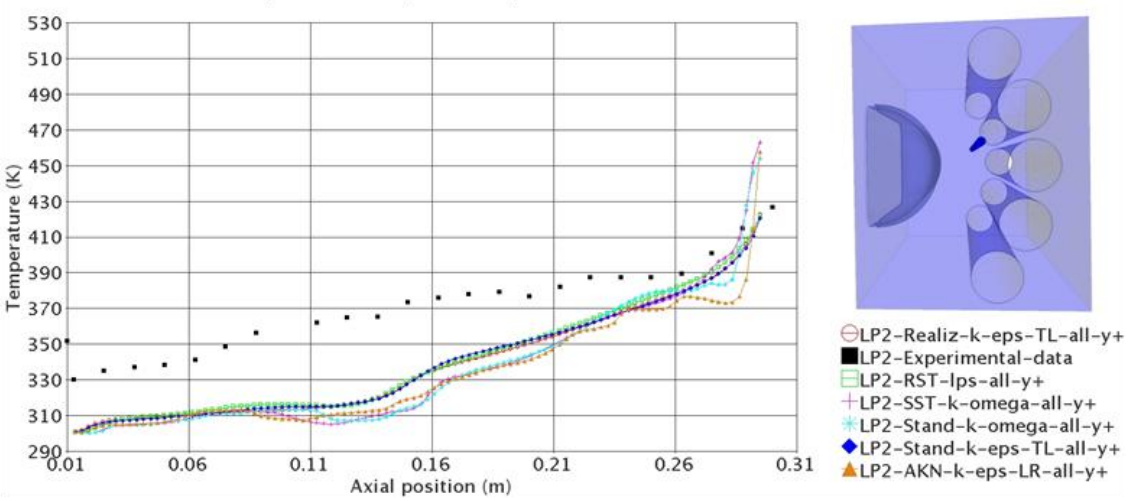

Fig. 37 – Cavity region axial temperature distribution (line probe 2) – Test #3

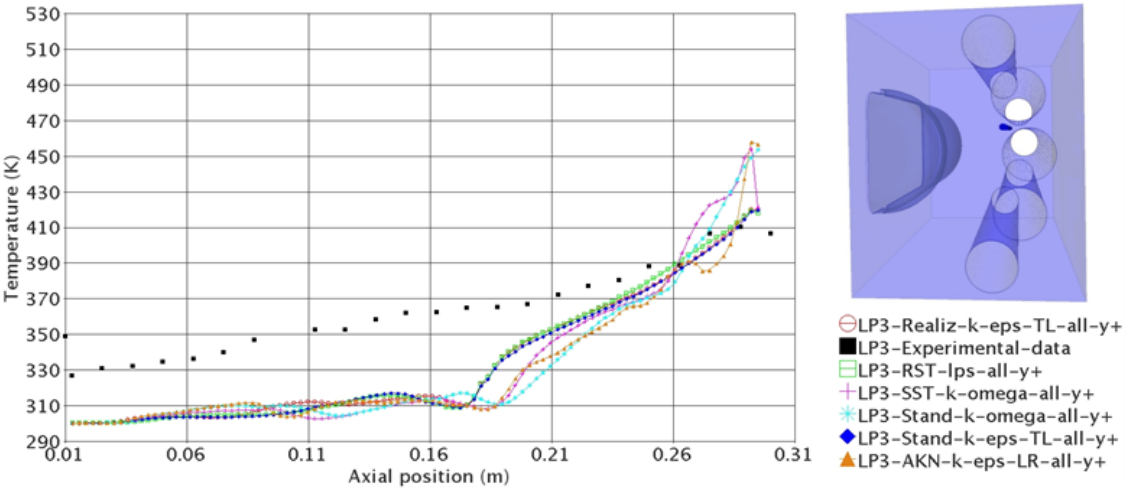

Fig. 38 – Cavity region axial temperature distribution (line probe 3) – Test #3

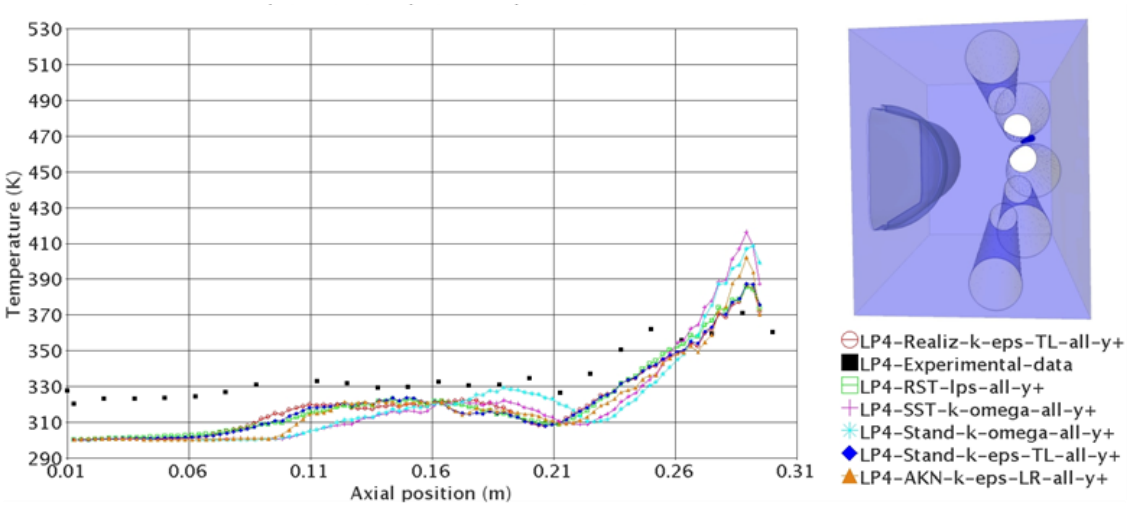

Fig. 39 – Cavity region axial temperature distribution (line probe 4) – Test #3

In Fig. 40 is shown the axial temperature distribution at the cavity region back wall rack plane location (line probe 5) predicted by the different turbulence models analyzed. No experimental data were available for this location. The figure shows that with the water-cooled configuration, the maximum wall temperature of the RCCS cavity region would not exceed 360 K (87 °C). Considering that below 100 °C, the loss in concrete material properties (e.g., the strain) is less than 10% [see Kassir et al. (1996)], this means that the water-shield configuration can be considered for further analysis in shielding the RCCS concrete walls from the RPV high temperature wall.

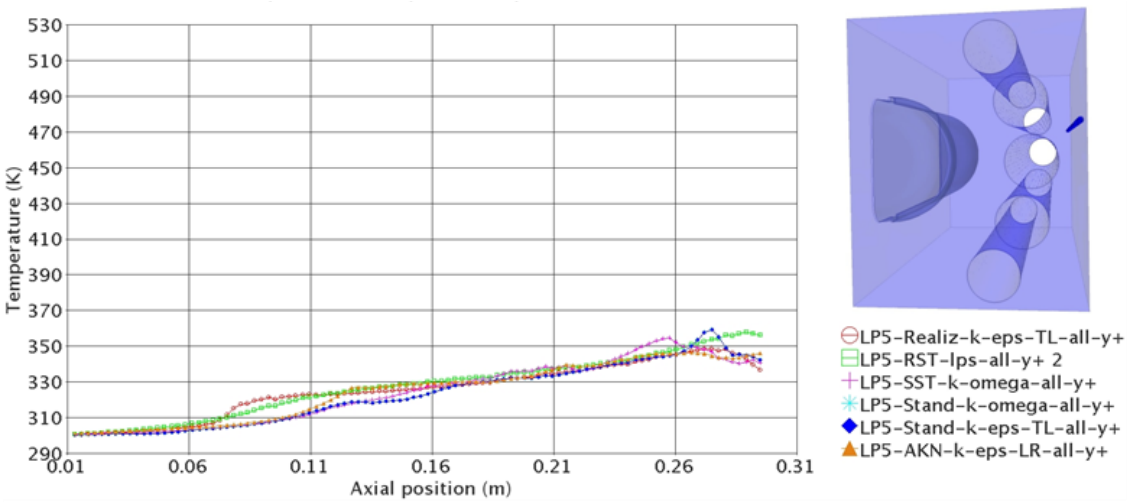

Fig. 40 – Cavity region axial temperature distribution (line probe 5) – Test #3

In the following figures the results relative to the simulation performed using the Realizable k-ε turbulence model with Two-Layer and *all* y^+ wall treatment will be discussed. In Fig. 41 in shown the calculated temperature distribution at the standpipes external wall for Test #3. The numerical results show that with the water-cooled RCCS configuration the standpipes temperature is much lower than the RPV wall temperature (see Fig. 35). As the analysis of non-dimensional groups showed, this behavior is due to the large mass flow rate imposed in the experimental facility standpipes, which gives a forced circulation flow regime, with a ratio of *Ri* number much smaller than one. In fact, the experiments and the CFD simulation for Test #3 were performed to a larger mass flow rate if scaled to the real plant standpipes conditions. This means that a very low standpipes wall temperature, and very low temperature gradient across the tube axial direction is obtained.

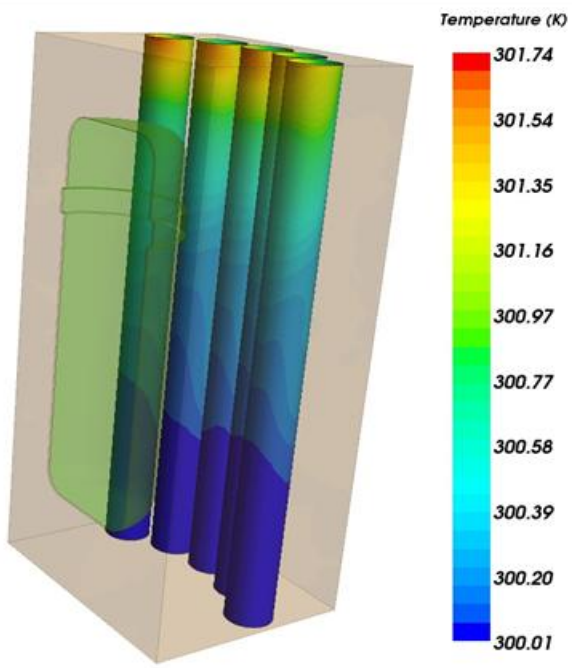

Fig. 41 – Temperature distribution at the standpipes wall – Test #3

In Fig. 42 through Fig. 45 is shown the velocity vector distribution inside the RCCS cavity region plotted at the rack plane location. In Fig. 42 is shown the velocity vector distribution at the bottom of the RCCS cavity region. The figure shows that the air below the RPV wall is almost stagnant. This is due to the higher temperature of the PRV lower head with respect to the external box lower wall. This means that the air closer to the external box bottom wall will be at a lower temperature (i.e., higher density) than the air closer to the RPV bottom head, as can be seen from Fig. 36 through Fig. 40. Under these conditions, stratification is present, as was expected. Approaching the RPV wall, the air temperature strongly increases (i.e., the air density strongly decreases) and buoyancy effects become the driving phenomena. The air close to the RPV wall is accelerated as can be seen in Fig. 43, Fig. 44, and Fig. 45. At the upper head of the RPV wall a

separation region is present (see Fig. 45), with air detaching from the vessel wall and moving towards the cavity upper wall. At this point the air at very high temperature (i.e., very low density) is directed downwards along the cold standpipes wall. Air exchanges heat with the standpipes wall; the air temperature decreases and the air density increases. At the bottom of the cavity the air reaches the lower temperature (i.e., higher density), and is redirected towards the hot RPV wall. This is the largest recirculation region present in the RCCS cavity gap between the RPV wall and the standpipes wall where free convection develops. In the upper part of the RCCS cavity it is also possible to see another recirculation region (see Fig. 45) between the RPV upper head and the RCCS cavity top wall.

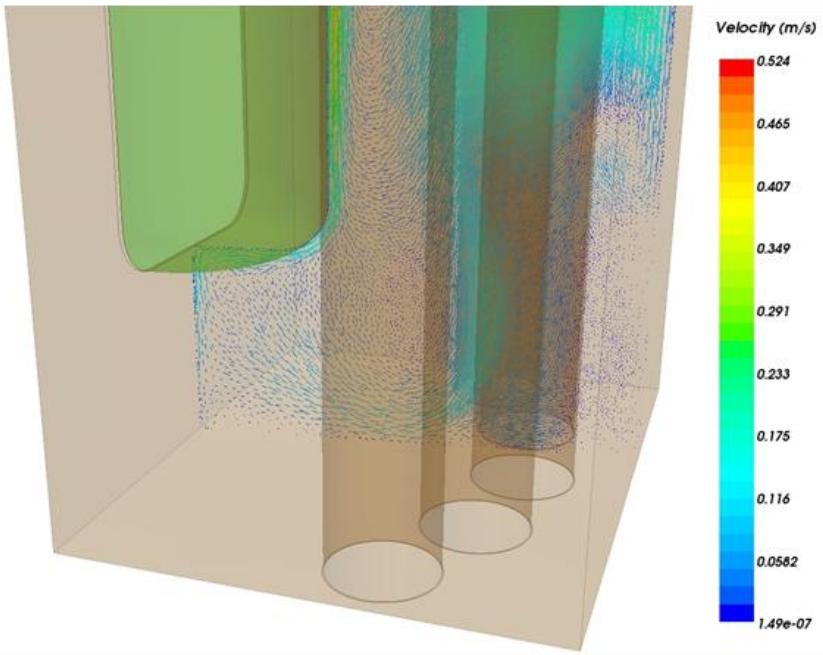

Fig. 42 – Velocity vector in the cavity region bottom part – Test #3

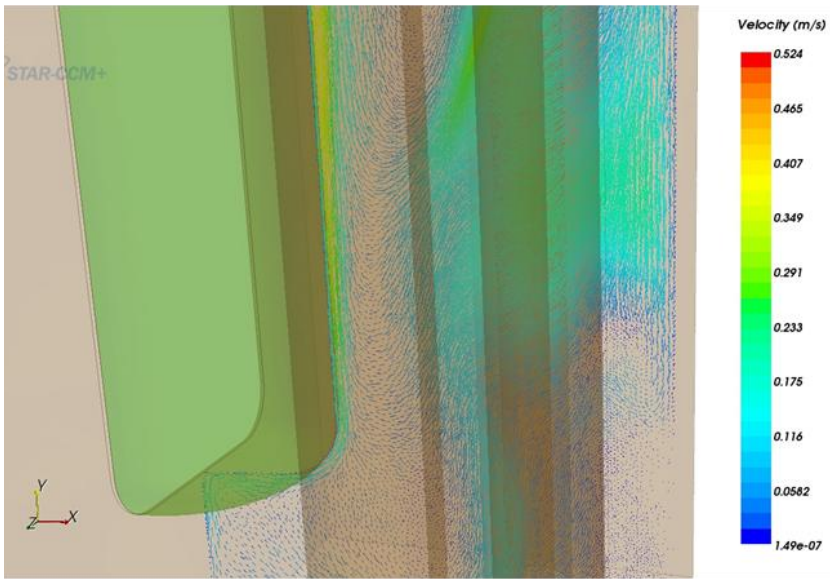

Fig. 43 – Velocity vector in the cavity region lower RPV head – Test #3

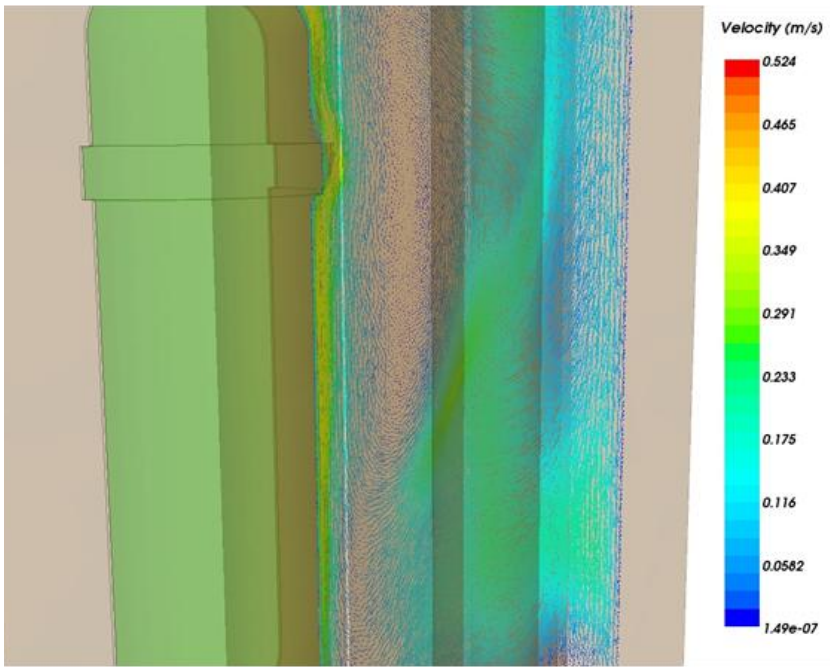

Fig. 44 – Velocity vector in the cavity region upper RPV head – Test #3

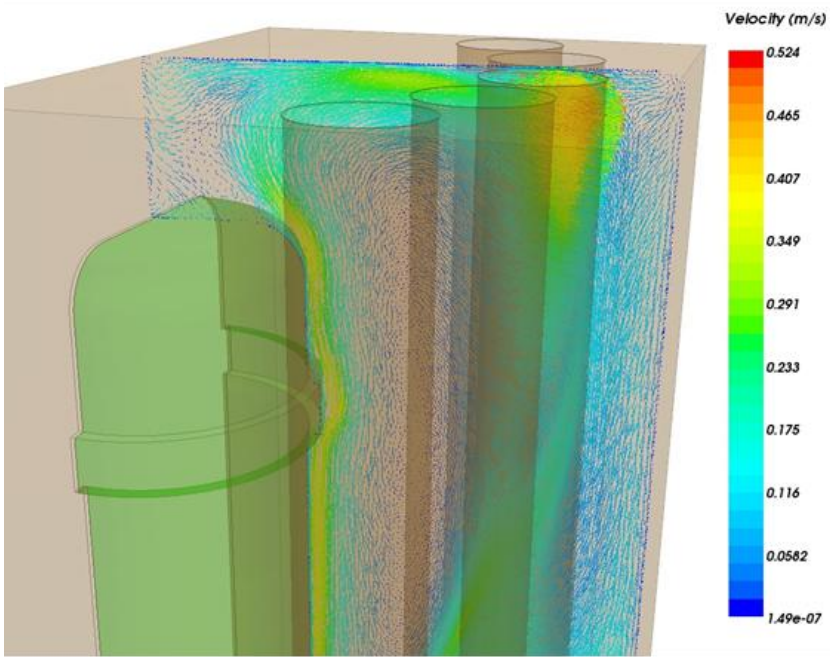

Fig. 45 – Velocity vector in the cavity region upper part – Test #3

In Fig. 46, Fig. 47 and Fig. 48 are shown the air temperature distribution in the lower, middle, and upper part of the RCCS cavity region rack plane location, respectively. The figures show the stratification region in the lower part of the cavity region below the RPV lower head, the temperature gradient in the gap between the RPV wall and the standpipes wall, and the recirculation region in the upper part of the cavity region, as previously described.

In Fig. 49 is shown the temperature isosurface in the RCCS cavity region. The figure shows that the air is heated close to the RPV wall and moves upwards towards the cavity top wall. Then the air is redirected towards the standpipes cold walls. Exchanging heat with the standpipes wall, the air in the cavity becomes heavier and start to descend along the standpipes wall forming the main recirculation path.

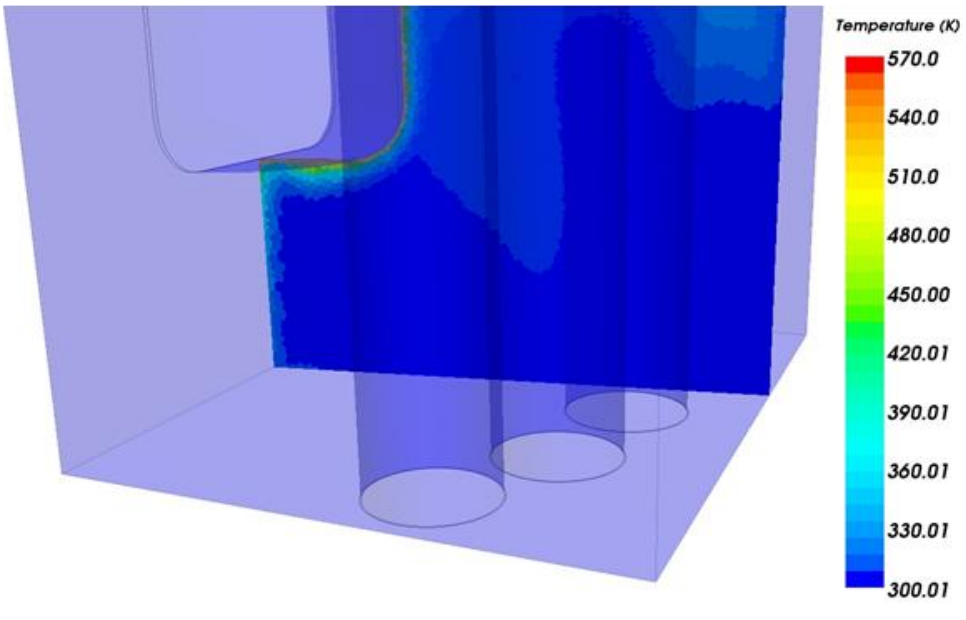

Fig. 46 – Temperature distribution in the cavity bottom part – Test #3

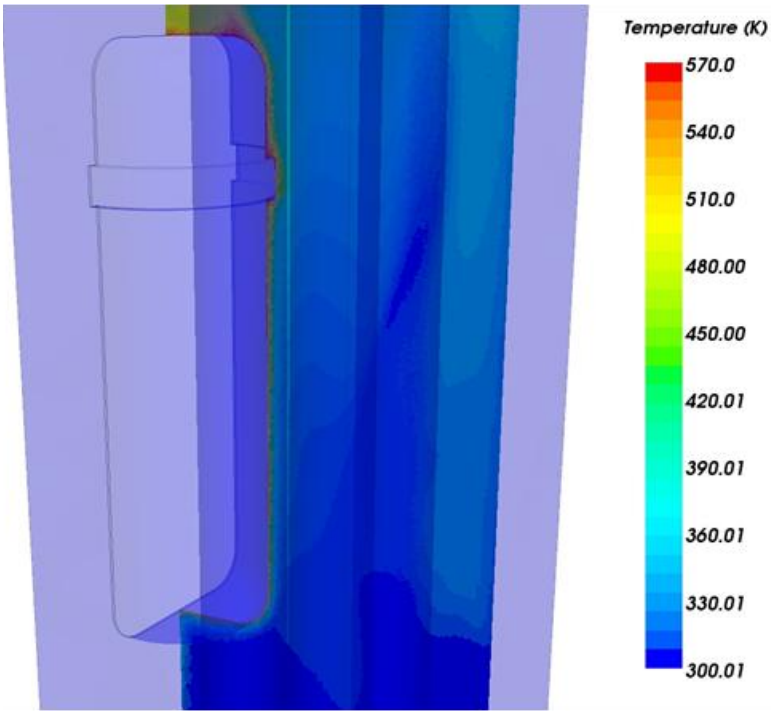

Fig. 47 – Temperature distribution in the cavity middle par) – Test #3

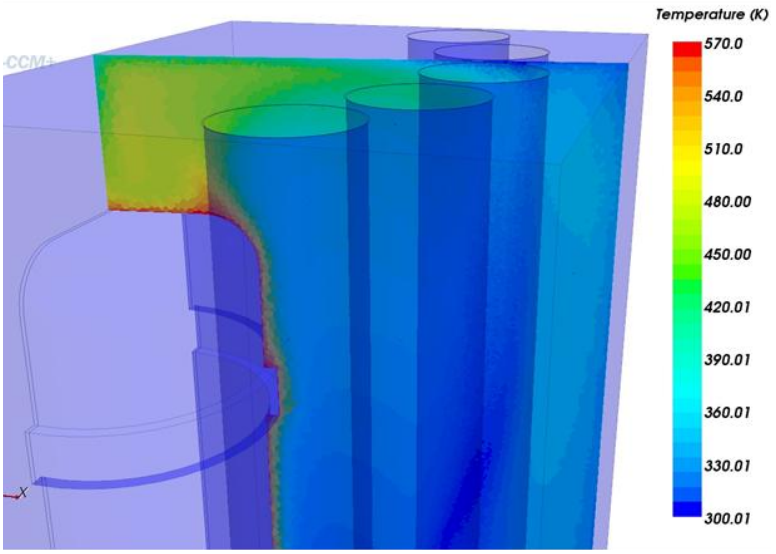

Fig. 48 – Temperature distribution in the RCCS cavity region upper part – Test #3

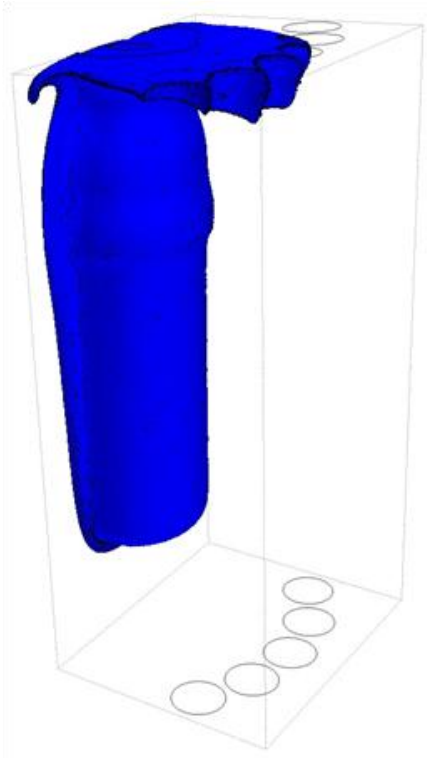

Fig. 49 – Temperature isosurface in the RCCS cavity region – Test #3

In Fig. 50 is shown the velocity magnitude isosurface in the RCCS cavity region. The figure shows that the largest air velocity inside the RCCS cavity is close to the RPV wall, and at the gap between the standpipes walls. Also the largest vorticity (i.e., velocity gradients) is reached in the gap between standpipes walls, as shown in Fig. 51.

In Fig. 52 is shown the velocity vector distribution in the RCCS cavity region on a plane parallel to the RPV and standpipes axes (see upper right corner of Fig. 52). The figure addresses the presence of many secondary recirculation regions. In the upper part of the cavity region, there are two symmetric recirculation regions. Another two recirculation regions are present at about half the height of the cavity region. These two recirculation regions break the symmetry of the RCCS. The experimental facility and the CFD model were built in such a way to have a symmetry plane passing through the RPV region, the cavity region, and the central standpipes. Fig. 52, and the following figures show that, even with a symmetric geometry, due to the intrinsic instability of the system, the velocity distribution is not symmetric in the cavity region. In the bottom part of the cavity region are present two more secondary recirculation regions.

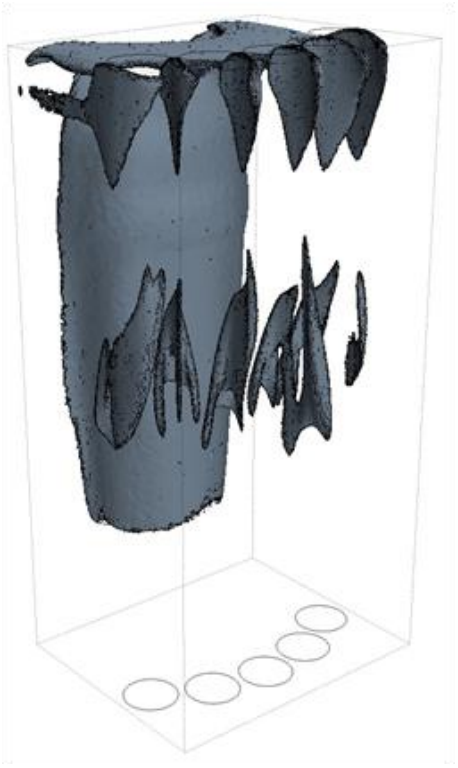

Fig. 50 – Velocity magnitude isosurface in the RCCS cavity region – Test #3

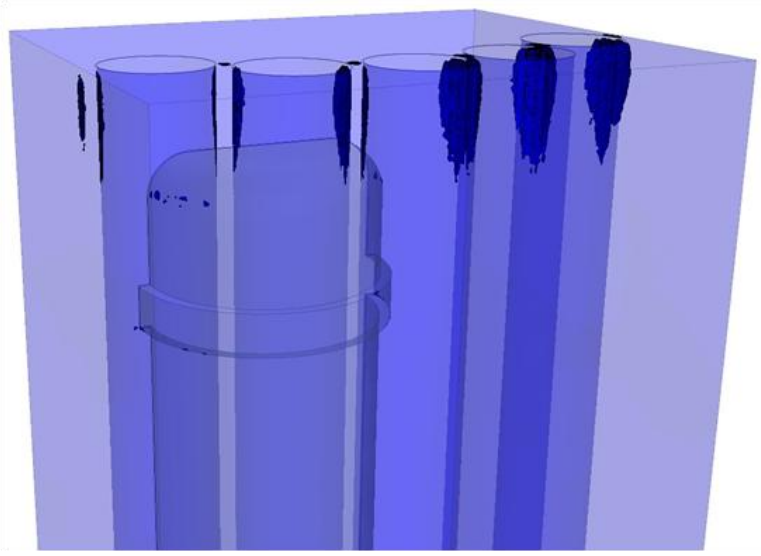

Fig. 51 – Vorticity magnitude isosurface in the cavity region upper part – Test #3

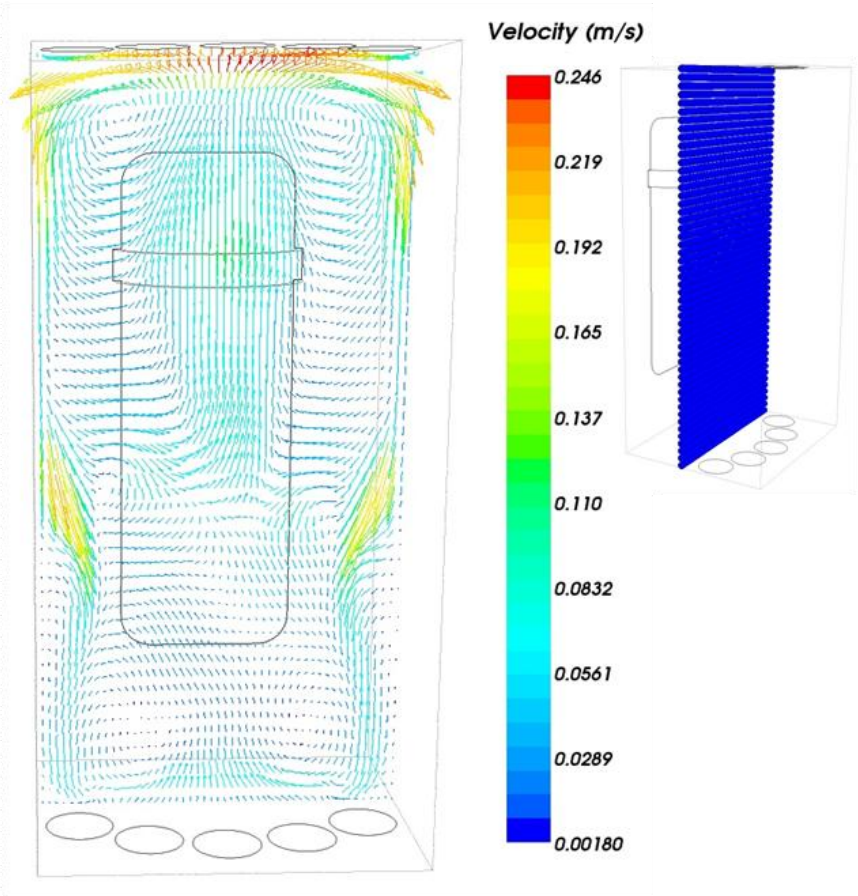

Fig. 52 – Velocity vector distribution in the cavity region (a) – Test #3

In Fig. 53 is shown the velocity vector distribution at half height of the RCCS cavity region (see upper right corner of Fig. 53). The figure shows that also for the plane normal to the RPV and the standpipes axes there are some secondary recirculation regions. In particular, a relevant fraction of the lighter air moving towards the top of the cavity region, passing through the gap between the standpipes, hits the back wall. This explains why the back wall maximum temperature is reached close to the upper cavity wall (see Fig. 36 - Fig. 40). Then the air moves downwards cooled by the standpipes wall and the cavity back wall. Fig. 53 points out that the air close to the cavity back wall

is forced through the narrow gaps between each couple of standpipes creating some kind of “jet” flow patterns. This behavior determines the formation of secondary recirculation regions in direction normal to the RPV and standpipes axes. There are some secondary motions of the air close to the RPV wall in the azimuthal and radial directions. The figure also shows that these secondary recirculation regions are not symmetric respect to the model symmetry plane.

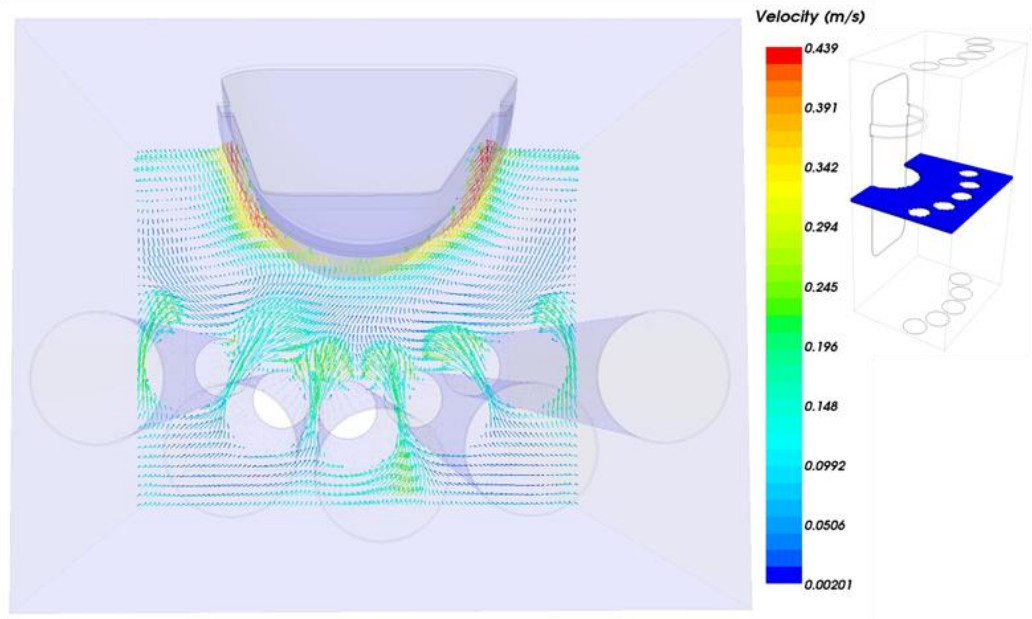

Fig. 53 – Velocity vector distribution in the cavity region (b) – Test #3

In Fig. 54 and Fig. 55 are shown the velocity vector and the azimuthal velocity distribution at the cavity region symmetry plane (see upper right corner of Fig. 54 and Fig. 55). Fig. 54 addresses the main recirculation region between the RPV wall and the standpipes wall. Also secondary recirculation regions are present in the cavity above the upper RPV head, and in the gap between the standpipes wall and the cavity back wall.

By symmetry of the model, the azimuthal velocity distribution (normal to the plane considered, positive if pointing out of the plane) should be zero on the symmetry plane. Due to the inherent instability in the physics of the problem simulated, the model predicts some secondary motions on the symmetry plane in the cavity region behind the standpipes wall and above the RPV upper head (i.e., the azimuthal component of the velocity is different from zero at the symmetry plane).

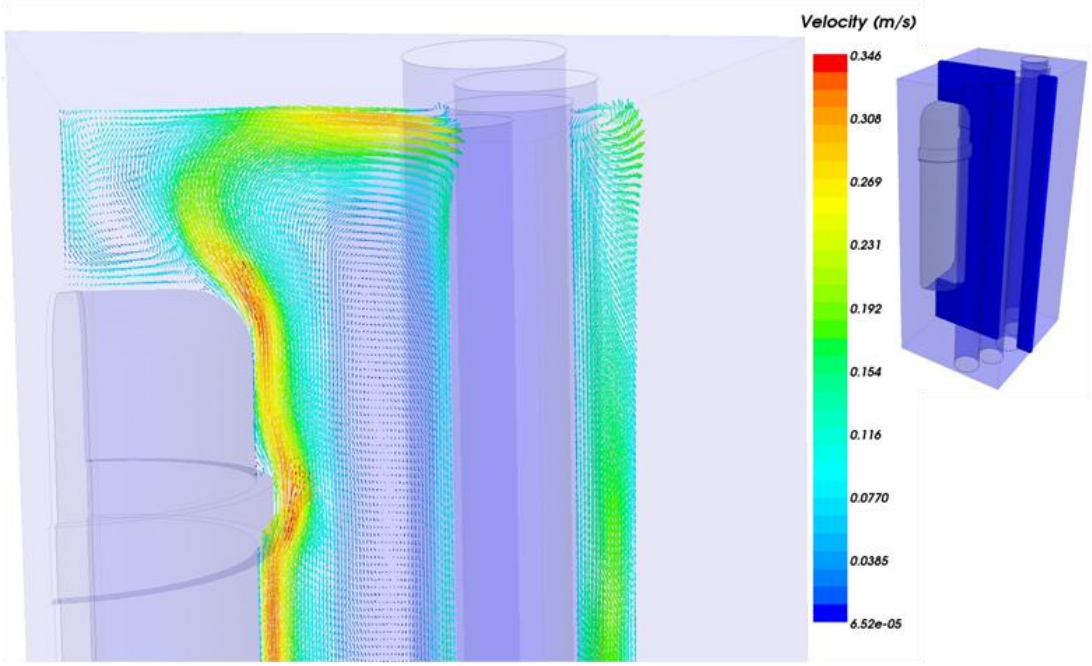

Fig. 54 – Velocity vector distribution on the RCCS cavity symmetry plane – Test #3

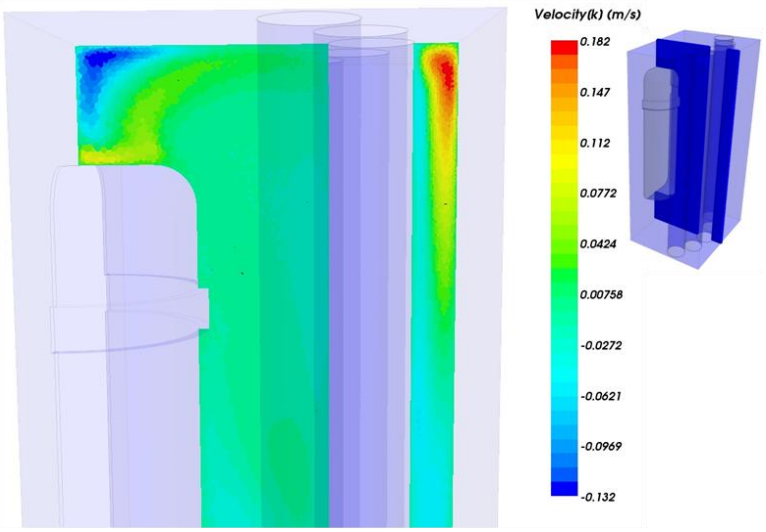

Fig. 55 – Azimuthal velocity distribution on the cavity symmetry plane – Test #3

The CFD simulations allowed to determine the fraction of energy transferred to the standpipes by radiation and convection heat transfer phenomena, respectively. For the boundary conditions set in Test #3, the CFD simulation determined a value of 54% and 46% due to radiation and convection heat transfer, respectively. The scaling analysis developed in Section 4 allowed to have a rough estimate of the effects due to radiation and convection heat transfer in the RCCS cavity. For Test #3 the respective values were 60.8% and 39.2%, with an error between the scaling analysis and the CFD simulations equal to 11.2%.

In Fig. 56 through Fig. 59 are shown the temperature distribution in the radial direction at cavity region symmetry plane and the central standpipe region for different elevations, respectively. In particular, Fig. 56 shows the radial temperature distribution at 55 mm from the cavity bottom wall (line probe 1). The figure shows that the air in proximity of the RPV bottom head and cavity wall is at a temperature slightly higher

than the air in the central RCCS cavity region. This determines a very small buoyancy effect (i.e., a gradient of density in the lower part of the RCCS cavity), which explains the recirculation region, even if very small axial velocity are present, as can be seen from Fig. 60. In Fig. 56 is also shown the air temperature distribution in the RCCS cavity region close to the central standpipe walls, along the central standpipe walls section, in the central standpipe riser and downcomer regions. The figure shows that there is a small temperature gradient at the bottom of the RCCS cavity region, meanwhile the temperature distribution is practically constant inside the different central standpipe regions.

In Fig. 57 is shown the radial temperature distribution inside the RCCS cavity region from the RPV wall to the cavity back wall, and inside the central standpipe regions at 135 mm from the RCCS cavity bottom wall (line probe 2). The figure shows that there is a very large temperature gradient close to the RPV wall. On the other hand, inside the central standpipe region, the temperature is almost constant across the walls thickness and in the coolant region (i.e., downcomer and riser).

In Fig. 58 is shown the radial temperature distribution from the RPV wall to the RCCS cavity back wall at 215 mm from the cavity bottom wall (line probe 3). The temperature profile is similar to that shown in the previous figure, with the only difference that a larger temperature gradient is present as the air rises towards the upper of the cavity region (see Fig. 36 through Fig. 39). In Fig. 59 is shown the radial temperature distribution in the upper part of the RCCS cavity, 275 mm from the cavity bottom wall (line probe 4). The figure shows the secondary recirculation region above

the RPV upper head, and the temperature gradient between the RPV wall and the central standpipe wall. The temperature distribution inside the central standpipe region is almost constant. As addressed before, this is due to the imposed mass flow rate for Test #3. The fact that the ratio of *Ri* number is much smaller than one addresses the forced circulation conditions present in the experimental facility/CFD model. With the imposed standpipes mass flow rate, the temperature gradient across the standpipes streamwise and spanwise directions is very small.

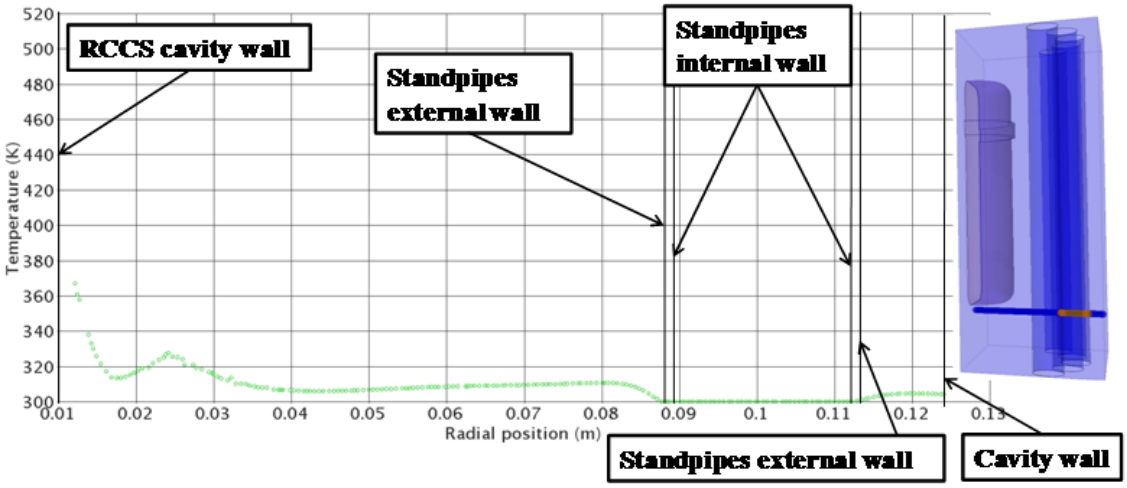

Fig. 56 – Cavity region radial temperature distribution (line probe 1) – Test #3

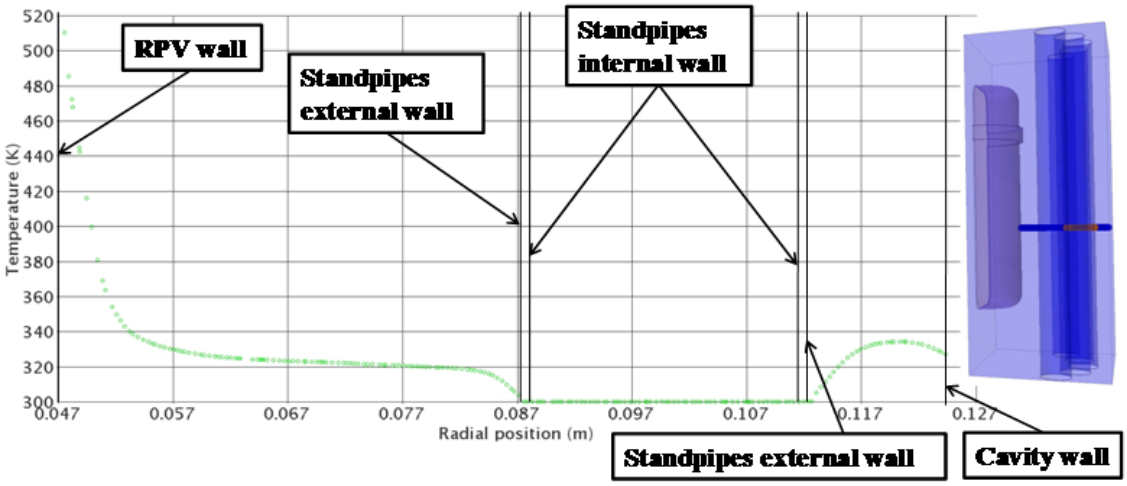

Fig. 57 – Cavity region radial temperature distribution (line probe 2) – Test #3

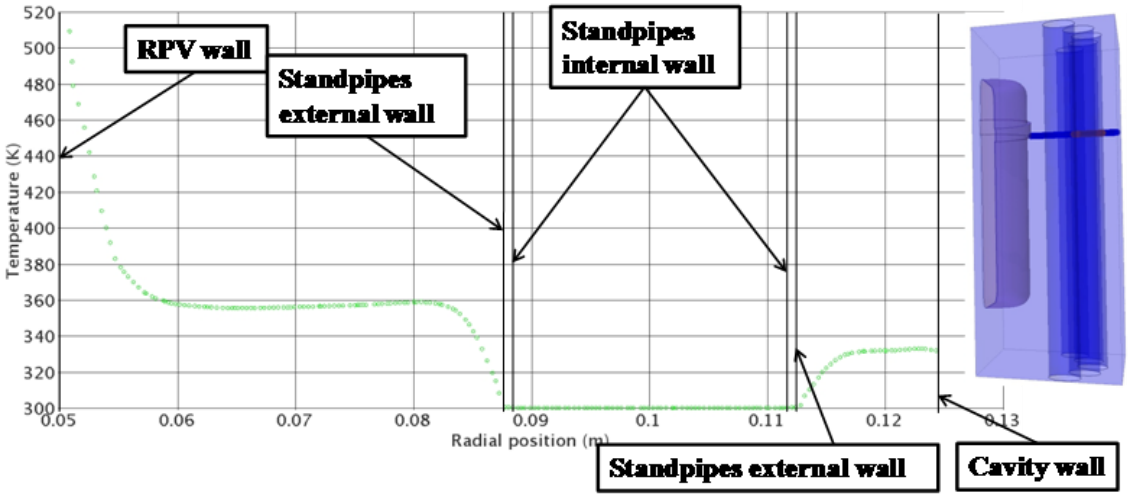

Fig. 58 – Cavity region radial temperature distribution (line probe 3) – Test #3

\

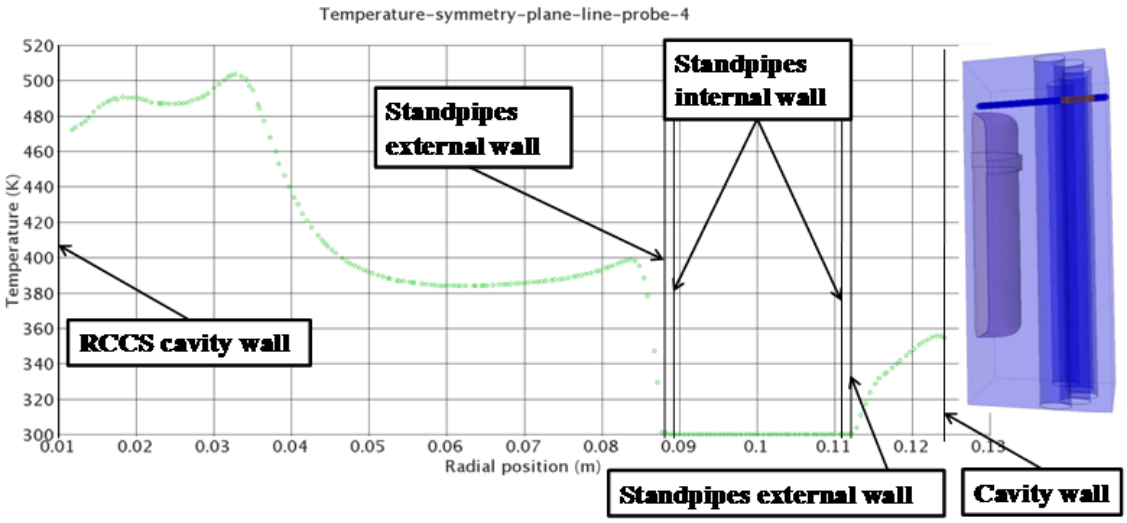

Fig. 59 – Cavity region radial temperature distribution (line probe 4) – Test #3

In Fig. 60 through Fig. 63 is shown the axial velocity distribution in the radial direction at the cavity region symmetry plane for different elevations, respectively. In Fig. 60 the axial velocity spans the RCCS cavity region from the left wall to the central standpipe wall. The axial velocity is taken at 55 mm from the cavity region bottom wall (line probe 1). As before discussed, there is a recirculation region below the RPV lower head, but the air velocity is close to zero across the RCCS cavity (the air is almost stagnant). Close to the standpipe wall the air shows a very small negative velocity (i.e., it is moving downwards). This represents the tail of the main recirculation path present in the gap region between the hot RPV wall and the cold standpipes wall. The main recirculation path in the cavity region can be better addressed in Fig. 61 and Fig. 62 , which plot the axial velocity profiles taken at 135 mm (line probe 2) and 215 mm (line probe 3) from the cavity bottom wall, respectively. Close to the RPV wall the air is

accelerated upwards by to buoyancy forces. After reaching a local maximum, the velocity gradient becomes negative, and a few millimeters away from the RPV wall also the velocity is negative (i.e., air is moving downwards). Fig. 62 shows that moving towards the upper part of the RCCS cavity region, the local maximum axial velocity increases and also the thermal boundary layer becomes thicker. This means that the velocity profile is far away from being fully developed. Buoyancy effects are underestimated from the experimental facility/CFD model respect to the real plant conditions, since the thermal boundary layer is still developing. A much larger heated length would be necessary to have buoyancy forces in the experimental facility of the same order as those present in the real plant, or a much larger temperature gradient across the RCCS cavity would give the same effect. Since neither the former nor the latter could be reached in the experimental facility, this justifies for the six order of magnitude smaller *Ra* number (i.e., much smaller buoyancy forces) present in the CFD model with respect to the real plane cavity region conditions.

In Fig. 63 is shown the axial velocity distribution across the RCCS cavity at 275 mm from the RCCS bottom wall (line probe 4). The figure shows the secondary recirculation region above the RPV upper head, and the upper part of the main recirculation path between the RPV wall and the central standpipe wall.

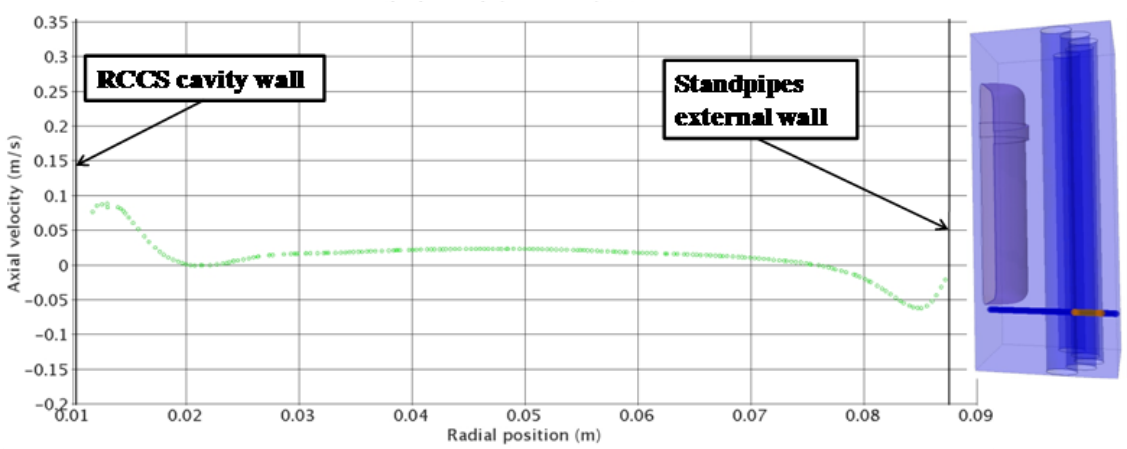

Fig. 60 – Cavity region axial velocity distribution (line probe 1) – Test #3

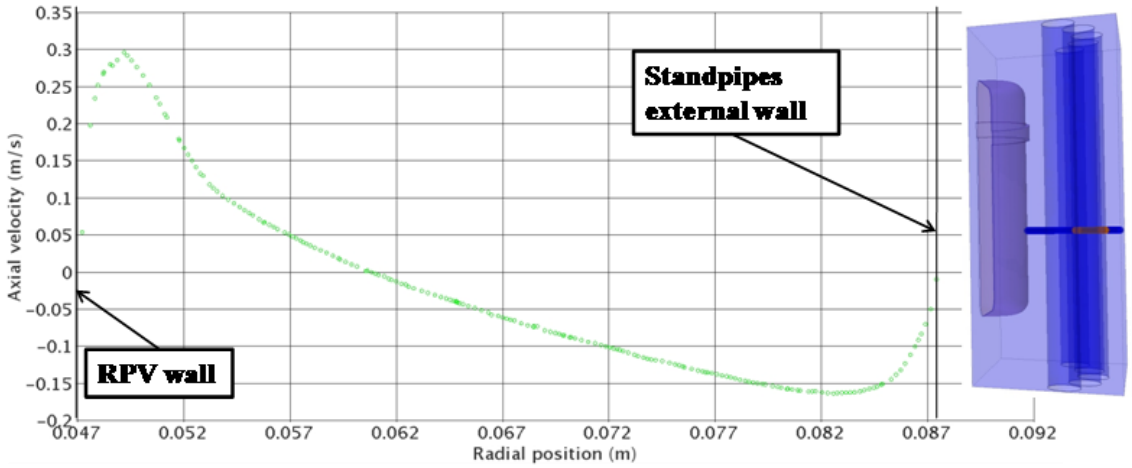

Fig. 61 – Cavity region axial velocity distribution (line probe 2) – Test #3

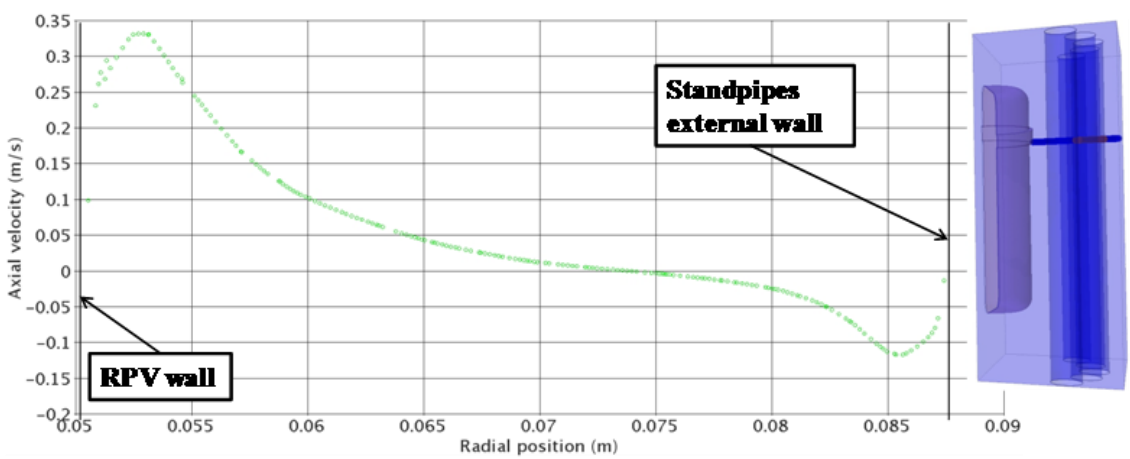

Fig. 62 – Cavity region axial velocity distribution (line probe 3) – Test #3

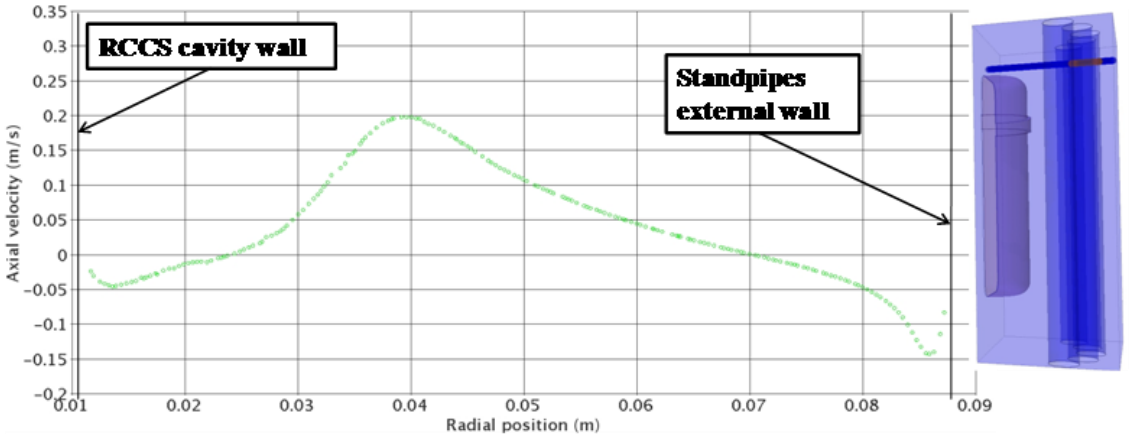

Fig. 63 – Cavity region axial velocity distribution (line probe 4) – Test #3

6.2 Analysis of the RCCS Water-Cooled Configuration (Test #8)

Test #8 was performed setting a uniform volumetric power inside the RPV region, which gives a total power generated equal to 27 W when integrated over the total RPV volume. The other boundary conditions are shown in Table 13. In Fig. 64 is shown the PRV wall temperature distribution obtained using the Realizable k-ε turbulence model with Two-Layer *all* y^+ Near-Wall treatment. Due to the very high thermal conductivity

of the RPV material (Cu was assumed for the simulations based on the material used for the experimental facility), the temperature at the RPV wall is almost uniform. The temperature gradient of 0.52 K present between the top and the bottom of the RPV wall is due to the cooling of air by free convection. The boundary conditions for this analysis were set in such a way to have a very small mass flow rate inside the standpipes (i.e., natural circulation conditions were simulated), and to have a reduced temperature gradient across the RCCS cavity region (i.e., the RPV wall temperature is much lower than that imposed for Test #3). The figure shows that the RPV wall maximum temperature is reached at the RPV upper head.

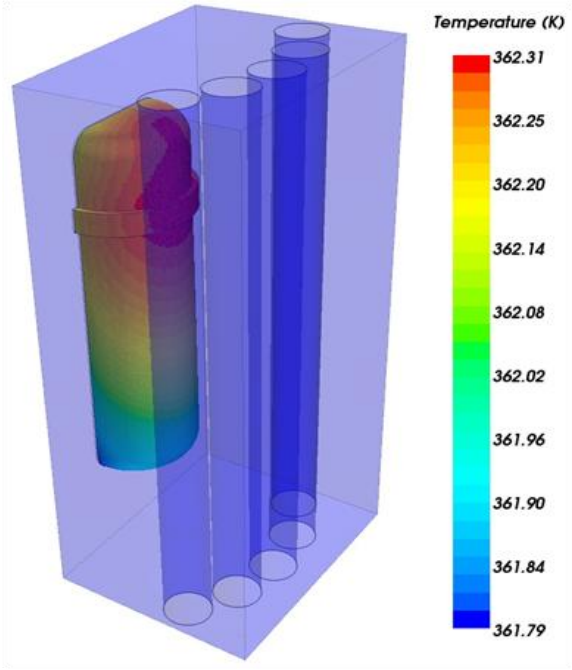

Fig. 64 – RPV wall temperature distribution – Test #8

In Fig. 65 through Fig. 69 is shown the sensitivity analysis over mesh refinement for the axial temperature distribution at the cavity region rack plane and different radial

distances from the RPV wall, respectively. As Table 20 addresses, mesh convergence was tested progressively increasing the number of cells in the RCCS cavity and the standpipes regions. Due to the inherent instability of free convection and natural circulation phenomena, the residuals show some oscillatory behavior with a period of oscillation depending on mesh refinement and boundary conditions set. To analyze mesh convergence an extensive measurement of temperature and velocity distributions was carried out in the RCCS cavity region. This criterion was used to judge mesh convergence for the analyses performed. The figures show that there are some discrepancies in the temperature profiles between the different meshes, especially close to the RCCS top wall. The differences in temperature distributions were expected due to the different mesh refinements necessary to calculate the heat exchange at the interfaces between fluid and solid regions (i.e., conjugate heat transfer). Solution convergence was obtained for each mesh, based on energy balance equations between the power introduced in the system and the power dissipated by the system (i.e., by cooling inside the standpipes and heat losses through the cavity external walls). Unfortunately mesh convergence was not completely reached since the different meshes gave different values for the fraction of energy dissipated by cooling and the fraction of energy due to heat losses, for the temperature and velocity distributions inside the cavity region, etc. This is an issue that requires further analysis and a larger effort on mesh convergence is demanded.

In Fig. 65 is shown the axial temperature distribution in the RCCS cavity 5.0 mm from the RPV wall at the rack plane location (line probe 1). The figure shows a local

maximum in the air temperature in proximity of the RPV flange. The flange represents an obstruction for the thermal boundary layer developing along the RPV wall, and a local minimum in the axial velocity is present close to the RPV wall at the flange location. This explains why the air temperature shows a local maximum close to the flange. The air temperature progressively increases from the RCCS bottom wall towards the upper part of the cavity as the air becomes lighter and cools down the RPV wall. The maximum air temperature is reached in the upper part of the cavity.

In Fig. 66 and Fig. 67 are shown the axial temperature distribution in the RCCS cavity region at 30 mm (line probe 2) and 40 mm (line probe 3) from the RPV wall, respectively (rack plane location). The figures show the same temperature trend as Fig. 65, with a smoother temperature gradient in the bottom half of the cavity, and a much larger temperature gradient in the upper half of the cavity. This behavior is due to the cooling effect of the standpipes. The air, once reaches the cavity top wall, moves downwards being cooled along the standpipes walls in the upper part of the RCCS cavity. The cooling effect of the standpipes is such that, at half the height of the RCCS cavity region the air temperature is very close to the standpipes wall temperature. This is due to the very large heat transfer capability of the experimental facility/CFD models standpipes realized (see discussion on the St number ratio is section 4.0). This temperature distribution inside the RCCS cavity addresses the fact that the main recirculation region develops in the upper half of the cavity, with air being stagnant in the lower cavity region. In Fig. 68 is shown the axial temperature distribution in the cavity region between the central standpipe and the adjacent one, at the rack plane

location (line probe 4). The figure shows that at about half the RCCS cavity height there is a local maximum in the air temperature with a negative gradient. This behavior is due to the fact that in the upper part of the RCCS cavity the maximum velocity is reached in the gap between standpipes, meanwhile in the lower part of the RCCS cavity region air is at almost stagnant conditions and, therefore, being forced between two standpipes the air temperature locally increases.

In Fig. 69 is shown the axial temperature distribution at the cavity back wall (line probe 5). With the relatively small power generated inside the RPV region (i.e., lower RPV wall temperature), the cavity back wall temperature ranges from 300 K in the bottom part up to 320 K close to the cavity top wall. This temperature is well below the concrete material design limits. With the boundary conditions imposed for Test #8, the RCCS cooling system is capable of removing a sufficient amount of heat from the cavity to maintain the RPV wall and the concrete walls below design limits.

The mesh sensitivity analysis shows that the finer meshes predict higher temperature distribution inside the cavity region with respect to the coarser meshes. This behavior is due to the fact that finer meshes show a more accurate prediction of the heat exchange at the RPV wall. Due to the sharp temperature gradients close to the RPV wall, it is extremely important to have very fine meshes in proximity of the vessel wall, if a better prediction of temperature profiles, buoyancy effects and, therefore, velocity distributions in the cavity region want to be obtained.

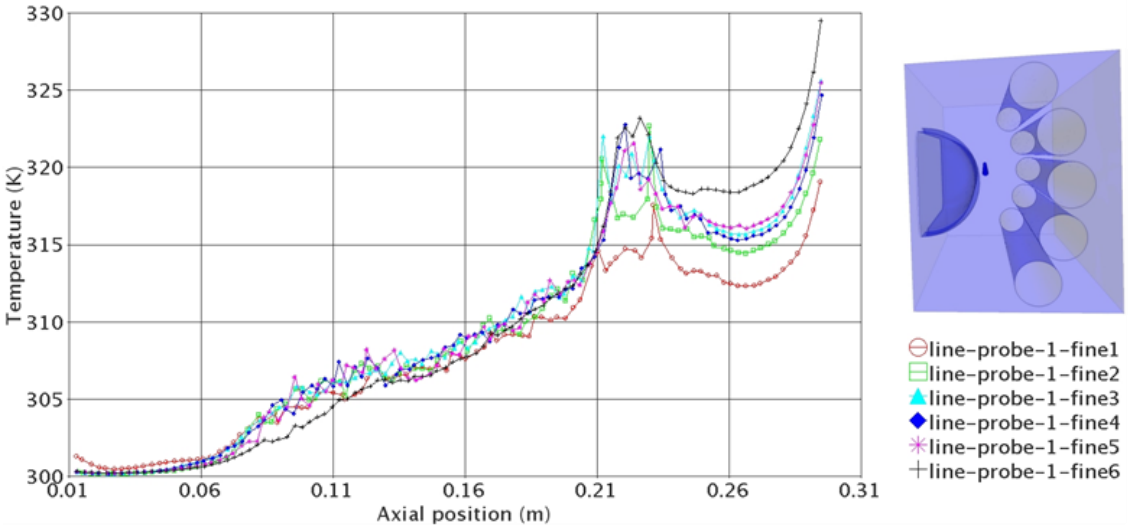

Fig. 65 – Cavity region axial temperature distribution (line probe 1) – Test #8

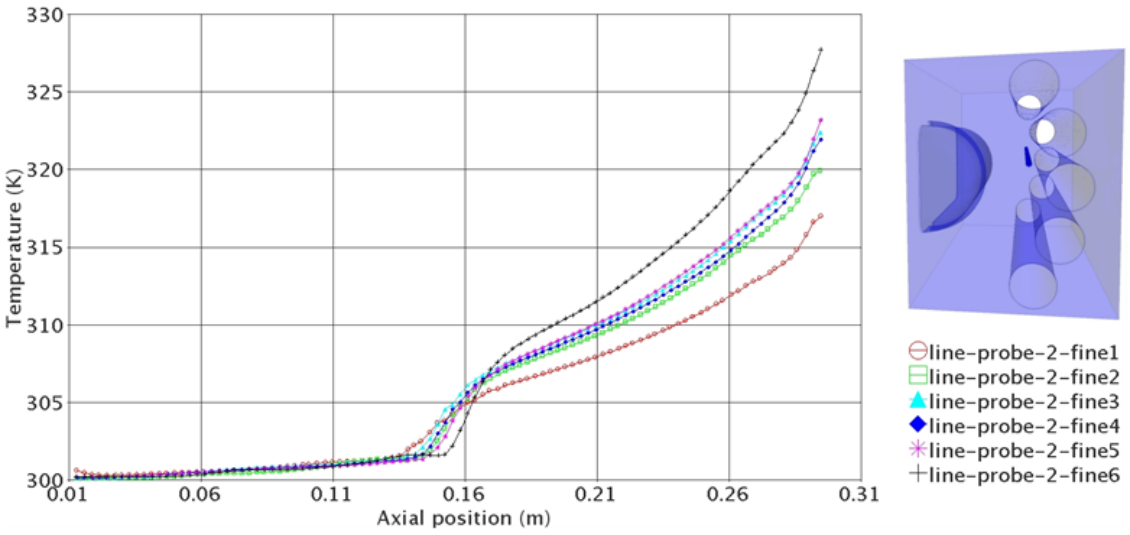

Fig. 66 – Cavity region axial temperature distribution (line probe 2) – Test #8

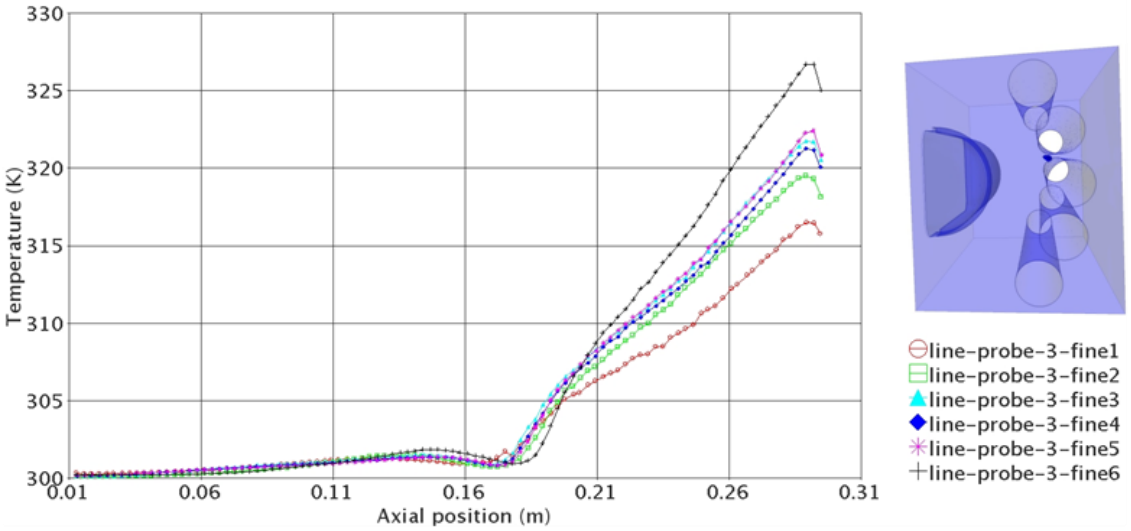

Fig. 67 – Cavity region axial temperature distribution (line probe 3) – Test #8

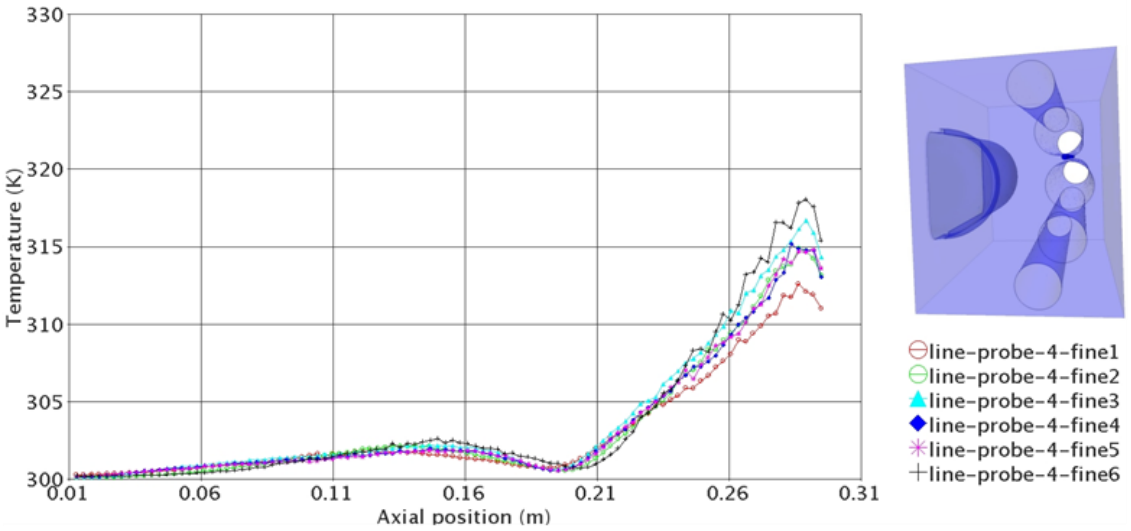

Fig. 68 – Cavity region axial temperature distribution (line probe 4) – Test #8

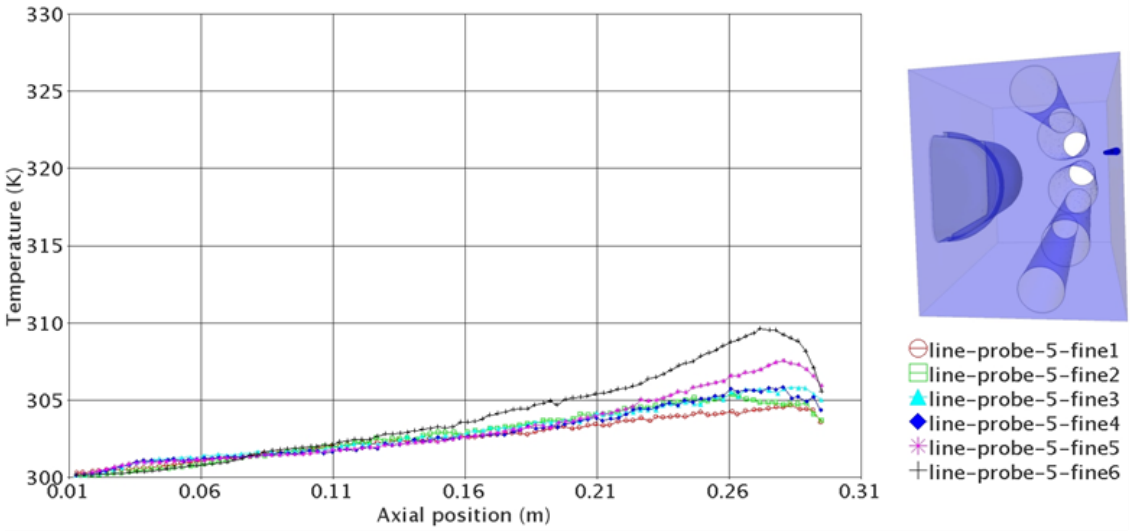

Fig. 69 – Cavity region axial temperature distribution (line probe 5) – Test #8

In Fig. 70 is shown the calculated temperature distribution at the standpipes external wall for test #8. Even for the reduced mass flow rate imposed at the standpipes, the standpipes wall temperature slightly increases axially. This result confirms that the RCCS water-cooled configuration represents an effective cooling system for the RCCS cavity walls.

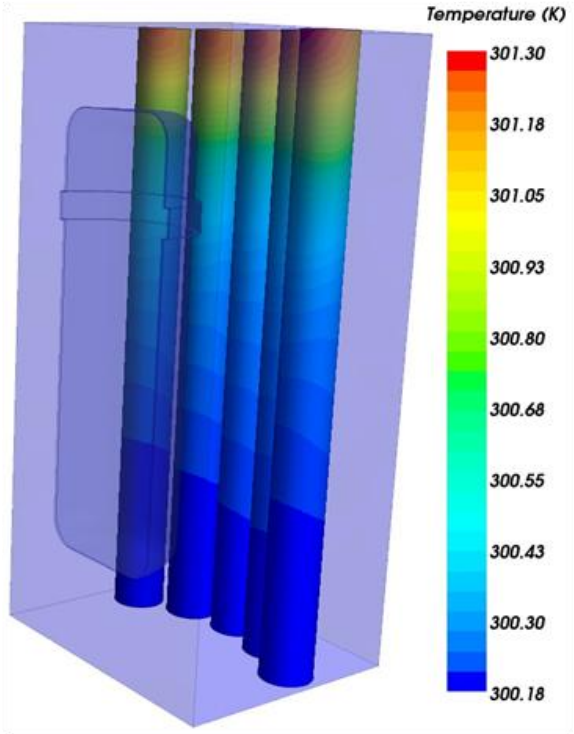

Fig. 70 – Temperature distribution at the standpipes wall – Test #8

In Fig. 71 and Fig. 72 are shown the velocity vector and the temperature distribution in the RCCS cavity region at the rack plane location for Test #8. The velocity vector plot shows the main recirculation region in the upper half part of the RCCS cavity region between the RPV wall and the standpipes wall. Also the stagnant region below the RPV lower head and the smaller recirculation region above the RPV upper head can be seen. The maximum velocity is reached at the gap between standpipes in the upper part of the RCCS cavity region. Due to the lower RPV wall temperature for Test #8 respect to Test #3, buoyancy effects are reduced in Test #8. This means that the velocity distribution inside the cavity is smoother for Test #8 with respect to Test #3.

The temperature distribution plot (see Fig. 72) in the cavity region addresses the stagnant air conditions in bottom part (i.e., an almost uniform temperature distribution is present in this region). Close to the RPV bottom head the air temperature rapidly increases and is driven by buoyancy upwards the RPV temperature wall. The maximum air temperature is reached at the RPV upper head where separation and reattachment regions are present.

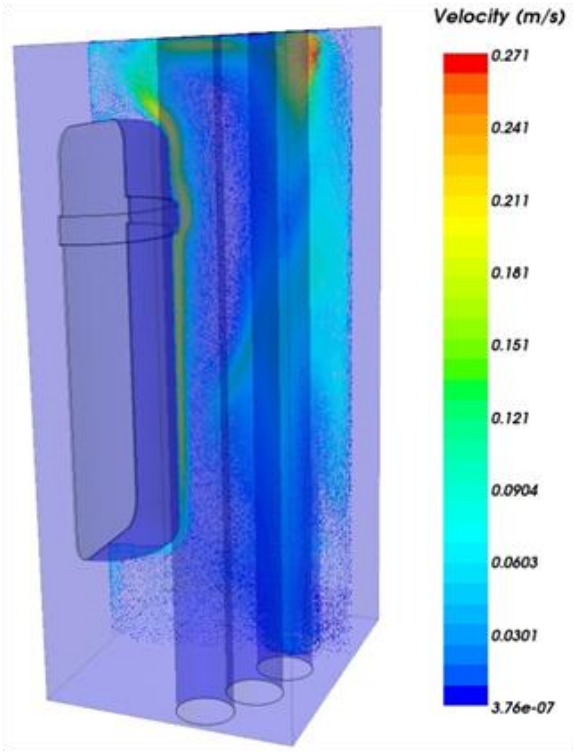

Fig. 71 – Velocity vector distribution in the cavity region (rack plane) – Test #8

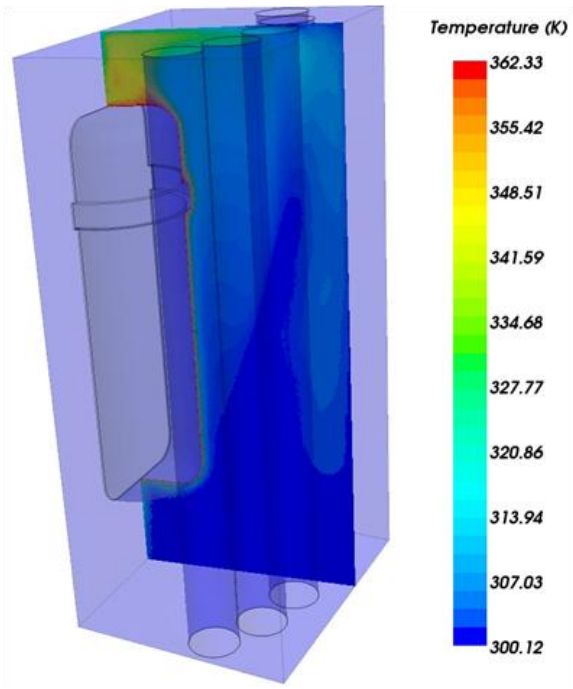

Fig. 72 – Temperature distribution in the cavity region (rack plane) – Test #8

In Fig. 73 and Fig. 74 are shown the radial temperature distribution in the RCCS cavity region at the symmetry plane, 215 mm (line probe 3) and 275 mm (line probe 4) from the bottom wall, respectively. Fig. 73 shows the radial temperature distribution at the RPV flange location. Close to the RPV wall a sharp temperature gradient is present. The thermal boundary layer is becoming thicker as the air rises along the RPV wall due to buoyancy forces. The figure also shows that there is some scatter in the temperature distribution close to the wall for the different meshes analyzed. Finer meshes predict larger temperatures close to the RPV and across the cavity region. The temperature distribution in the central standpipes regions is almost constant.

In Fig. 74, the temperature distribution in the upper part of the RCCS cavity region (i.e., 275 mm from the bottom region) is shown. The effect of mesh refinement is even

more evident in Fig. 74. There is a difference of almost 20 K between the coarsest and finest meshes analyzed, with the finer mesh predicting higher temperature distribution. The effect of mesh resolution influences the temperature gradient distribution close to the RPV wall. This in turn influences the effect of buoyancy forces which are the driving phenomenon in the momentum equations. Therefore, different velocity distributions will be obtained for the different meshes, and since the velocity distribution close to the vessel wall strongly influences the temperature distribution in this region, the resulting effect is sensible differences in the temperature distributions for the different meshes analyzed close to the RPV wall and in the upper part of the cavity region are obtained refining the mesh.

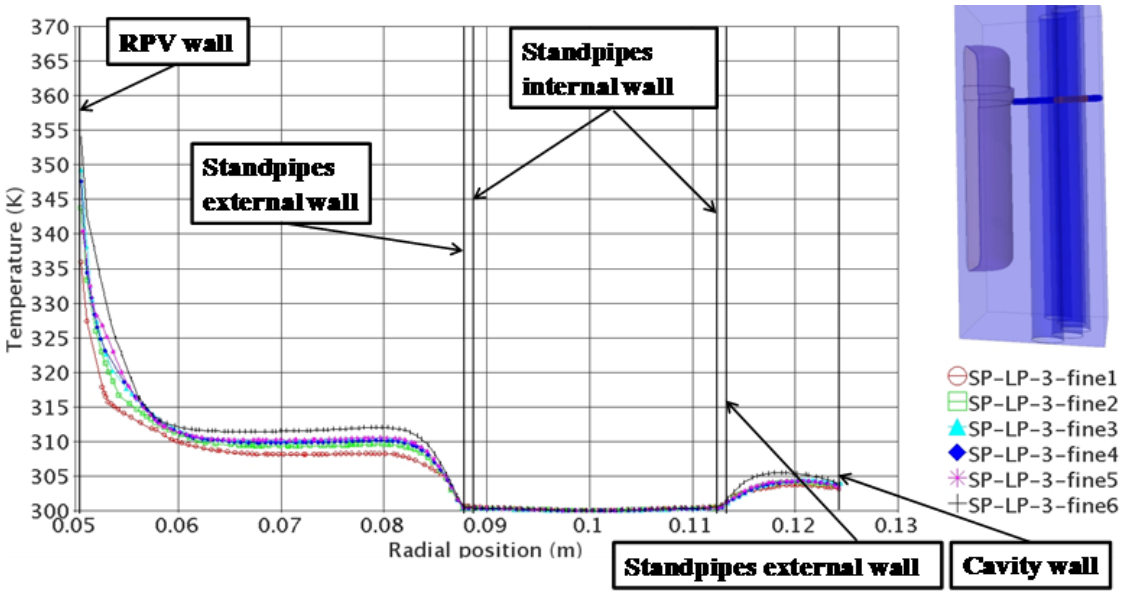

Fig. 73 – Cavity region radial temperature distribution (line probe 3) – Test #8

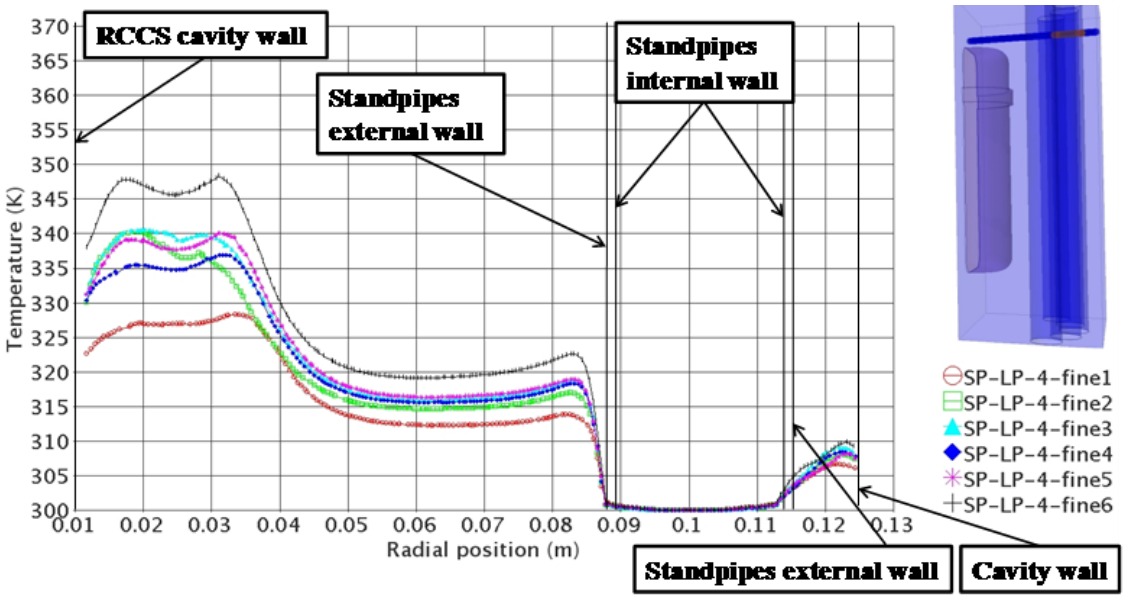

Fig. 74 – Cavity region radial temperature distribution (line probe 4) – Test #8

In Fig. 75 and Fig. 76 are shown the axial velocity distribution in the radial coordinate at the cavity region symmetry plane, 215 mm (line probe 3) and 275 mm (line probe 4) from the bottom wall, respectively. Fig. 75 shows the axial velocity distribution at the RPV flange location. The different refinements close to the RPV wall give large differences on the velocity distribution close to the vessel wall. Finer meshes predict a larger buoyancy effect and, therefore, larger axial velocities close to the RPV wall. This effect is strongly reduced close to the standpipes wall due to the reduced temperature gradients.

Fig. 76 shows the mesh sensitivity for the axial velocity distribution in the upper part of the cavity region at the symmetry plane. The different predictions in buoyancy forces, separation and reattachment region at the RPV upper head and temperature

distribution in the thermal boundary layer determine different velocity profiles in the upper part of the cavity region.

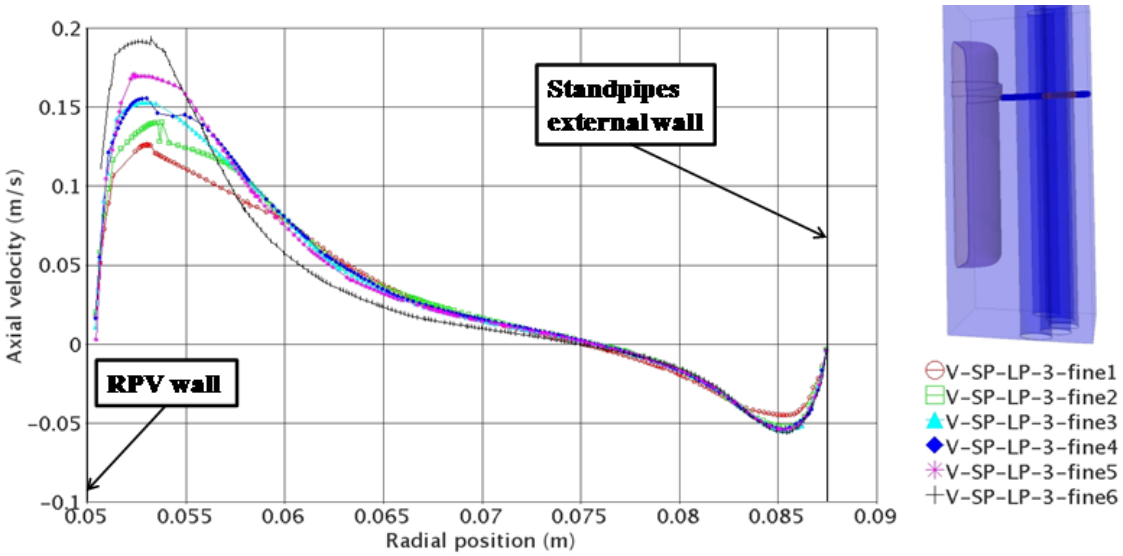

Fig. 75 – Cavity region axial velocity distribution (line probe 3) – Test #8

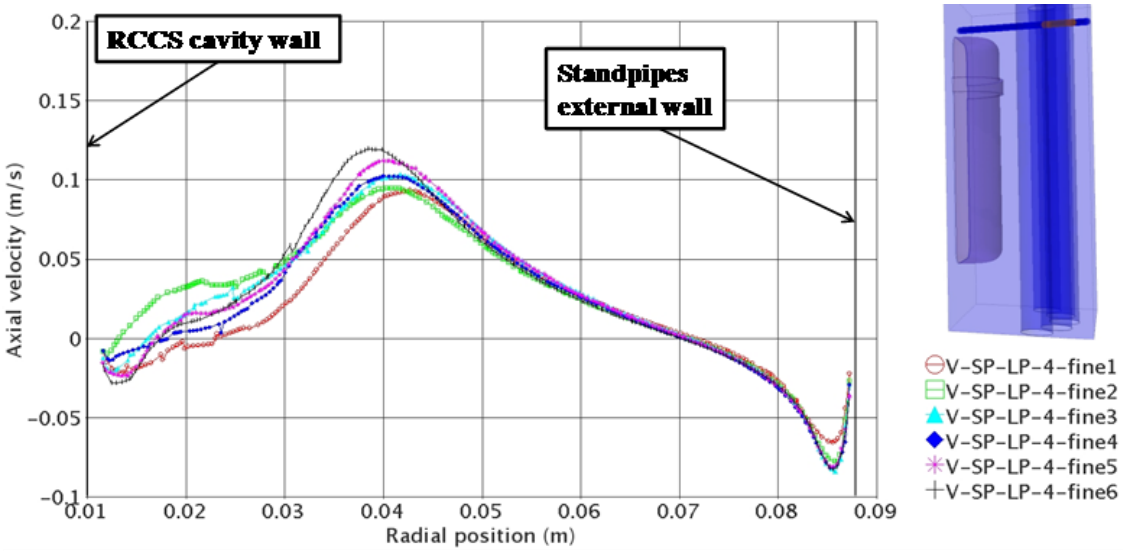

Fig. 76 – Cavity region axial velocity distribution (line probe 4) – Test #8

For the scaling of convection and radiation heat transfer across the RCCS cavity region, the simulation predicted 38.9% due to radiation and 61.1% due to convection heat transfer phenomena, respectively. These values are in satisfying agreement with those obtained from the scaling analysis for Test #8 (3% error), which are 40.2% and 59.8% due to radiation and convection heat transfer, respectively. The relatively small fraction of heat transfer due to radiation is explained with the reduced heat power imposed inside the RPV region, which determine a lower RPV wall temperature respect to Test #3. Since the heat transfer exchanged by radiation goes as the forth power of the difference temperature between the RPV wall and the standpipes wall temperature, with a lower RPV wall temperature, the effect of radiation is reduced. This analysis was performed to address the behavior of the standpipes for the CFD model under conditions very similar to the real plant standpipes ones (i.e. a ratio of *Ri* number close to one).

6.3 Analysis of the RCCS Water-Cooled Configuration (Test #9)

Test #9 was performed setting a uniform volumetric power inside the RPV region, with a total power generated equal to 50 W (see Table 13). In Fig. 77 is shown the PRV wall temperature comparison for Test #8 and #9 obtained using the Realizable k-ε turbulence model with Two-Layer all y^+ Near-Wall treatment. Also for Test #9, due to the very high thermal conductivity of the RPV material, the temperature at the RPV wall is almost uniform, with a temperature difference between the bottom and the top RPV heads less than 1.0 K. Fig. 77 also shows that the RPV wall maximum temperature is at the RPV upper head. A very small standpipes mass flow rate was imposed in such a way to simulate natural circulation conditions.

In Fig. 78 and Fig. 79 is shown the sensitivity over mesh resolution for the axial temperature distribution at the cavity region rack plane, 0.25 mm (line probe 1) from the RPV wall and at the cavity back wall (line probe 5), respectively. The figures show that there are some discrepancies in the temperature profiles between the different meshes, especially close to the RPV wall and in the upper part of the RCCS cavity region. The differences in temperature distribution were expected due to the different mesh refinement necessary to calculate the heat exchange at the interfaces between fluid and solid regions. In Fig. 78, the sharp temperature increase at about 0.21 m from the cavity bottom wall is due to the RPV flange. The figure shows that there is a difference of about 20 K between the coarsest and finest meshes analyzed, with the latter predicting higher temperature inside the cavity region.

In Fig. 79 is shown the temperature distribution at the cavity back wall. Also for this analysis the back wall temperature does not exceed 325 K, which is very close to the maximum value reached for Test #8 (i.e., 320 K). This temperature is below the concrete walls design limits. This analysis shows that the increase in the cavity walls peak temperature is very small even if the power generated inside the RPV region was doubled.

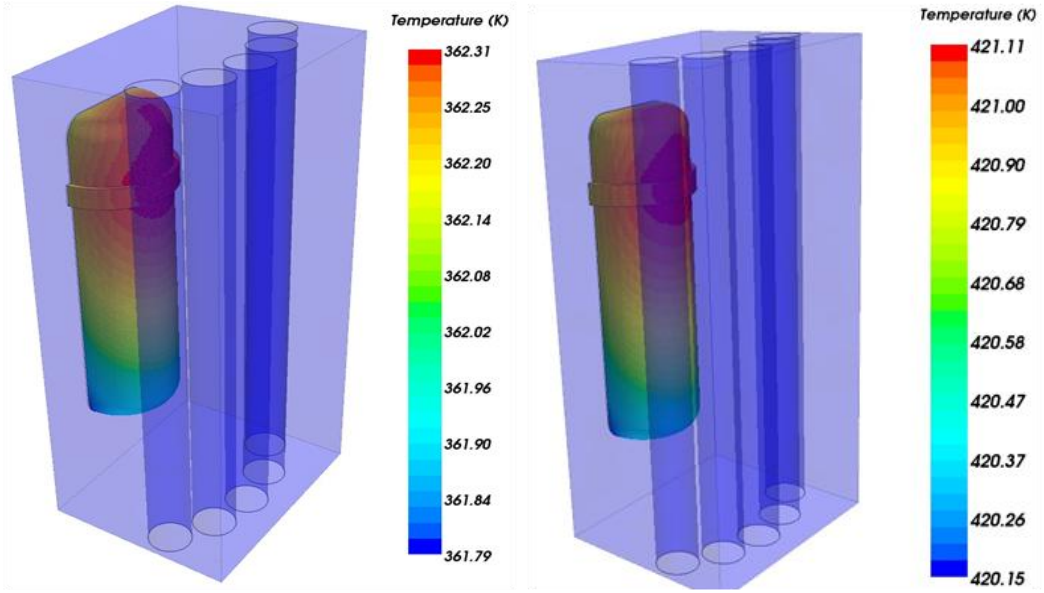

Fig. 77 – RPV wall temperature distribution – Test #8 (left)/9 (right)

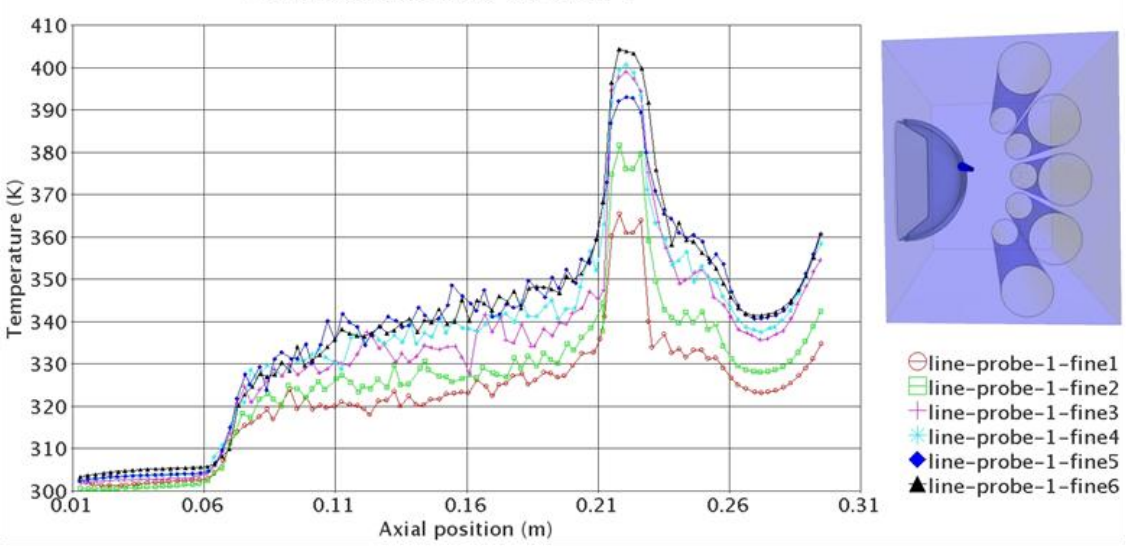

Fig. 78 – Cavity region axial temperature distribution (line probe 1) – Test #9

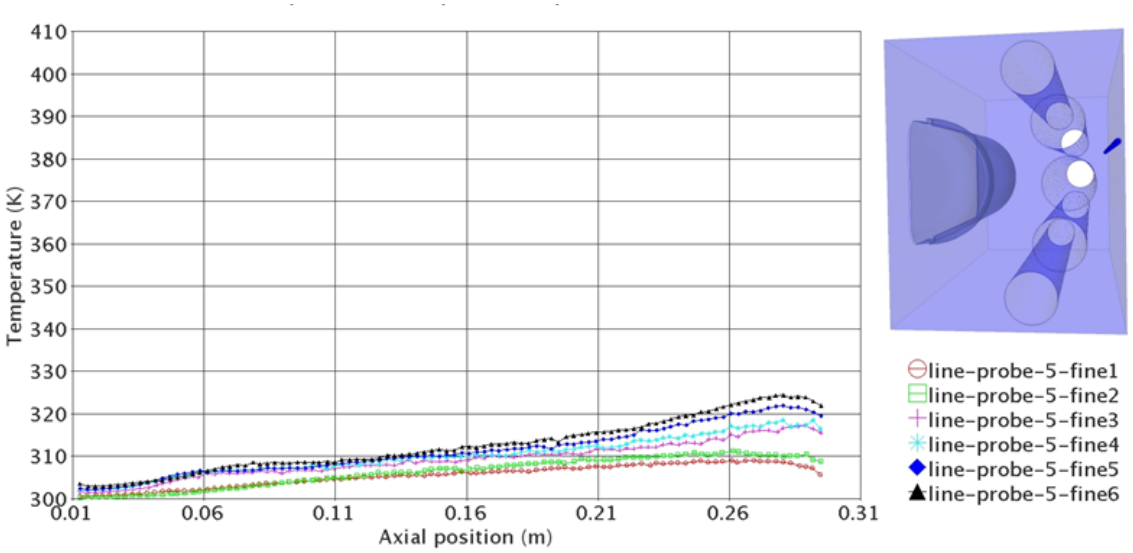

Fig. 79 – Cavity region axial temperature distribution (line probe 5) – Test #9

In Fig. 80 is shown the comparison between the calculated temperature distributions at the standpipes external wall for test #8 and Test #9, respectively. The figure shows that there is a small increase in the standpipes external wall temperature when the RPV power generated is doubled, even for a very small cooling fluid mass flow rate imposed. This result confirms that the RCCS water-cooled configuration represents an effective cooling system for the RCCS cavity walls.

In Fig. 81 is shown the velocity vector distribution in the RCCS cavity region at the rack plane location for Test #8 and #9, respectively. Also for Test #9, the velocity vector plot shows the main recirculation region in the upper half part of the RCCS cavity region between the RPV wall and the standpipes wall. The stagnant region below the RPV lower head and the smaller recirculation region above the RPV upper head can be seen from the figure. Due to the increased power generated inside the RPV region for Test #9 respect to Test #8, buoyancy forces determine an enhanced free convection regime.

In Fig. 82 is shown the temperature distribution plot at the cavity region rack plane for Test #8 and #9, respectively. It is possible to note the stagnant region in the bottom part of the cavity (i.e., an almost uniform temperature distribution is present in this region). Close to the RPV bottom head the air temperature rapidly increases and air is driven by buoyancy upwards the RPV wall. The maximum air temperature is reached at the RPV upper head where separation and reattachment regions are present.

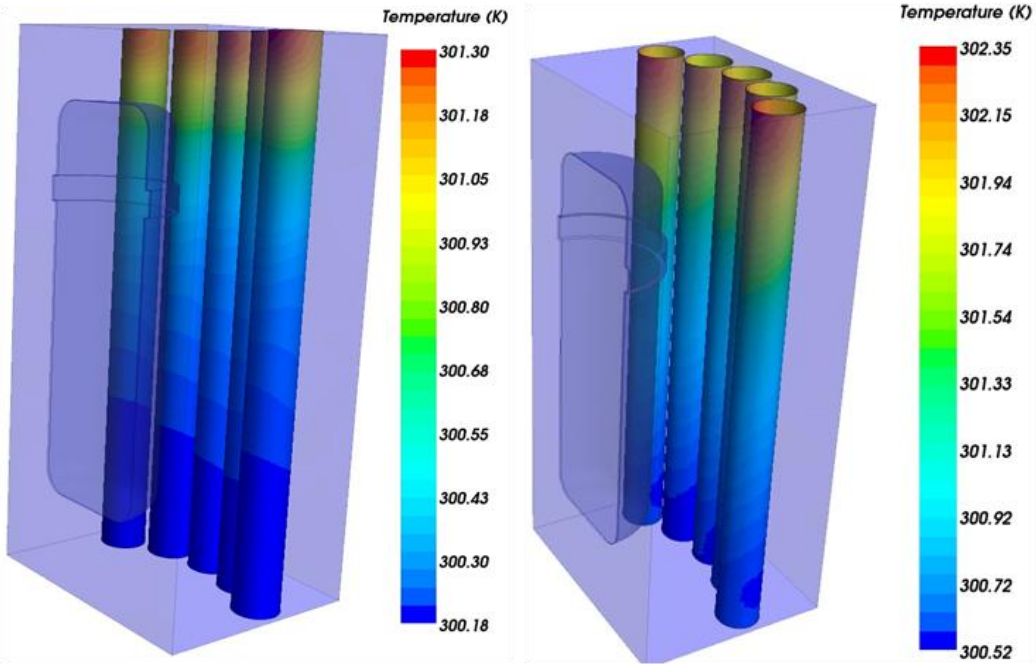

Fig. 80 – Temperature distribution at the standpipes wall – Test #8 (left)/#9 (right)

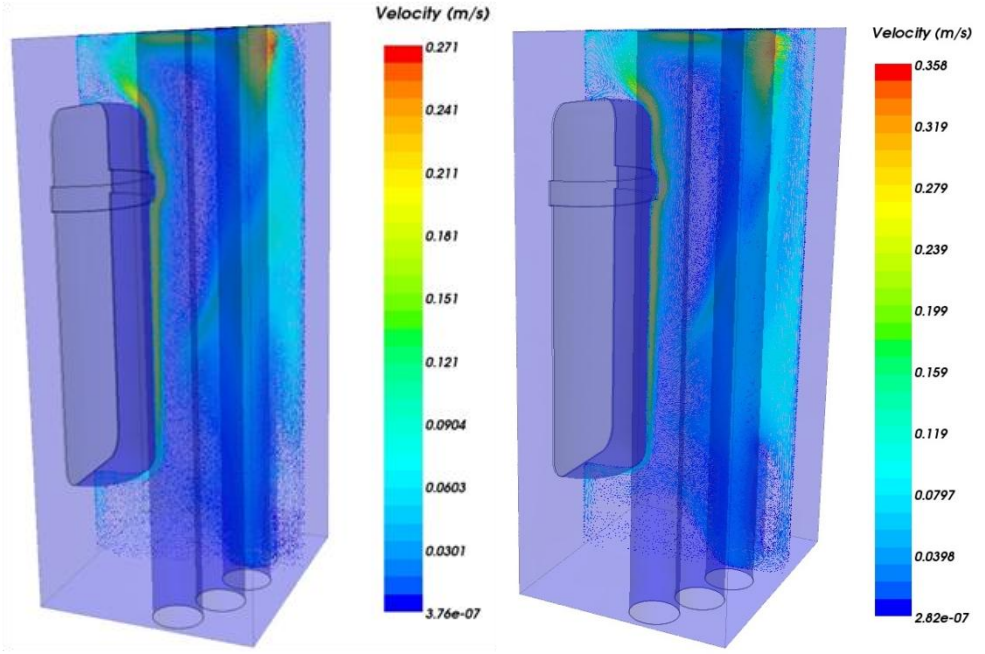

Fig. 81 – Cavity region velocity vector distribution – Test #8 (left)/#9 (right)

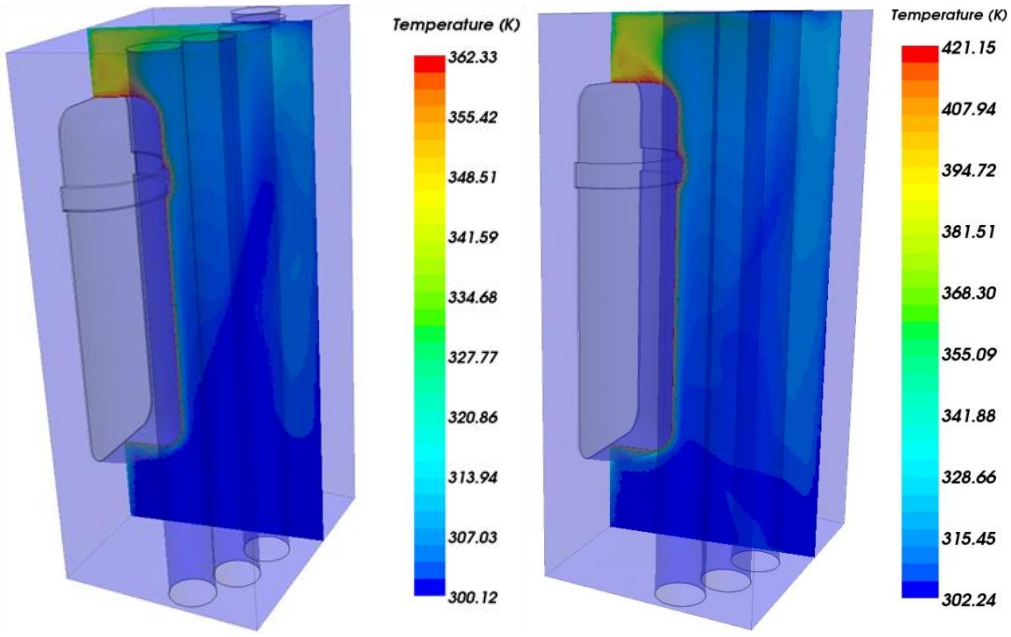

Fig. 82 – Cavity region temperature distribution – Test #8 (left)/#9 (right)

In Fig. 83 and Fig. 84 are shown the radial temperature distribution at the cavity region symmetry plane 215 mm (line probe 3) and 275 mm (line probe 4) from the bottom wall. Fig. 83 shows the radial temperature distribution at the flange location. The figure shows the sharp temperature gradient close to the RPV wall, and a relatively smoother temperature gradient close to the central standpipe wall. The figure also shows that there is a scatter in the temperature distribution close to the wall for the different meshes analyzed, with the finer meshes predicting larger temperature in the cavity region. The temperature profiles for the different meshes almost converge in the central standpipe region.

In the upper part of the RCCS cavity region (see Fig. 84) the effect of mesh refinement on the temperature distribution is even more evident, with difference of more than 40 K between the coarser and finer meshes analyzed, and the finer meshes predicting higher temperature distributions across the RCCS cavity region.

In Fig. 85 is shown the axial velocity distribution in the radial direction at the cavity region symmetry plane 215 mm (line probe 3) from the bottom wall. The effect of buoyancy forces predicted by the different meshes strongly influences the velocity profile close to the RPV wall. This behavior is much less evident close to the central standpipe wall where a smoother temperature profile is present.

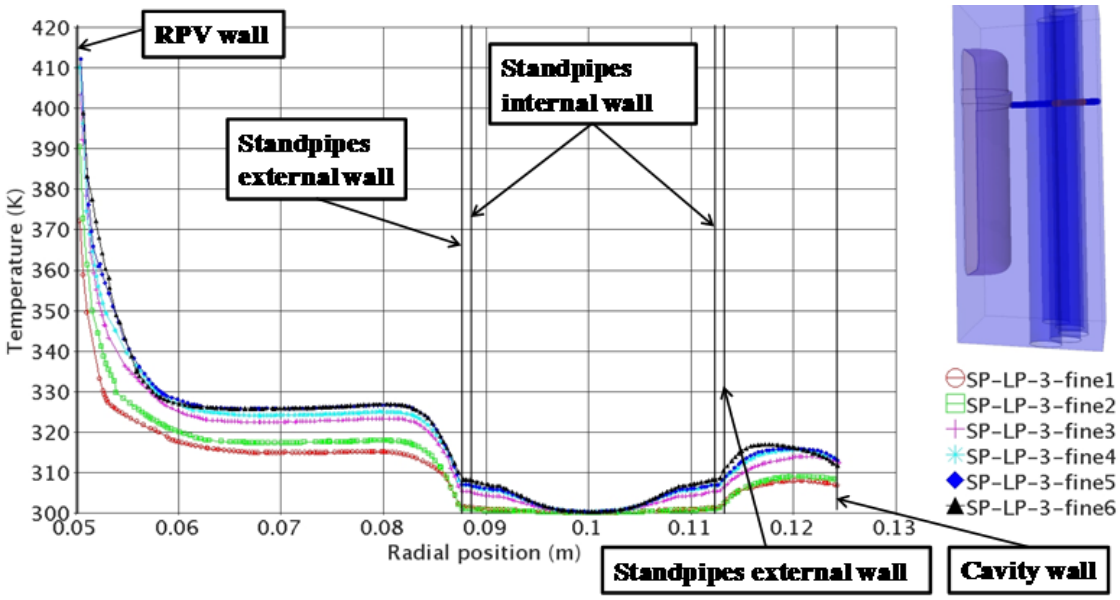

Fig. 83 – Cavity region radial temperature distribution (line probe 3) – Test #9

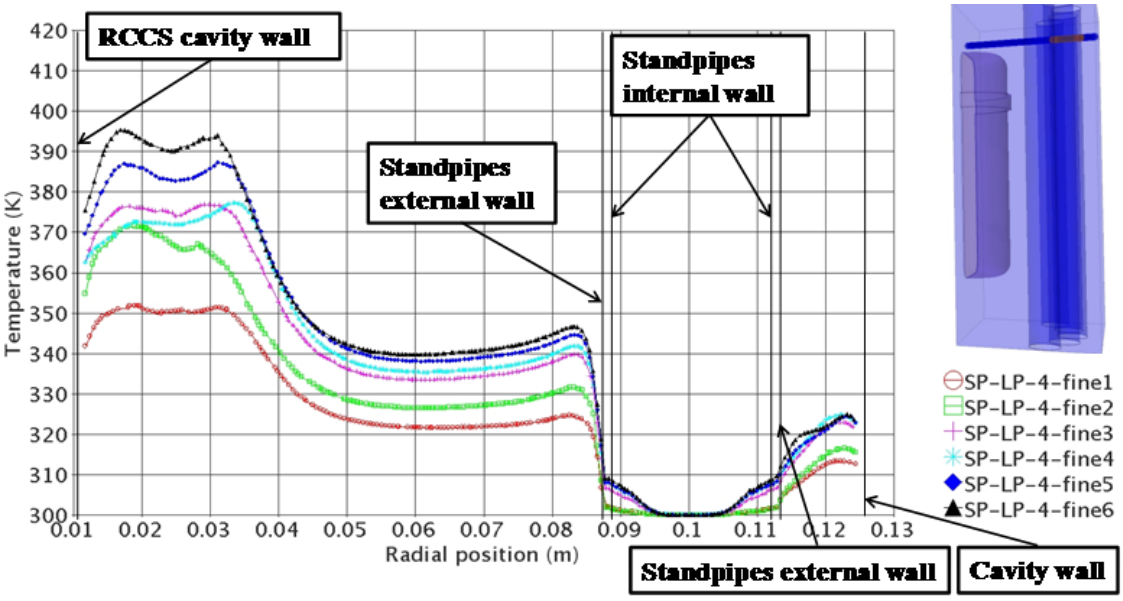

Fig. 84 – Cavity region radial temperature distribution (line probe 4) – Test #9

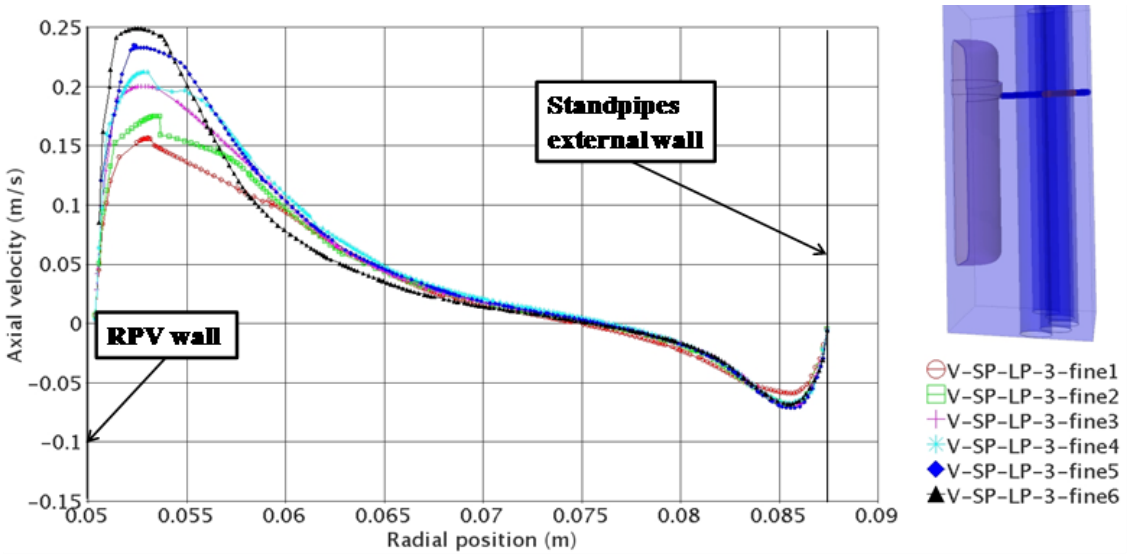

Fig. 85 – Cavity region axial velocity distribution (line probe 3) – Test #9

For the scaling of convection and radiation heat transfer across the RCCS cavity region, the simulation predicted 39% due to radiation and 61% due to convection heat transfer phenomena, respectively. These values are in satisfying agreement with the values obtained from the scaling analysis for Test #9 (7% error), which are 42% and 58% due to radiation and convection heat transfer, respectively. The fact that radiation heat transfer is still below 50 % of the total heat transfer is due to the relatively reduced RPV wall temperature (see Fig. 77). This analysis was performed to address the behavior of the standpipes for the CFD model under very similar conditions to those of the real plant (i.e. a ratio of *Ri* number close to one). Also the Convection and Radiation similarity groups were very close to one. Therefore, the analysis allowed to test if the CFD model introduced distortion respect to the prototype conditions in the scaling of radiation and convection heat transfer phenomena. Since the effect due to radiation and convection heat transfer numerically determined is in good agreement with that

calculated by the scaling analysis, it is possible to conclude that the scaling distortion introduced by the CFD model on radiation and convection heat transfer is of the same order and, therefore, the two heat transfer phenomena are scaled properly by the CFD model, as well as the scaling analysis showed that the radiation and convection heat transfer are properly scaled by the experimental facility.

6.4 Analysis of the RCCS Water-Cooled Configuration (Test #10)

Test #10 was performed setting a uniform volumetric power inside the RPV region, for a total power of 175 W (see Table 13). In Fig. 86 is shown the PRV wall temperature distribution for Test #10 obtained using the Realizable k-ε turbulence model with Two-Layer *all* y^+ Near-Wall treatment. Also for Test #10, the temperature at the RPV wall is almost uniform due to the very high thermal conductivity of the RPV material. The RPV wall maximum temperature is reached at the upper head.

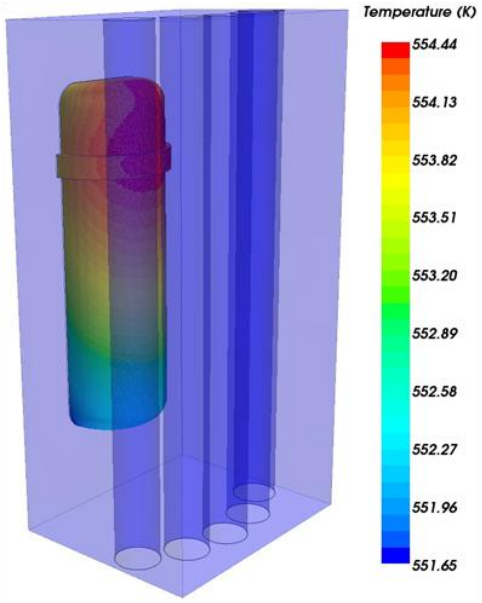

Fig. 86 – RPV wall temperature distribution –Test #10

In Fig. 87 is shown the sensitivity analysis over mesh refinement for the axial temperature distribution at the cavity region rack plane 0.25 mm from the RPV wall (line probe 1). The figure shows that there are some discrepancies in the temperature profiles between the different meshes analyzed. The differences in temperature distribution were expected due to the different mesh refinement necessary to calculate the heat exchange at the interfaces between fluid and solid regions.

Fig. 88 shows the axial temperature distribution at the cavity back wall rack plane location (line probe 5). Also for this analysis the back wall temperature does not exceed 340 K, which is very close to the maximum value reached for Test #8 and Test #9 (320 K and 325 K, respectively). This temperature is still well below the design limits for the cavity concrete walls. It is possible to conclude that, also for the very high RPV

temperature conditions reached in Test #10 (see Fig. 86), the water-cooled RCCS system is still capable of keeping the RCCS external walls temperature below the design limits.

In Fig. 89 is shown the temperature distribution at the standpipes external wall. The figure shows that, even for a sensible increase in the power generated inside the RPV region, the standpipes wall temperature slightly increases. This result confirms that the RCCS water-cooled configuration represents an effective cooling system for the RCCS cavity walls.

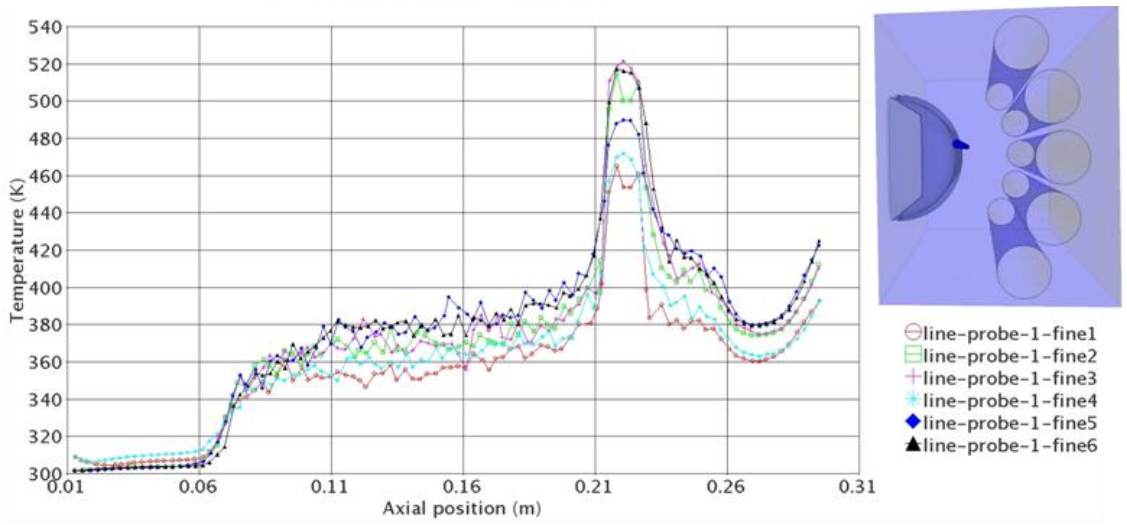

Fig. 87 – Cavity region axial temperature distribution (line probe 1) – Test #10

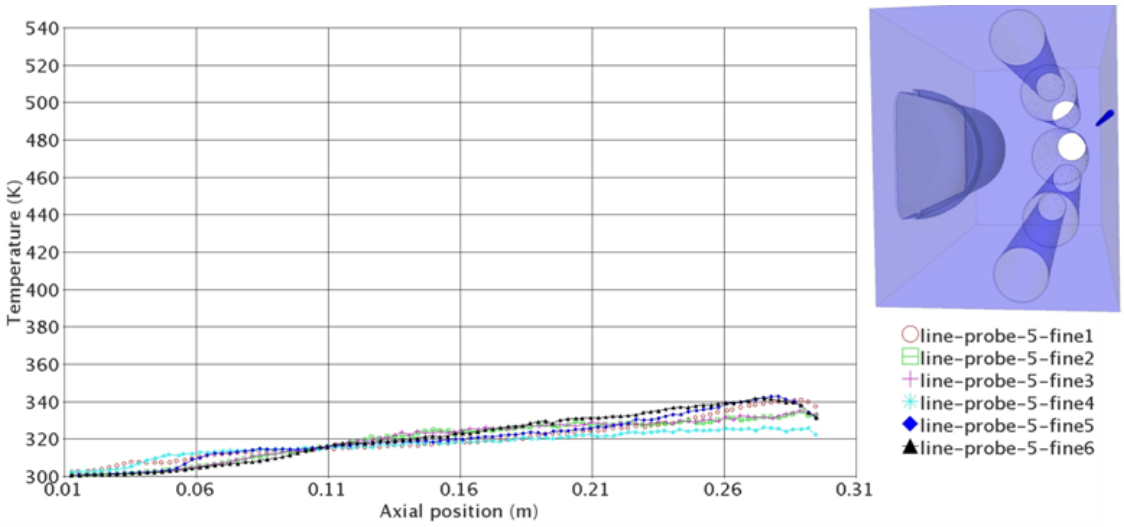

Fig. 88 – Cavity region axial temperature distribution (line probe 5) – Test #10

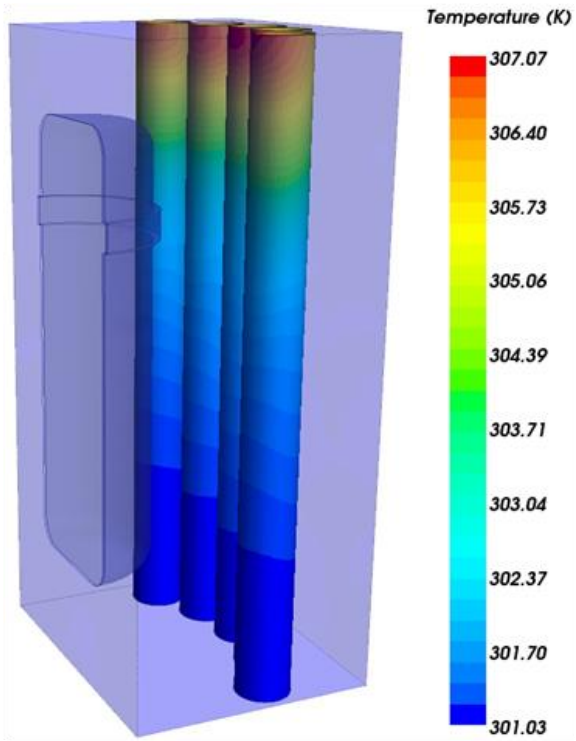

Fig. 89 – Temperature distribution at the standpipes wall – Test #10

In Fig. 90 is shown the velocity vector distribution in the RCCS cavity region at the rack plane location. The velocity vector plot shows the main recirculation region in the upper half part of the RCCS cavity region between the RPV wall and the standpipes wall. Also the stagnant region below the RPV lower head and the smaller recirculation region above the RPV upper head can be identified. Due to the increased power generated inside the RPV region for Test #10 respect to Test #8-9 (i.e., higher PRV wall temperature), buoyancy forces determine an enhanced free convection regime (i.e., a larger Gr/Re^2).

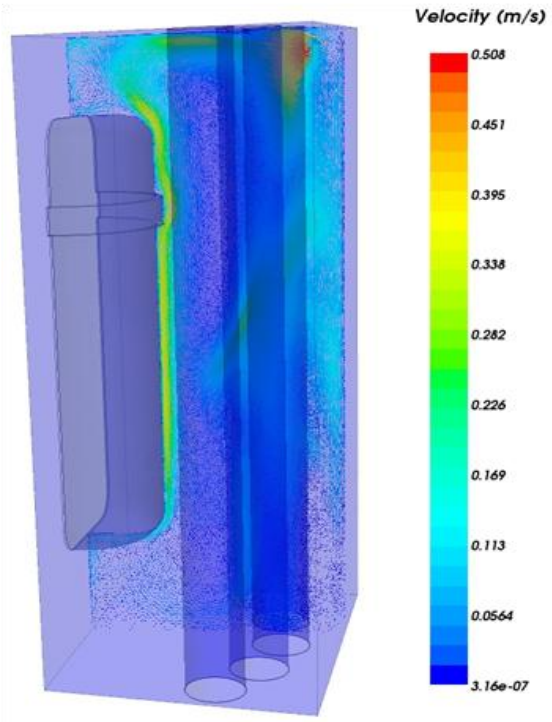

Fig. 90 – Velocity vector in the cavity region (rack plane) – Test #10

In Fig. 91 is shown the temperature distribution at the cavity region rack plane. It is possible to note the stagnant region in the bottom part of the cavity (i.e., an almost uniform temperature distribution is present in this region). Close to the RPV bottom head the air temperature rapidly increases and air is driven by buoyancy upwards the RPV temperature wall. The maximum air temperature is reached at the RPV upper head where separation and reattachment regions are present.

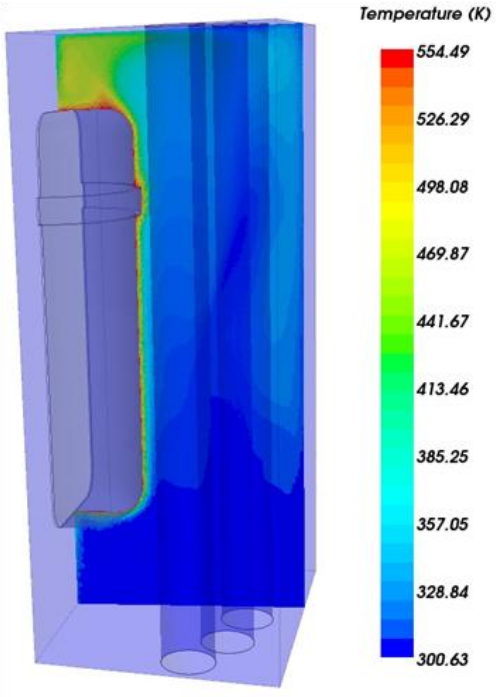

Fig. 91 – Temperature distribution in the cavity region (rack plane) – Test #10

In Fig. 92 is shown radial temperature distribution at the cavity region symmetry plane 275 mm from the bottom wall (line probe 4). The effect of mesh refinement is evident, with the finest mesh giving higher temperature distribution respect to the

coarser meshes. Differences up to 60 K are present in the temperature distribution above the RPV upper head between the coarsest and the finest meshes analyzed.

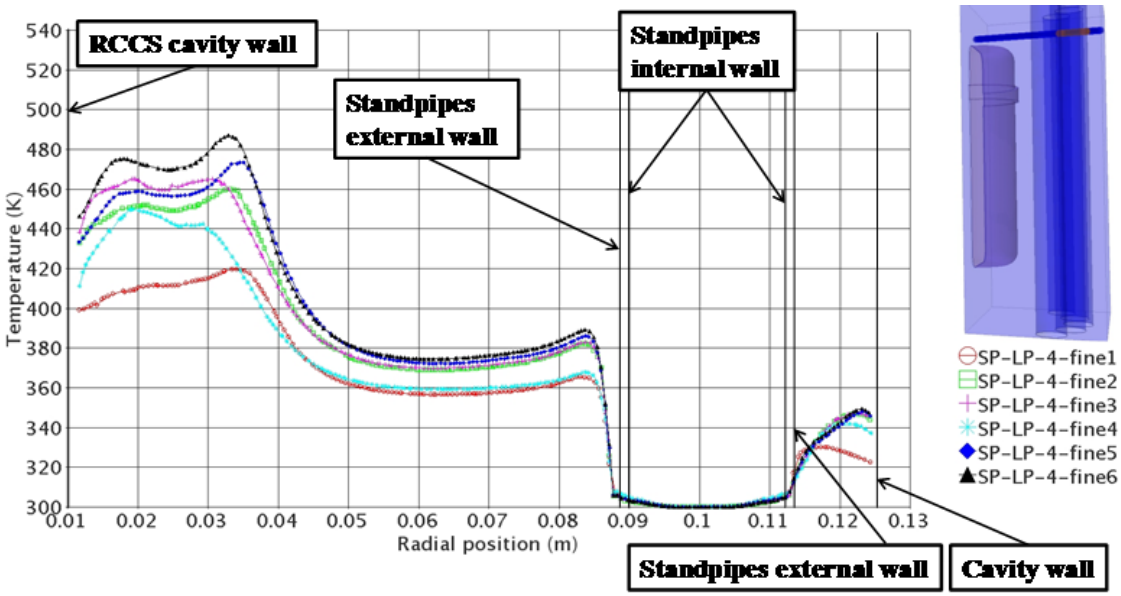

Fig. 92 – Cavity region radial temperature distribution (line probe 4) – Test #10

In Fig. 93 is shown the axial velocity distribution in the radial direction at the cavity region symmetry plane 215 mm from the bottom wall (line probe 3). The figure shows the effect of buoyancy forces on the velocity distribution close to the RPV wall. The finer meshes predict with more accuracy the temperature gradient across the thermal boundary layer, which means a better estimate of the buoyancy forces can be determined. Since buoyancy forces are the driving phenomena in free convection flow regime, a better estimate of the velocity profile close to the RPV wall is obtained for the finer meshes.

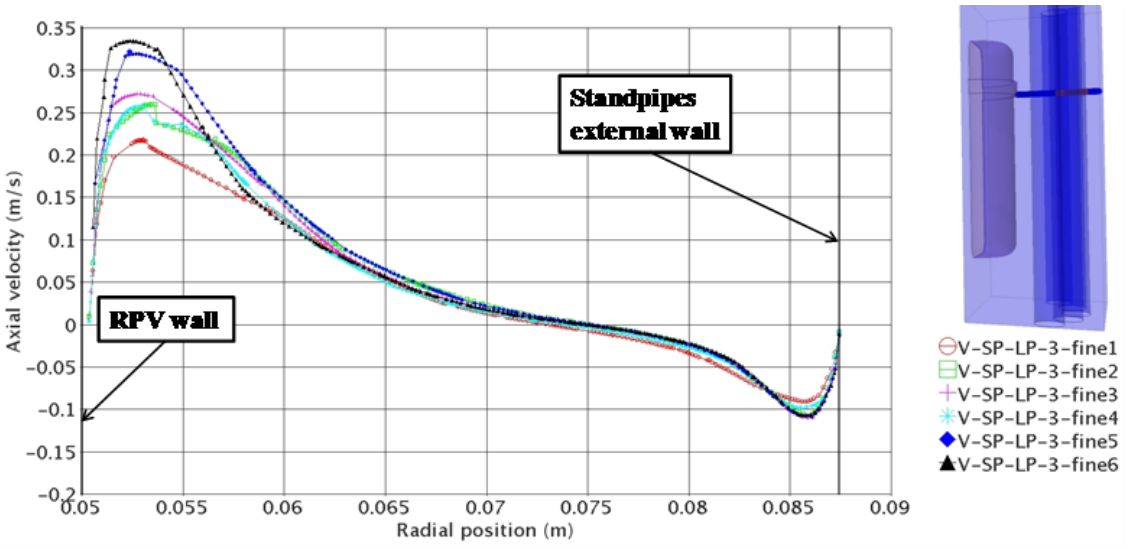

Fig. 93 – Cavity region axial velocity distribution (line probe 3) – Test #10

For the scaling of convection and radiation heat transfer across the RCCS cavity region, the simulation predicts 59.4% due to radiation and 40.6% due to convection heat transfer phenomena, respectively. These value are in satisfying agreement with the values obtained from the scaling analysis for Test #10 (10% error), which are 53.5% and 46.5% due to radiation and convection heat transfer, respectively. Radiation heat transfer is becoming the predominant heat transfer mechanism due to the increase in the RPV temperature (see Fig. 86). For this analysis the ratio of *Ri* number is very close to one, which means that the momentum equation in the standpipes is properly scaled from the prototype down to the model. Also the ratio of Gr/Re^2 in the cavity region is very close to one, which means the effect of buoyancy forces over inertia forces is not distorted, and the physics inside the cavity region is well represented.

Since the effect due to radiation and convection heat transfer numerically determined is in good agreement with that calculated by the scaling analysis, it is

possible to conclude that the scaling distortion introduced by the CFD model on radiation and convection heat transfer is of the same order and, therefore, the two heat transfer phenomena are properly scaled by the CFD model.

In Fig. 94 and Fig. 95 are shown the axial temperature distribution at the cavity region rack plane 0.25 mm (line probe 1) from the RPV wall and at the cavity back wall (line probe 5), respectively. The figures show the comparison between the different turbulence models analyzed. In particular, for Test #10 the following turbulence models were tested: the Realizable k-ε model with Two-Layer *all* y^+ wall treatment, the Abe-Kondoh-Nagano (AKN) k-ε model with Low-Reynolds Number and *all* y^+ wall treatment, the SST k-ω model with *all* y^+ wall treatment, the Reynolds-Stress Transport (RST) with Linear Pressure Strain treatment for the pressure rate of strain tensor and *all* y^+ wall treatment, the Spalart-Allmaras one-equation model with *all* y^+ wall treatment, and the Standard k-ε model with Two-Layer *all* y^+ wall treatment. For the temperature distribution a good agreement between the different turbulence models was achieved. The standard and Realizable k-ε models gave very close temperature distribution prediction, and both models gave a qualitative and quantitative good agreement with the RST turbulence model. The AKN k-ε model, the SST k-ω model and the Spalart-Allmaras one-equation model show some differences respect to the RST in the central part of the RCCS region. This different behavior of the AKN, k-ω and Spalart-Allmaras models is due to the different predictions in the extension of the main recirculation region inside the cavity medium. As the comparison among the different turbulence models for the axial velocity distribution in the cavity region shows (see following

discussion on the velocity distribution), there are some differences at the bottom part of the cavity region, which is where the air moving downwards is redirected towards the RPV wall.

At the cavity back wall (see Fig. 95) there is good agreement among the different turbulence models analyzed, since the temperature gradients and buoyancy effects are much less relevant than close to the RPV wall.

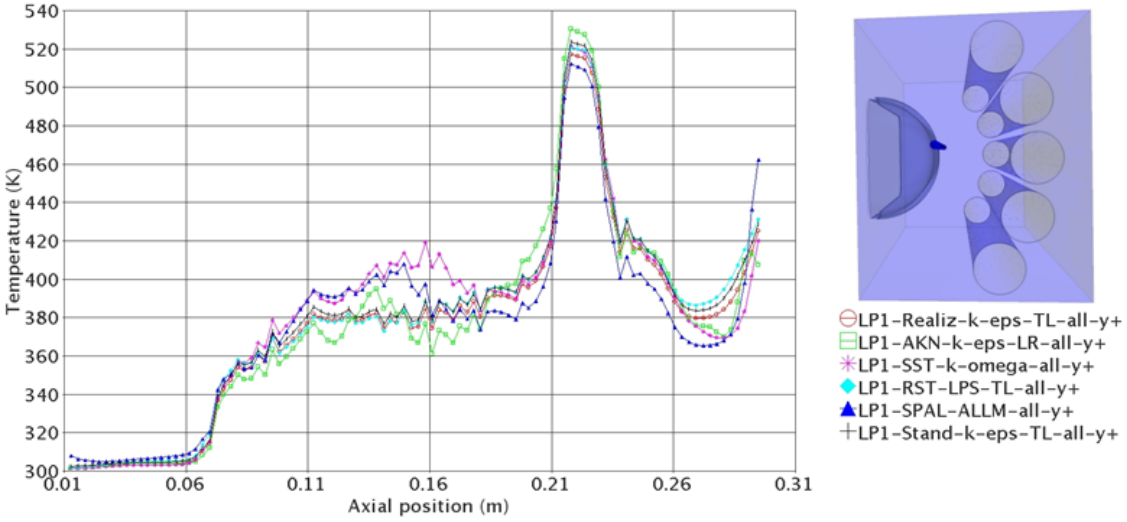

Fig. 94 – Cavity region axial temperature comparison (line probe 1) – Test #10

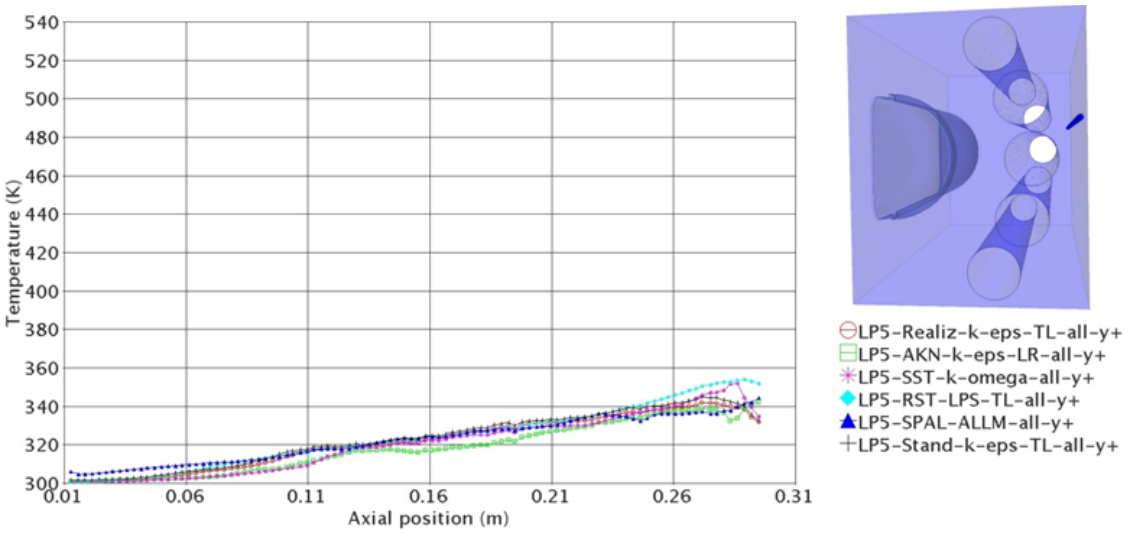

Fig. 95 – Cavity region axial temperature comparison (line probe 5) – Test #10

In Fig. 96 is shown the radial temperature distribution at the symmetry plane in the upper part of the cavity region. The results obtained with the different turbulence models analyzed were compared. Minor temperature differences are shown in the gap region between the RPV wall and the central standpipe wall, meanwhile some scatter is present in the cavity above the RPV upper head. As addressed for the axial temperature distribution, also for the radial temperature distribution this behavior is due to the different velocity predicted by the turbulence models analyzed close to the RPV wall and in the cavity upper region (see Fig. 98).

In Fig. 97 and Fig. 98 are shown the axial velocity distribution at the cavity region symmetry plane, 135 mm and 275 mm above the bottom wall, respectively. The figures show that there are some discrepancies between the different turbulence models analyzed in predicting the extension of the main recirculation region in the lower part of the cavity (see Fig. 97) and in the upper part of the cavity (see Fig. 98). Due to the strong

anisotropy of the Reynolds Stress Tensor and to the 3-dimensional characteristics of the turbulence in the cavity region, the RST is expected to give a better prediction of the flow inside the cavity region. Fig. 97 and Fig. 98 also shows that the axial velocity distributions determined with the Realizable and standard *k-ε* model and Two-Layer *all* y^+ Near-Wall treatment are very close to that predicted with the RST turbulence model, meanwhile the AKN *k-ε*, the SST *k-ω* and the Spalart-Allmaras models under/over-estimate the extension of the main recirculation region, the effect of buoyancy close to the RPV wall, the temperature distribution in the thermal boundary layer, etc.

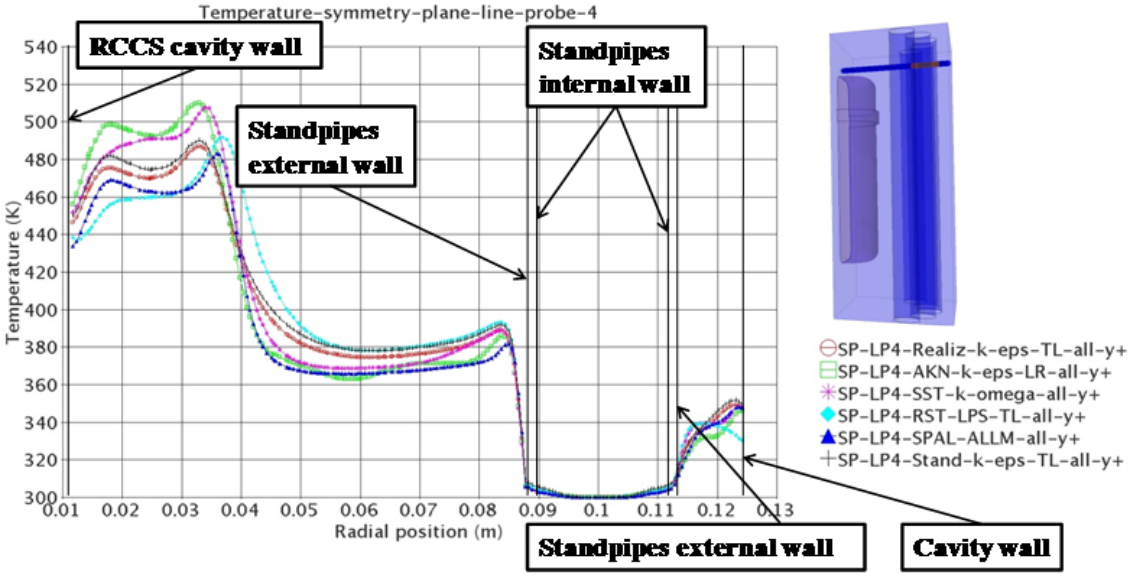

Fig. 96 – Cavity region radial temperature comparison (line probe 4) – Test #10

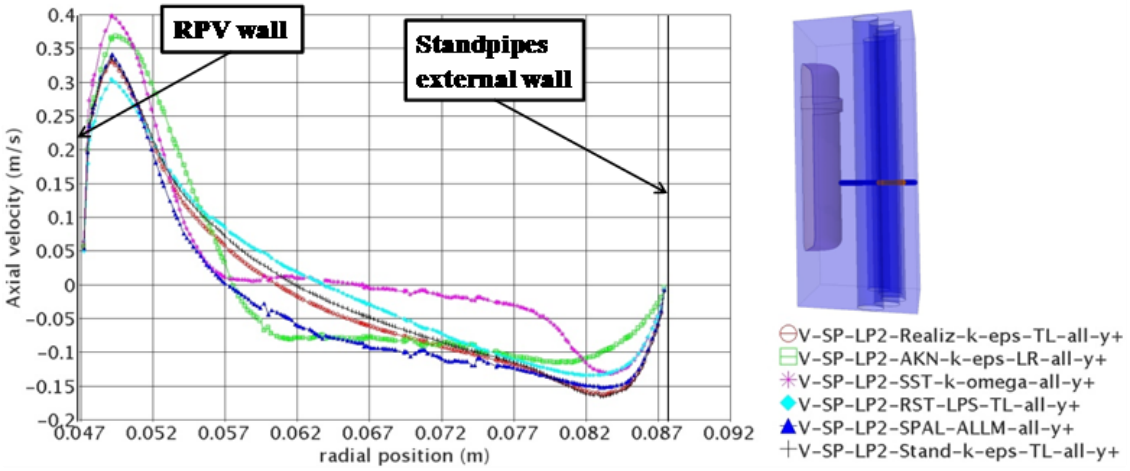

Fig. 97 – Cavity region axial velocity comparison (line probe 2) – Test #10

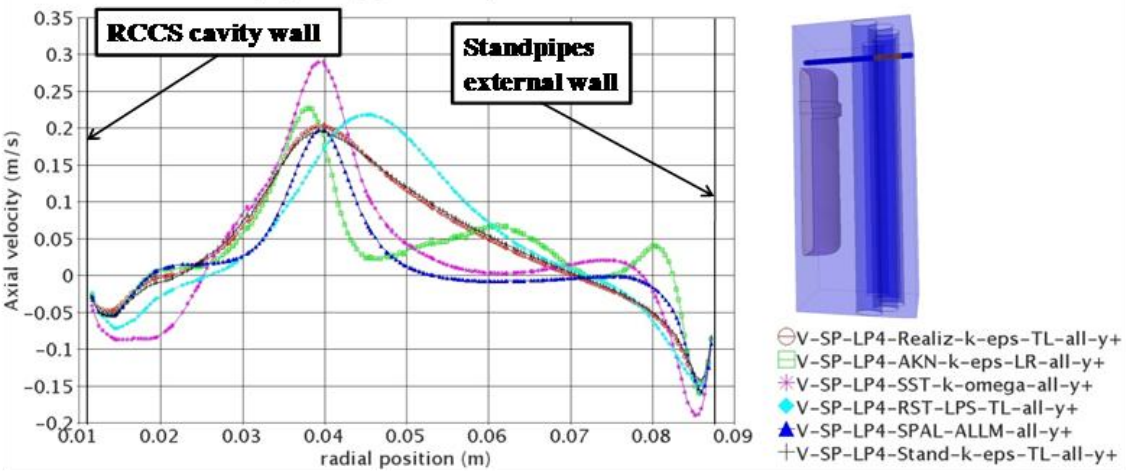

Fig. 98 – Cavity region axial velocity comparison (line probe 4) – Test #10

6.5 Analysis of the RCCS Air-Cooled Configuration (Test #11)

Test #11 through Test #18 consider the RCCS in the air-cooled configuration, which is air is flowing inside the standpipes. As shown in Table 15, for Test #11 through #15, a constant mass flow rate was imposed at the standpipes inlets, meanwhile temperature profiles were set at the RPV wall boundary. The different temperature profiles were

chosen in such a way to simulate different working conditions for the RPV wall and for the RCCS cavity region. For Test #11 the RPV wall temperature profile shown in Fig. 99 was set as boundary condition. After mesh convergence, it was possible to determine the total amount of energy dissipated inside the cavity region due to the imposed temperature profile at the RPV wall, which is 23.4 W, as shown in Table 15. With a uniform heat source inside the RPV region, an almost uniform temperature distribution is obtained at the RPV wall due to the very high thermal conductivity of the material chosen for the RPV (i.e., *Cu*). On the other hand, the power generated inside the RPV has not a uniform distribution both during normal operation and accident conditions. With the reactor in shutdown conditions (e.g, following a scram due to an accident scenario), the largest part of energy generated inside the RPV is due to the decay heat of the reactor core. Other sources of heat are the thermal energy stored inside the reactor vessel internals, and the γ heating on the RPV walls and other metallic components close to the core region. It is very difficult to have an exact prediction of the energy distribution inside the RPV, and the heat flux at the RPV wall. From experimental data (see IAEA (2000)], it was possible to have a rough estimate of the heat fluxes at the RPV wall during the different phases of PCC and DCC scenarios, which give temperature distributions qualitatively similar to those used for to those used for Test #11 through #18. The objective of these analyses was to test the performance of the RCCS air-cooled configuration, imposing temperature profiles at the RPV wall which take into account the non-uniform distribution of heat generated inside the vessel, and address the behavior of the RCCS system for the boundary conditions set.

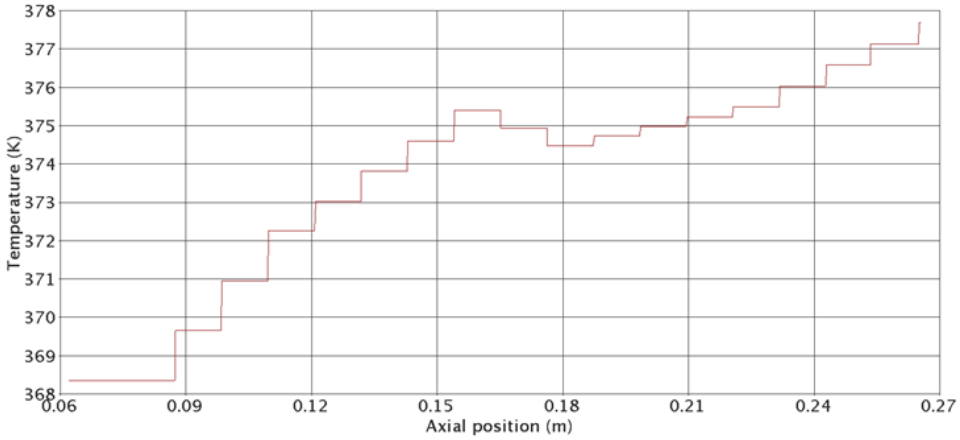

Fig. 99 – RPV wall temperature distribution (boundary condition) –Test #11

In Fig. 100 and Fig. 101 are shown the axial temperature distribution at the cavity region rack plane, 5.0 mm (line probe 1) for the RPV wall and on the cavity back walls (line probe 5), respectively. Both figures show the effects of mesh refinement on the temperature distribution. The coarsest mesh predicts higher temperature inside the cavity region, both close to the RPV wall and at the cavity back wall. The mesh sensitivity analysis shows that there is good agreement among the finest meshes results. The air close to the RPV wall is moving upstream due to buoyancy effects. There is a local maximum temperature close to the RPV flange location (see Fig. 100). At the cavity back wall (see Fig. 101) the maximum temperature is reached close to the top wall, and is well below design limits.

Fig. 102 shows the radial temperature distribution at the cavity symmetry plane 275 mm (line probe 4) from the bottom wall. The scatter on the temperature predictions is due to differences in the velocity distribution above the RPV upper head (i.e., secondary

recirculation region) for the various meshes considered. The coarsest mesh predicts higher temperature in the gap region, and on the cavity back wall.

In Fig. 103 is shown the axial velocity distribution at the cavity region symmetry plane 215 mm (line probe 3) above the bottom wall, which is at the flange location. The figure shows the air moving upwards close to the RPV wall due to buoyancy forces, and moving downwards close to the central standpipe wall. The finest mesh predicts the largest velocity close to the RPV wall.

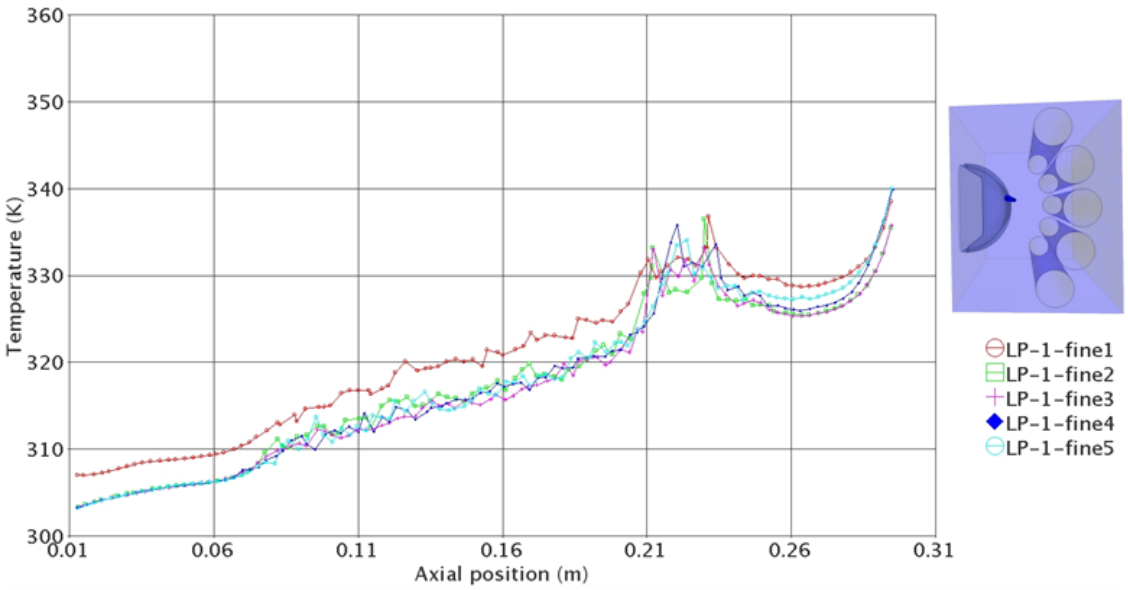

Fig. 100 – Cavity region axial temperature distribution (line probe 1) – Test #11

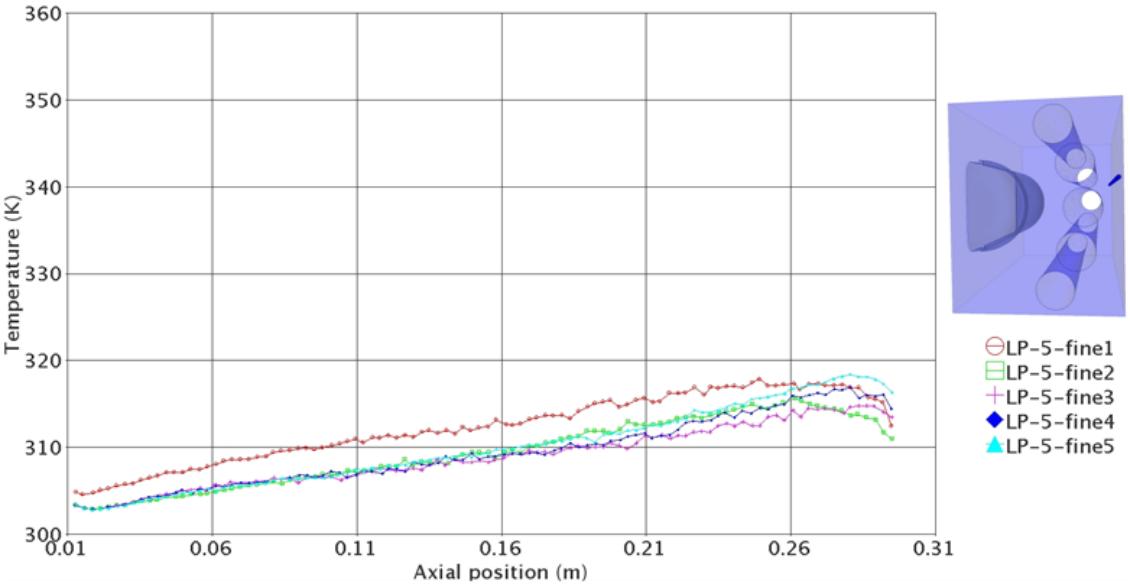

Fig. 101 – Cavity region axial temperature distribution (line probe 5) – Test #11

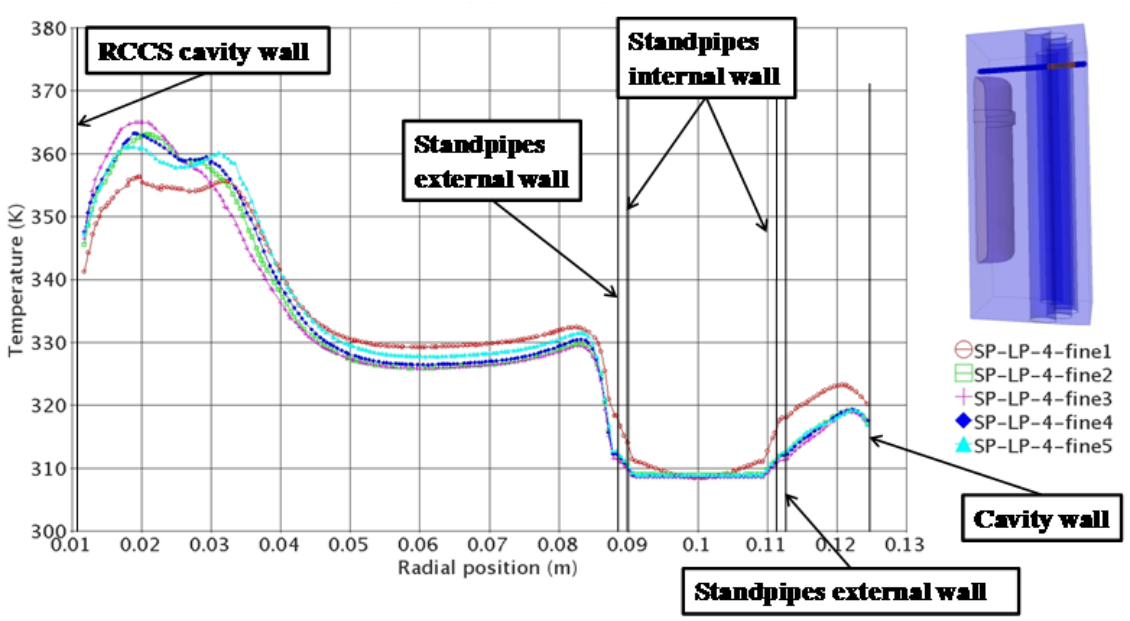

Fig. 102 – Cavity region radial temperature distribution (line probe 4) – Test #11

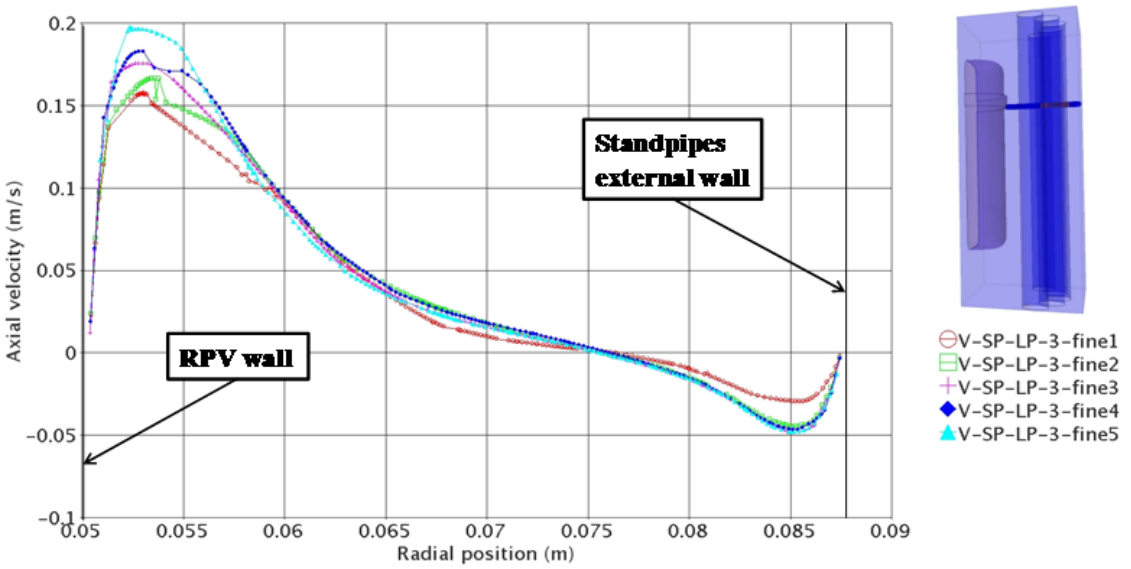

Fig. 103 – Cavity region axial velocity distribution (line probe 3) – Test #11

With the temperature profile set as boundary condition at the RPV wall, the numerical computation predicted 61.4% and 38.6% due to radiation and convection heat transfer respectively in the RCCS cavity region between the RPV wall and the standpipes wall. The scaling analysis predicted 63.4% and 36.6% for radiation and convection heat transfer respectively, which are in good agreement with the numerical results (3% error).

This means that, with the predicted temperature distribution imposed at the RPV wall as boundary condition, and with the standpipes in air-cooled configuration, the numerical simulation give a good representation of the physics inside the RCCS cavity region. The ratio of Gr/Re^2 is close to one, which means there are no significant distortions introduced in the flow dynamics inside the cavity region, even if buoyancy is underestimated (i.e., Ratio of *Ra* number much smaller than one). The ratio of radiation

and convection numbers is not close to unity, but the same amount of distortion is introduced on the two phenomena. Therefore the distortions introduced by the CFD model are of the same order of magnitude for the two heat exchange mechanisms.

This analysis was performed to gain understanding on the behavior of the RCCS in the air-cooled configuration.

6.6 Analysis of the RCCS Air-Cooled Configuration (Test #12)

For Test #12 the temperature profile shown in Fig. 104 was imposed as boundary condition at the RPV wall. In Table 15 are given the other boundary conditions. The effect of increasing the temperature distribution at the RPV wall determines an increase in the power generated inside the RPV region (43.16 W). Also for this analysis a non-uniform power generated inside the RPV region was assumed to simulate the non-uniform heat flux at the RPV wall. Due to the presence of the reactor core in the lower part of the RPV, a local maximum in temperature distribution was assumed in the bottom half of the vessel region. Due to the reduced heat exchange between the RPV wall and the recirculating air in the cavity region, the RPV wall temperature increases again towards the RPV upper head, as shown in Fig. 104.

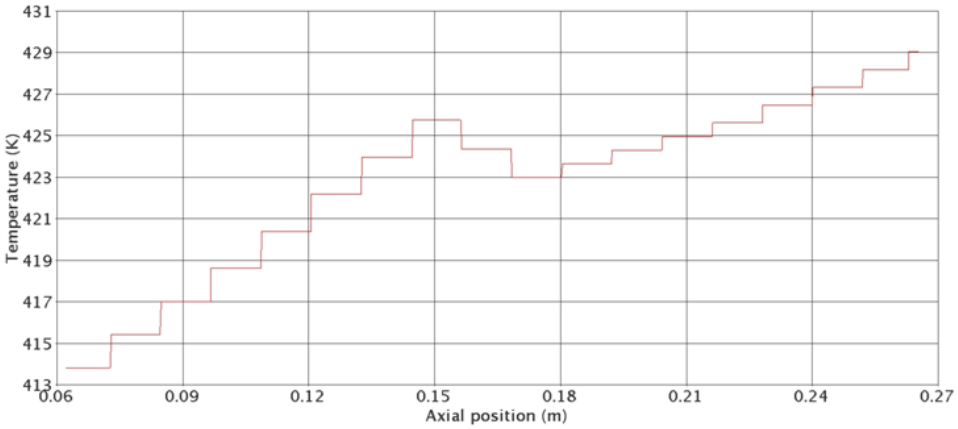

Fig. 104 – RPV wall temperature distribution (boundary condition) –Test #12

In Fig. 105 is shown the axial temperature distribution in the cavity region at back wall rack plane location (line probe 5). With an increased temperature at the RPV wall, the maximum temperature on the cavity back face goes for 320 K for Test #11 to almost 340 K for Test #12, which is still well below the design limits. The coarsest mesh predicts larger temperature than the finer meshes, which give satisfying agreement on the temperature distribution. Some differences were found on the axial velocity distribution close to the RPV wall (line probe 3), as shown in Fig. 106. Finer meshes determine a larger axial velocity distribution close to the RPV wall respect to coarser meshes. This behavior is due to a more accurate prediction of the heat exchange close to the RPV wall and, therefore, of the buoyancy effects, which are the driving force in the momentum equation for the free convection flow regime present in the RCCS cavity region.

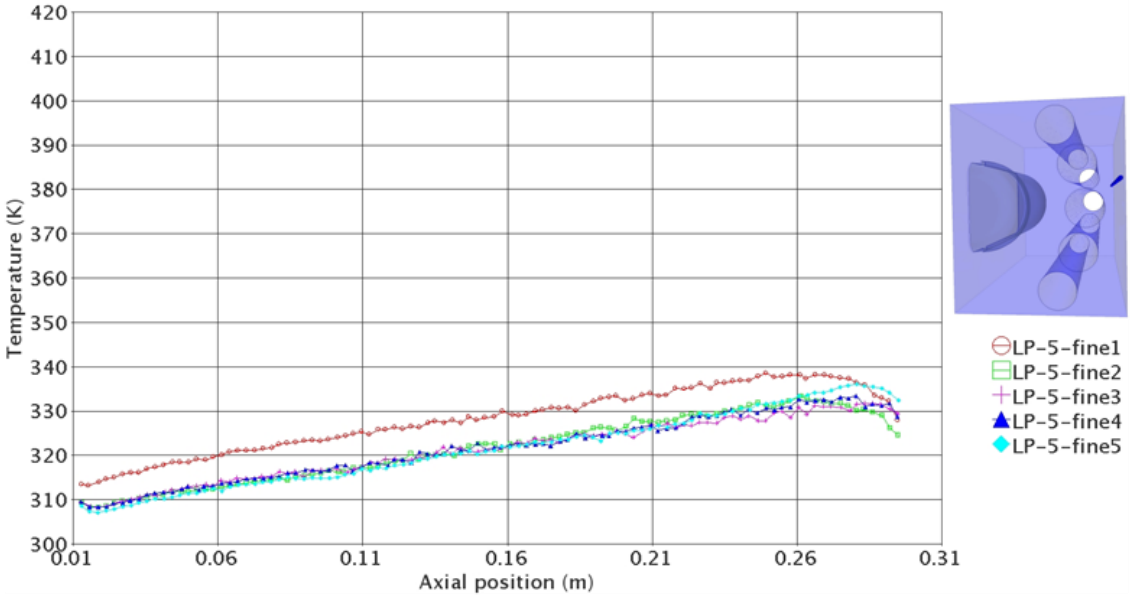

Fig. 105 – Cavity region axial temperature distribution (line probe 5) – Test #12

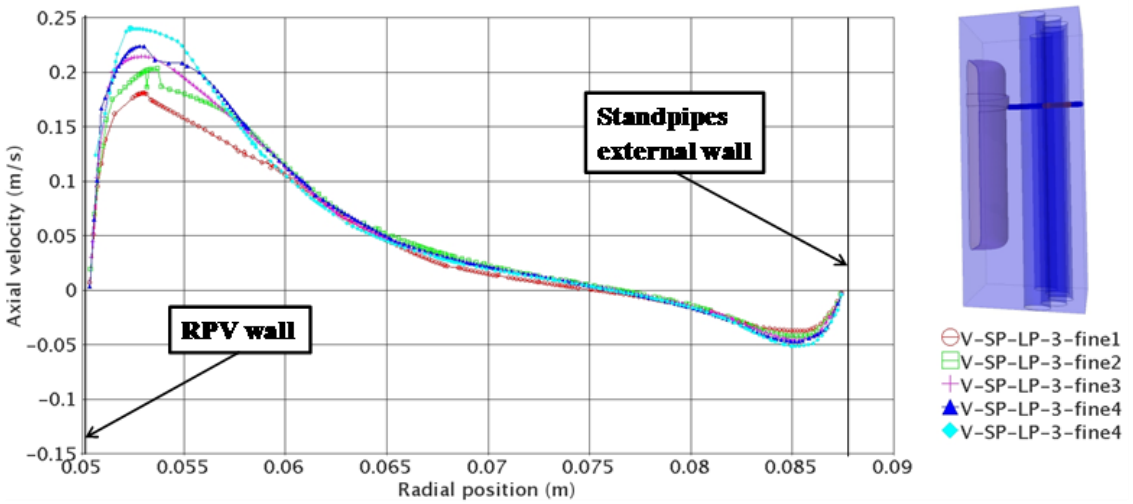

Fig. 106 – Cavity region axial velocity distribution (line probe 3) – Test #12

For Test #12 the numerical computation predicted 67.2% and 32.8% heat transfer due to radiation and convection phenomena, respectively. The scaling analysis predicted

64.4% and 35.6% for radiation and convection heat transfer respectively, which are in good agreement with the numerical results (less than 4.2% error).

With the ratio of Gr/Re^2 being very close to one, and the same amount of distortion introduced by the CFD model on radiation and convection heat exchange phenomena, a satisfying description of the physics inside the RCCS cavity is expected by the CFD model developed.

6.7 Analysis of the RCCS Air-Cooled Configuration (Test #13)

In Fig. 107 is shown the temperature profile imposed as boundary condition at the RPV wall for Test #13. In Table 15 are given the other boundary conditions. The imposed temperature profile at the RPV wall is equivalent to a total power generated inside the RPV region of 65.5 W. The temperature profile imposed at the RPV wall simulates the non-uniform heat generated inside the RPV, with the effect due to the decay heat of the reactor core.

In Fig. 108 is shown the axial temperature distribution at the RCCS cavity back wall rack plane location (line probe 5). The mesh sensitivity analysis shows that the coarsest mesh predicts a higher temperature distribution on the cavity back wall respect to the finer meshes. The maximum temperature is reached close to the cavity top wall. With the boundary conditions imposed, the maximum temperature on the cavity walls is close to the design limits.

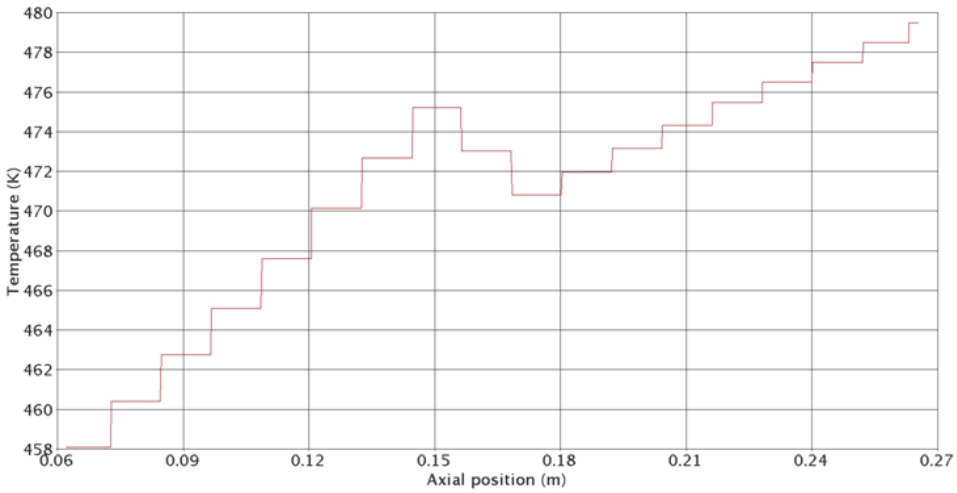

Fig. 107 – RPV wall temperature distribution (boundary condition) –Test #13

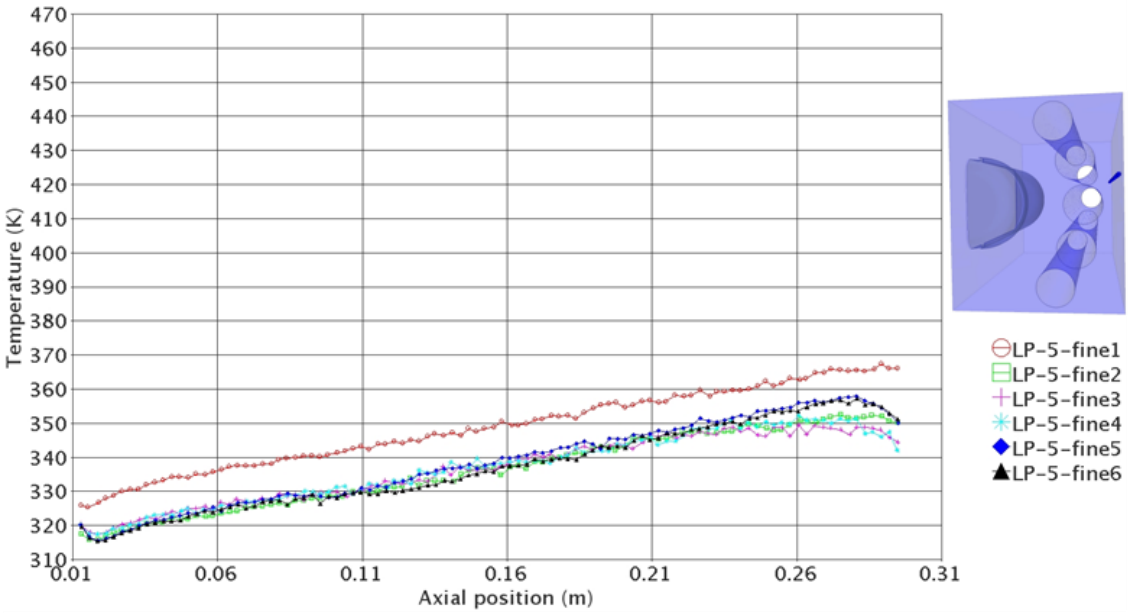

Fig. 108 – Cavity region axial temperature distribution (line probe 5) – Test #13

Fig. 109 shows the axial velocity distribution in the radial direction at the cavity region symmetry plane 215 mm (line probe 3) from the bottom wall (i.e., flange location). The mesh sensitivity shows that the finer meshes give a higher air velocity

close to the RPV wall, due to a better prediction of the buoyancy effects where very large temperature gradients are present.

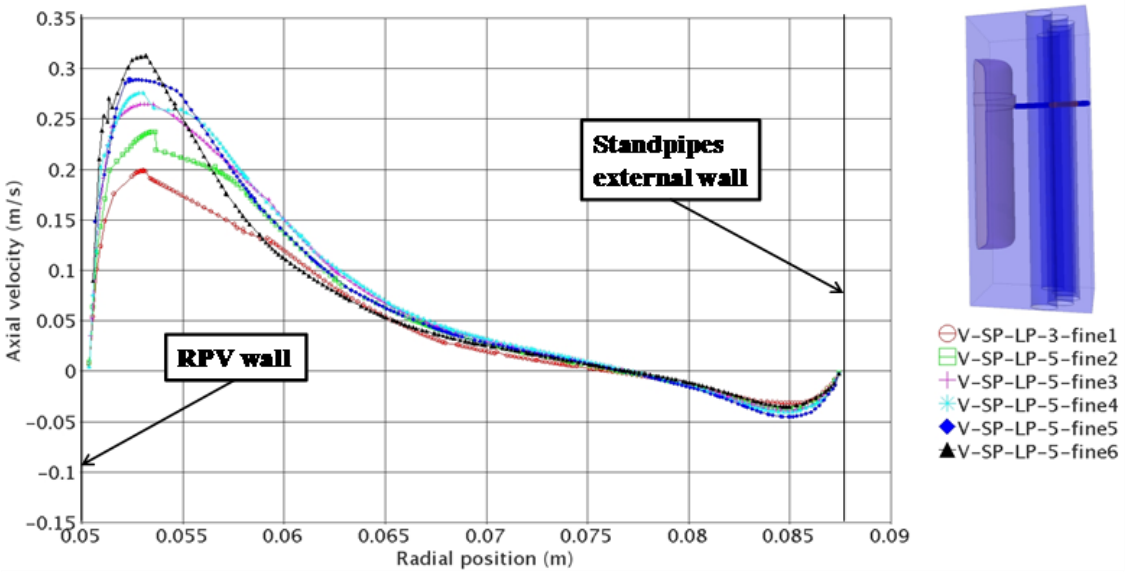

Fig. 109 – Cavity region axial velocity distribution (line probe 3) – Test #13

The CFD simulations with the boundary conditions set for Test #13 predicted 69% and 31% heat transfer due to radiation and convection phenomena respectively in the RCCS cavity region between the RPV wall and the standpipes wall. The scaling analysis predicted 66.5% and 33.5% for radiation and convection heat transfer respectively, which are close to the numerical results (less than 3.6% error).

For this analysis the ratio of Gr/Re^2 is 0.728, which means a negligible distortion in the scaling of buoyancy over inertia forces is introduced by the CFD model. Some distortion is introduced in the scaling of radiation and convection heat transfer phenomena.

6.8 Analysis of the RCCS Air-Cooled Configuration (Test #14)

Fig. 110 shows the temperature profile imposed as boundary condition at the RPV wall for Test #14. In Table 15 are given the other boundary conditions. The imposed temperature profile at the RPV wall is equivalent to a total power generated inside the RPV region of 104.2 W. The temperature profile imposed at the RPV wall simulates the non-uniform heat generated inside the RPV region.

Fig. 111 shows the axial temperature distribution at the cavity back wall rack plane location (line probe 5). Also for Test #14, the mesh sensitivity analysis shows that the coarsest mesh predicts a higher temperature distribution on the cavity back wall respect to the finer meshes. The maximum temperature is reached close to the cavity top wall. The figure shows that the maximum temperature ranges between 370 K and 390 K, which is the temperature for which the concrete material starts to show an increase in the rate of properties deterioration.

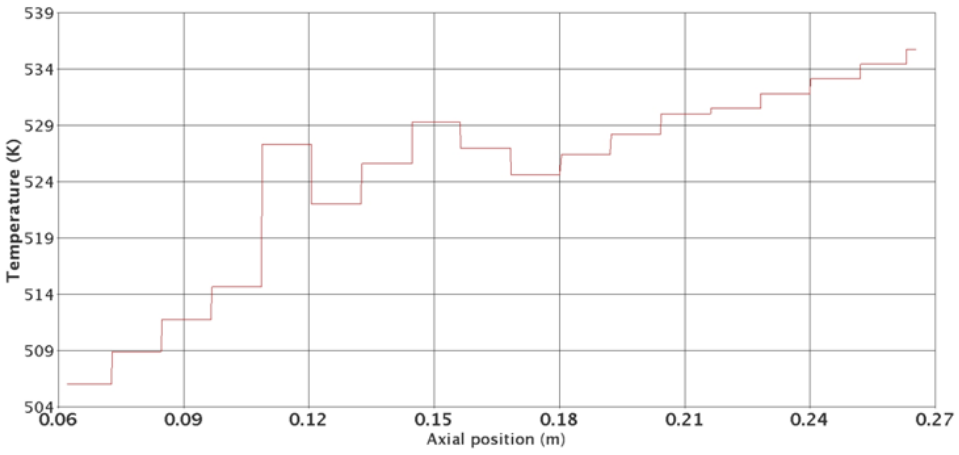

Fig. 110 – RPV wall temperature distribution (boundary condition) –Test #14

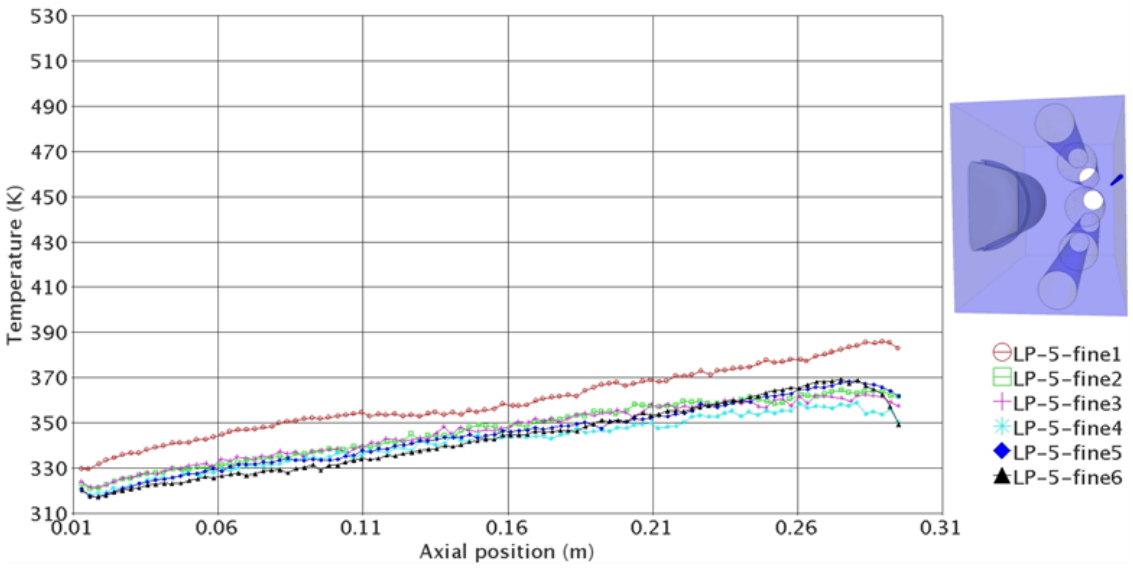

Fig. 111 – Cavity region axial temperature distribution (line probe 5) – Test #14

Fig. 112 shows the axial velocity distribution in the radial direction at the cavity region symmetry plane 275 mm (line probe 4) from the bottom wall (i.e., above the RPV upper head). The mesh sensitivity shows that there are some differences in the extension of the main and secondary recirculation regions in the cavity above the RPV upper head (i.e., the location of the separation and reattachment points on the RPV upper head).

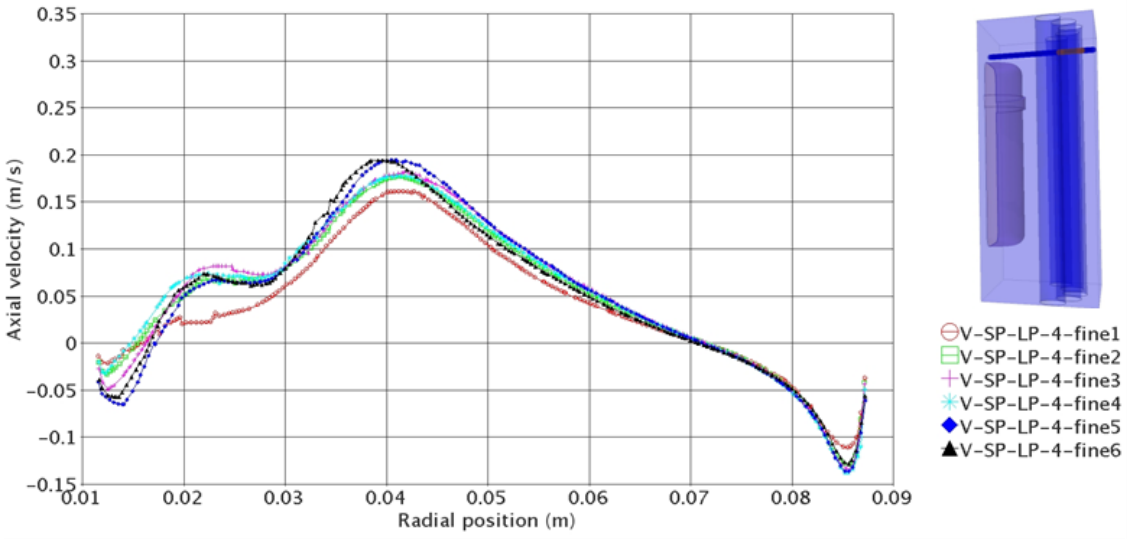

Fig. 112 – Cavity region axial velocity distribution (line probe 4) – Test #14

The CFD simulations with the boundary conditions set for Test #14 predicted 75.5% and 24.5% heat transfer due to radiation and convection phenomena, respectively. The scaling analysis predicted 77.3% and 22.7% for radiation and convection heat transfer respectively, which is in good agreement with the numerical results (less than 2.4% error).

For this analysis the ratio of Gr/Re^2 is 0.91, which means buoyancy over inertia forces are properly scaled from the real plant down to the CFD model. Also the ratio of convection and radiation numbers is close to one. This means that the physics inside the RCCS cavity is well scaled by the CFD model.

6.9 Analysis of the RCCS Air-Cooled Configuration (Test #15)

In Fig. 113 shows the temperature profile imposed as boundary condition at the RPV wall for Test #15. In Table 15 are given the other boundary conditions. The

imposed temperature profile at the RPV wall is equivalent to a total power generated inside the RPV region of 131.0 W. The temperature profile imposed at the RPV wall simulates the non-uniform heat generated inside the RPV.

In Fig. 114 is shown the comparison for the temperature distribution at the RCCS cavity back wall rack plane location (line probe 5) for Test #3, #8, #9, #10, #11, #12, #13, #14 and #15, respectively. Test #3 was performed setting a temperature distribution on the RPV wall boundary which gave a total power generated inside the RPV region equal to 196 W. For Test #8, #9, and #10 a uniform volumetric heat source inside the RPV region was specified, for a total power generated equal to 27.0 W, 50.0 W and 170.0 W respectively. The cooling fluid in the standpipes was water (see Section 6.1-6.4). For Test #11 throughout #15 the same standpipes air mass flow rate was imposed. On the other hand, the different temperature profiles imposed at the RPV wall for Test #11-15 determined a different amount of energy generated inside the RPV region: 23.4 W, 43.16 W, 65.5 W, 104.2 W and 131.0 W, respectively. Fig. 114 shows that the maximum temperature is reached close to the cavity top wall for all analyses. The air-cooled configurations give a higher air temperature distribution inside the RCCS cavity region and at the cavity walls respect to the water-cooled configurations. Comparing Test #3 (water-cooled configuration with 196 W RPV total power generated) with Test #15 (air-cooled configuration with 130 W RPV total power generated), it is evident that even with a 30% less power generated, the air-cooled configuration gives a maximum temperature on the cavity walls of about 395 K, more than 50 K higher than the maximum temperature reached for Test #3 (about 345 K). These results demonstrate the

better performance of the water-cooled RCCS configuration with respect to the air-cooled one.

Considering the results obtained for the RCCS air-cooled configuration, for Test #11, #12 and #13, the maximum concrete wall temperature is below the design limits, meanwhile for Test #14 it is very close to the design limits. With the boundary conditions set for Test #15, the maximum temperature at the cavity walls is above the design limits.

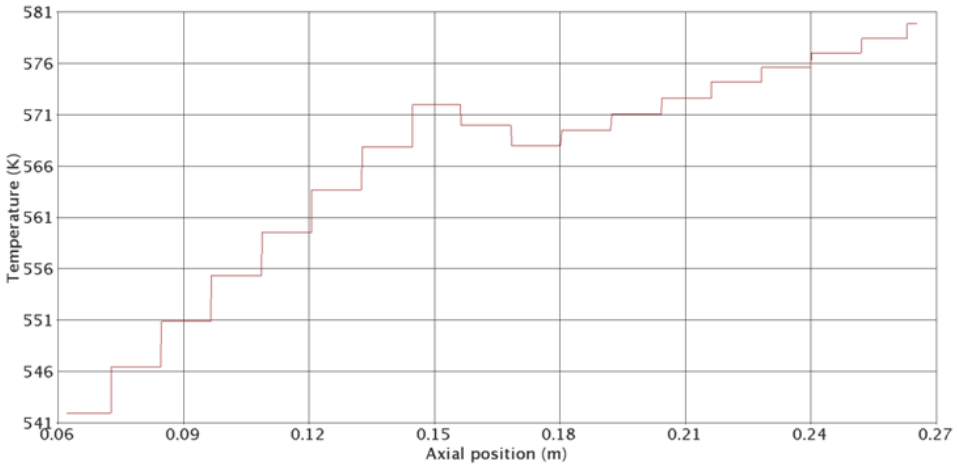

Fig. 113 – RPV wall temperature distribution (boundary condition) –Test #15

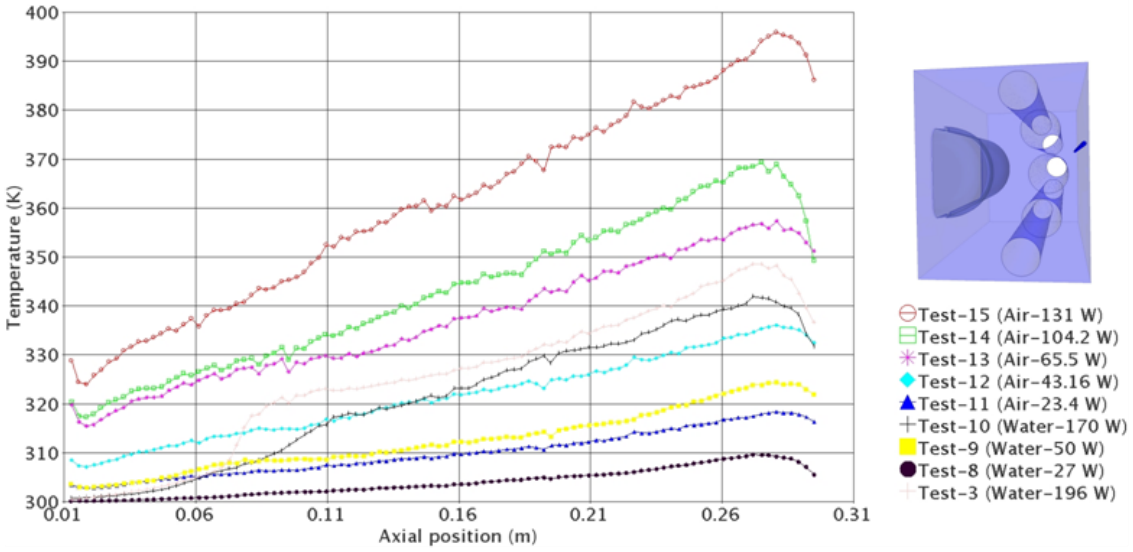

Fig. 114 – Cavity region axial temperature comparison (line probe 5) – Test #3-15

The CFD simulations with the boundary conditions set for Test #15 predicted 87.8% and 12.2% heat transfer due to radiation and convection phenomena, respectively. The scaling analysis predicted 83.7% and 16.3% for radiation and convection heat transfer respectively, with an error less than 4.7%.

For this analysis the ratio of Gr/Re^2 is 1.044, which means no distortion is introduced in scaling buoyancy over inertia forces from the real plant down to the CFD model. Also the ratios of convection and radiation numbers are close to one, which means that the physics inside the RCCS cavity is well scaled by the CFD model.

7. CONCLUSIONS

The objective of the present work was to apply Computational Fluid Dynamics tools to the analysis of the Reactor Cavity Cooling System, which is one of the safety system designed for Very High Temperature Gas-Cooled Reactors.

From a preliminary Phenomena Identification and Ranking Table analysis of the accident scenarios which might generate the most severe consequences for VHTRs, the Pressurized Conduction Cooling (PCC) accident was identified as one of the most demanding transient conditions. Fluid properties in the reactor cavity, convective and radiation heat transfer across the cavity region, pressure drop in the cooling pipes, buoyancy effects, etc., are some of the most relevant phenomena to be addressed if a satisfactory prediction of the PCC transient evolution is required.

An experimental facility was designed and operated at Texas A&M University. The CFD model realized reproduced the exact geometry of the experimental facility and all the main features. The comparison between the experimental data collected at Texas A&M University and the numerical results allowed to test the capability of the CFD code STAR-CCM+/V.3.06.006 in simulating such a complex system, addressing its strength and weaknesses in reproducing the physics inside the RCCS cavity system.

A scaling analysis was performed to address the distortions introduced by the experimental facility and CFD model developed respect to the real plant RCCS configuration. The scaling analysis pointed out that the mockup/CFD model well address the physics inside the RCCS cavity region for a wide range of operating conditions and

both water-cooled and air-cooled RCCS configurations. In particular, with a ratio of Gr/Re^2 very close to one, buoyancy over inertia forces are properly reproduced inside the models. This implies the correct flow paths and recirculation regions are reproduced. Since the whole energy balance between the RPV wall and the standpipes wall is due to radiation and convection heat exchange phenomena, a proper scaling of these two heat exchange mechanisms was necessary to address the real conditions of the RCCS safety system. The sensitivity over different standpipes mass flow rates, RPV wall temperature profiles and RPV volumetric heat sources showed that the correct repartition of energy transfer by radiation and convection is predicted in the experimental facility and CFD model for both water- and air-cooled configurations. The scaling analysis also addressed that the conditions inside the mockup/CFD model standpipes introduce some distortion respect to the natural circulation flow regime expected for the real configuration. Also for this point, the numerical sensitivity performed with the CFD model allowed to show that the natural circulation conditions can be simulated for the model setting a very low standpipes mass flow rate (i.e., ratio of *Ri* number very close to one). The geometrical configuration chosen for the model standpipes introduces some distortions in the scaling of the heat exchange at the standpipes walls, which means that the model standpipes have a larger heat exchange capacity if compared to the real plant standpipes configuration. This was to be expected since the 492 standpipes designed for the real plant where scaled with 5 standpipes in the model developed at Texas A&M University.

Also buoyancy effects are distorted in the model developed due to the physics of the problem. Reducing the heated length of almost two orders of magnitude will determine a

reduction in the buoyancy forces of $100^3=10^6$ times, if the other parameters remain unchanged.

The numerical computations showed good agreement with the experimental data for the temperature distribution in the RCCS cavity region. Some differences were present close to the cavity bottom wall due to the fact that the mockup cavity bottom wall was partially realized in aluminum, meanwhile the CFD model cavity external box was assumed to be glass. The aluminum in the mockup determined a back reflection inside the cavity region, not simulated by the CFD model. Beside this discrepancy, the numerical results for the temperature distribution in the upper part of the RCCS cavity qualitatively and quantitatively were in good agreement with the experimental data.

The sensitivity analysis over the different turbulence models showed that the Realizable and Standard *k-ε* models with Two-Layer *all* y^+ Near-Wall treatment perform better than the SST and Standard k-ω models, the AKN *k-ε* model, and the Spalart-Allmaras one-equation model, showing closer agreement with the experimental data and the RST turbulence model.

Considering the strong anisotropy of turbulence especially close to the wall, the RST model was expected to perform much better than the *k-ε* models in determining the conjugate heat transfer close to the RPV wall, where very strong temperature gradients and three-dimensional turbulence effects are present. The results showed that no sensible differences were present between the simulations performed with the RST turbulence model and those realized with the Realizable and Standard *k-ε* models, even if the computational effort was strongly increased. The reason for such behavior is partially

due to a not enough fine mesh discretization close to the RPV wall, and also to the fact that the flow regime inside the RCCS cavity region is not completely turbulent. Some stratification regions in the lower part of the cavity can be identified where return to laminar conditions might be present. These conditions are extremely arduous to simulate even for the most advanced commercial CFD codes, if the closure problem of the momentum and energy equations is resolved by using first or second-moment closure equations. The best way to approach this problem would be perhaps to use Large Eddy Simulation methodologies, where a negligible part of the turbulence dissipation is modeled, and the main structures of the flow are completely resolved.

The sensitivity over mesh convergence showed that the results are extremely dependent on the mesh refinement at the fluid/solid interface (i.e., where conjugate heat transfer is present). In particular, the region close to the RPV wall requires very fine meshes due to the large temperature gradients at the wall. These temperature gradients sensibly influence the buoyancy effects close to the vessel wall and, therefore, the flow regime inside the RCCS cavity. Also the change of fluid properties plays a dominant role in determining the buoyancy effects inside the RCCS cavity region.

One of the strength of CFD codes is their ability to simulate radiation heat exchange phenomena in very complex geometries, where the determination of view factors represents the main problem for analytical solution of the problem.

The numerical analyses performed on the RCCS with water-cooled and air-cooled configurations allowed to address the better performance of the former respect to the latter in reducing the stress on the cavity concrete walls. The sensitivity performed over

different RPV wall temperature distributions allowed to give a general idea of the cavity wall temperatures during the phases of a PCC transient. The analyses showed that, in the critical stage of the transient (i.e., see Test #14 and #15), the cavity wall peak temperature might exceed the design limits for the air-cooled configuration; meanwhile the water-cooled configuration provides a more efficient cooling, with the cavity wall peak temperature below the design limits even if more arduous conditions are assumed throughout the transient evolution.

REFERENCES

Abe, K., Kondoh, T., Nagano, Y., 1991. A new turbulence model for predicting fluid flow and heat transfer in separating and reattaching flows – 1. Flow field calculation. Int. J. Heat Mass Transfer, 37, 1-13.

Ball, S. J., 2003. MHTGR accident analysis. American Nuclear Society MHTGR Technology Course, June.

Capone, L., Perez, C.E., Hassan, Y.A., 2010. Experimental investigation of reactor cavity cooling system for very high temperature gas-cooled reactors. In: 18th International Conference on Nuclear Engineering, Xi'an, China, May 17-21, ICONE18.

Frisani, A., Capone, L., Ugaz, V.M., Hassan, Y.A., 2009. Three-dimensional simulation of RCCS heat exchange using STAR-CCM+ CFD code. In: ANS Annual Meeting, June 14-18, Atlanta, GA.

Frisani, A., Ugaz, V.M., Hassan, Y.A., 2009. On the effect of turbulence modeling and near-wall treatment in simulating heat exchange in the reactor cavity cooling system using STAR-CCM+ CFD code. In: ANS Winter Meeting and Nuclear Technology Expo, November 15-19, Washington DC.

Gibson, M.M., Launder, B.E., 1978. Ground effects on pressure fluctuations in atmospheric boundary layer. J. Fluid Mech., 86(3), 491-511.

International Atomic Energy Agency website, 2000. Heat transport and afterheat removal for gas cooled reactors under accident conditions. IAEA-TECDOC-1163. http://www.iaea.org/inisnkm/nkm/aws/htgr/abstracts/abst_crp3.html

Jones, W.P., Launder, B.E., 1972. The prediction of laminarization with a two-equation model of turbulence. Int. J. Heat and Mass Transfer, 15, 301-314.

Kader, B.A., 1981. Temperature and concentration profiles in fully turbulent boundary layers. Int. J. Heat Mass Transfer, 24, 1541-1544.

Kassir, M. K., Bandyopadhyay, K.K., Reich, M., 1996. Thermal degradation of concrete in the temperature range from ambient to 315 °C. Office of Environmental Restoration and Waste Management, United States Department of Energy, Washington D.C., Contract No. DE-AC02-76CH00016.

Krüger, K., Bergerfurth, A., Burger, S., Pohl, P., Wimmers, M., Cleveland, J. C., 1991. Preparation, conduct, and experimental results of AVR loss-of-coolant accident simulation test. Nucl. Sc. and Eng., 107, 99-113.

Launder, B.E., Sharma, B.I., 1974. Application of energy dissipation model of turbulence to the calculation of flow near a spinning disc. Letter in Heat and Mass Transfer, 1 (2), 131-138.

Lien, F.S., Chen, W.L., Leschziner, M.A., 1996. Low-Reynolds number eddy-viscosity modeling based on non-linear stress-strain / vorticity relations. In: Proc. 3rd Symp. On Engineering Turbulence Modeling and Measurement, May 27-29, Crete, Greece.

Menter, F.R., 1994. Two-equation eddy-viscosity turbulence modeling for engineering applications. IAAA Journal, 3(8), 1598-1605.

Nuclear Regulatory Commission website, 2009. http://www.nrc.gov.

Reichardt, H., 1951. Vollstaendige Darstellung der turbulenten geschwindigkeitsverteinlung in glatten Leintungen. Z. Angew. Math. Mech. 31, 208-219.

Rodi, W., 1991. Experience with two-layer models combining the k-ε model with a one-equation model near the wall. In: 29th Aerospace Sciences Meeting, January 7-10, Reno, NV, AIAA 91-0216.

Sarkar, S., Balakrishnan, L., 1990. Application of a Reynolds-stress turbulence model to the compressible shear layer. ICASE Report 90-18, NASA CR 182002. http://ntrs.nasa.gov/.

Schultz R.R., 2007. Next generation nuclear plant methods technical program plan. INL/EXT-06-11804, January.

Shih, T.H., Liou, W.W., Shabbir, A., Yang, Z., Zhu, J., 1994. A New k-ε eddy viscosity model for high Reynolds number turbulent flows - model development and validation. NASA TM 106721. http://ntrs.nasa.gov/.

Spalart, P. R., Allmaras, S. R., 1992. A one-equation turbulence model for aerodynamic flows. In: 30th Aerospace Sciences Meeting , January 6-9, Reno, NV, AIAA-92-03439.

Speziale, C.G., Sarkar, S., Gatski, T.B., 1991. Modeling the pressure-strain correlation of turbulence: an invariant dynamical systems approach. J. Fluid Mech., 227, 245-272.

Vilim, R.B., Feldman, E.E., 2005. Scalability of the Natural Convection Shutdown Heat Removal Test Facility (NSTF) data to VHTR/NGNP RCCS designs. Nuclear Engineering Division, Argonne National Laboratory, June 30, ANL-GenIV-049.

Wilcox, D. C., 1998. Turbulence modeling for CFD. 2nd edition, DCW Industries, Inc.

Wolfstein , M., 1969. The velocity and temperature distribution in one-dimensional flow with turbulence augmentation and pressure gradient. Int. J. Heat Mass Transfer, 12, 301-318.

Xu, W., Chen, Q., Nieuwstadt, F. T. M., 1998. A new turbulence model for near-wall natural convection. Int. J. Heat Mass Transfer, 41, 3161-3176.

VITA

Name:	Angelo Frisani
Address:	Department of Nuclear Engineering Texas A&M University 129 Zachry Engineering Center, 3133 TAMU College Station, TX 77843-3133
E-mail address:	a.frisani@neo.tamu.edu
Education:	B.S., Nuclear Engineering, University of Pisa (Italy), 5-year Degree (Laurea), 110/110 cum laude, 2005. M.S, Nuclear Engineering, Texas A&M University, 2010.